12-19-2021

Droplet-Based Fuel Property Measurements

Wanjun Dang

DROPLET-BASED FUEL PROPERTY MEASUREMENTS

A Dissertation

Submitted to the Graduate Faculty of the
Louisiana State University and
Agricultural and Mechanical College
in partial fulfillment of the
requirements for the degree of
Doctor of Philosophy

in

Department of Mechanical & Industrial Engineering

by
Wanjun Dang
B.E., Wuhan University of Technology Huaxia College, 2008
M.E., Wuhan University of Technology, 2011
May 2022

Acknowledgments

I would like to express my gratitude to several people who have supported me in achieving this degree and making graduate school at LSU one of the memorable experiences in my life. First and foremost, I would like to give thanks to my advisor, Dr. Shyam Menon, for recruiting me as his first PhD student and providing financial support, continuous guidance on research work, and timely mentoring of the common issues I met as an international student. I will never forget his knowledgeable teaching, patient advising, and high standards of work ethics. I hope I can learn from him and make continuous improvements in my future career. I would like to thank other faculty members on my committee, Dr. Schoegl, Dr. Devireddy, Dr. Gartia, and Dr. Dorman. I would also like to give thanks to Dr. Charalampopoulos, who allowed me to audit his undergraduate heat transfer class in Spring 2018.

I would like to acknowledge several of my PhD co-workers and undergraduate researchers for supporting me during the last four years. I will not forget my journal paper co-author Mohana, who used ANSYS Fluent to analyze the non-idealities in damped oscillations; lab colleagues Navid, David, Varun, William, and Wei, who had good discussions with me about research and helped me lift heavy objects during experiments.

I am also grateful for the support from my friends I have made at LSU (Edison, Susheel, Veerendra, Nishir, Arash, Behnam, Muneera, Sanjay, Connor, Lijesh, Armaghan, Thomas) and others whom I might have missed out here.

I would like to thank my parents for their perpetual love and caring. They are always available if I want to talk. They always give their full support for my study and life.

Finally, I would like to give thanks to the funding agency for my research work. Their funding support made this work possible. All chapters of this dissertation were conducted as part of the Co-Optimization of Fuels & Engines (Co-Optima) project sponsored by the U.S. Department of Energy (DOE) Office of Energy Efficiency and Renewable Energy (EERE), Bioenergy Technologies and Vehicle Technologies Offices.

With the research funding from DOE, the patient guidance from Dr. Menon and Dr. Schoegl, the genuine caring from my co-workers, friends, and parents, I could realize my childhood dream of doing PhD in the US.

Thank you all for supporting me going through my PhD journey from 2017 to 2021!

Table of Contents

List of Tables

List of Figures

Abstract

Ongoing work to find renewable biofuels to function as drop-in replacements or blending components with gasoline has identified a large number of fuel candidates. Given the vast number of potential biomass-derived fuel molecules and limited sample sizes, screening tools are required to down-select candidate fuels having desired physical properties to ensure good engine performance. This work investigates approaches for rapid screening of candidate fuels using micro-liter sample sizes targeting four properties – surface tension, viscosity, heat of vaporization (HOV), and vapor pressure. Measurement techniques for fuel properties are developed based on unit phenomena for liquid fuel droplets including droplet oscillation and evaporation.

For surface tension and viscosity predictions, the approach uses shape oscillation dynamics of single droplets generated by a piezo-electric device and their decay over time. Lamb's theory for small-amplitude droplet oscillations is utilized to calculate viscosity and surface tension. Measurements are obtained for both primary reference fuels (isooctane and *n*-heptane) and bio-derived candidate fuels from four functional groups of interest. Measurements results show that the droplet oscillation based approach is capable of reproducing surface tension and viscosity values for the tested fuels within deviations of 7% and 13% respectively from literature data. Results are obtained using an average of 5 μL per fuel sample per run within about 20 s.

For surface tension and viscosity prediction at elevated temperatures, the measurements show deviations within 10% of reference values obtained from the literature. The simulations are further used to study the relative contribution to deviations in surface tension and viscosity predictions due to heat and mass transfer from the droplet, as well as viscous effects violating the inviscid flow assumption in the droplet oscillation theory.

For HOV and vapor pressure predictions, evaporation of moving heated fuel droplets is studied. Measurement results for *n*-heptane, isobutanol, and PRF 84 are compared with literature data at different temperatures. The predictions of HOV and vapor pressure have

deviations within 10% and 22% respectively from literature data. Extended schemes are proposed involving additional measurements for droplet temperature and velocity. These extended schemes can potentially increase the number and accuracy of predicted fuel properties.

Chapter 1
Introduction

1.1 Background

Co-optimization of fuels and engines (Co-Optima) is a promising route that accelerates the introduction of advanced fuel and engine technologies [1]. Engine researchers are trying to find fuel properties that will improve efficiency and reduce emissions for light-duty gasoline fueled spark-ignition engines [2], while biofuel researchers are keen on discovering potential fuel candidates which can be renewably sourced, transported, stored, and marketed.

The Co-Optima program includes a layered screening process to identify potential biofuel candidates that can blend with gasoline to improve the efficiencies of spark ignition engines, particularly BSI (boosted spark ignition) engines [3]. The fuel screening process is shown in Figure 1.1. Fuels being down-selected are gasoline blendstocks with viable biomass-derived production pathways to incorporate renewable domestic biomass into the gasoline supply chain [4]. In tier 1 screening, 14 chemical families including alcohols, aromatics, ketones, esters, and furans from 470 blendstocks having viable production pathways from biomass were identified shown in Table 1.1. Tier 1 blendstocks were assessed concerning physical properties and combustion metrics. Tier 2 fuels were obtained by refining Tier 1 fuels. Tier 2 fuels were picked based on criteria such as melting/boiling point, solubility, corrosivity, toxicity, fuel handling/safety, biodegradation, and RON values (no less than 98). Tier 3 evaluation considers criteria including engine efficiency using the merit function, fuel-quality requirement by RVP, distillation, and commercialization possibilities. Both Tier 2 and Tier 3 focused on properties of fuel mixtures, which are combinations of different bioblendstock candidates with traditional gasoline fuels. The major goals of Co-Optima include fuel economy improvement by 10% for light-duty vehicles using boosted SI engines surpassing the projected values of existing research efforts, improving fuel economy by 4% for heavy-duty vehicles, providing 25 billion gallons/year of US sourced fuels, and

reducing emissions [1].

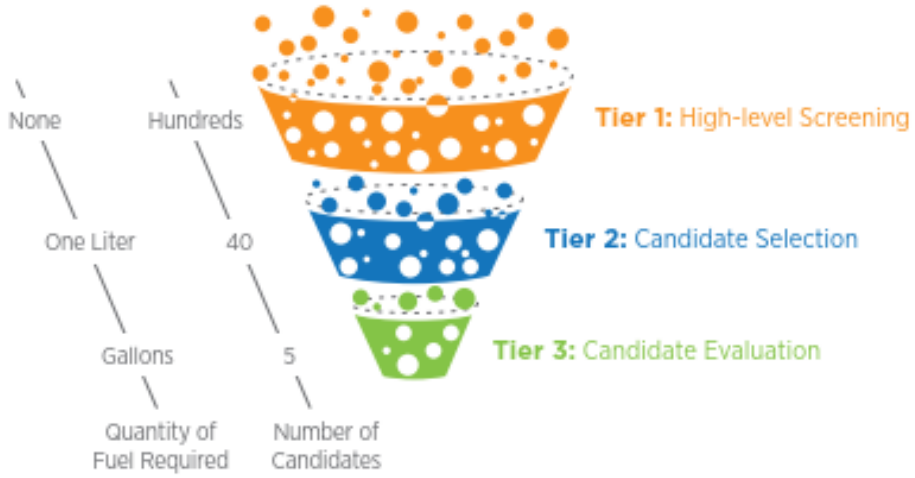

Figure 1.1. Three-tier evaluation procedure for fuel down selection [4].

Table 1.1. 14 Chemical families in Tier 1 screening.

1	**2**	**3**	**4**	**5**	**6**	**7**
Normal paraffins	iso-Paraffins	Olefins	Aromatics	Naphthenes	Alcohols	Ketones
8	**9**	**10**	**11**	**12**	**13**	**14**
Fatty acid esters	Furans	Ethers	Multi-ring aromatics	Aldehydes	Fatty esters	Carboxylic acids

Although DOE (Department of Energy) researchers as part of the Co-Optima program are working on the determination of candidate bioblendstocks for detailed investigation through engine tests [5], it is imperative to utilize fast screening approaches to discover the suitability of candidate biofuels by evaluating physical and combustion specific properties at engine relevant operating conditions. The fast screening approach measures the physical properties of the fuel using minimal volume, which is much more efficient than doing engine tests using a large pool of potential biofuel alternatives. This approach is suitable for cases when there is a limited quantity of fuel samples available. High throughput and small sample size ($\mathcal{O}(\mu\text{l})$) are two desirable features for fast screening tests. The screening tools aim to measure physical and combustion specific properties as relevant to the combustion of biomass derived fuels in DI gasoline engines. While several properties are relevant to fuel

spray generation and combustion, the properties of interest in this work include viscosity, surface tension, HOV, and vapor pressure.

These properties impact fuel injection, atomization, vaporization, and combustion processes, resulting in changes in engine performance and emissions. Figure 1.2 shows a depiction of a series of processes inside a diesel engine including fuel injection, spray formation and atomization, vaporization, fuel and air mixing, and combustion. Similar in-cylinder processes also occur in the case of direct-injected spark ignition engines. Surface tension and viscosity affect spray formation and atomization, while HOV and vapor pressure directly impact vaporization. Fuel surface tension is related to spray breakup, which manifests through the Weber number (We=$\frac{\rho V^2 D}{\sigma}$), which shows the ratio of inertial to cohesive forces. Fuel viscosity is related to spray penetration and angle represented by the Reynolds number (Re=$\frac{\rho V D}{\mu}$). Once the fuel is atomized into droplets, evaporation, and fuel/air mixing processes occur and are directly coupled to the HOV and vapor pressure of the fuel [6]. HOV or latent heat is the energy required for the phase change of the liquid fuel. Vapor pressure shows the pressure exerted by the fuel vapor in thermodynamic equilibrium with its liquid phase.

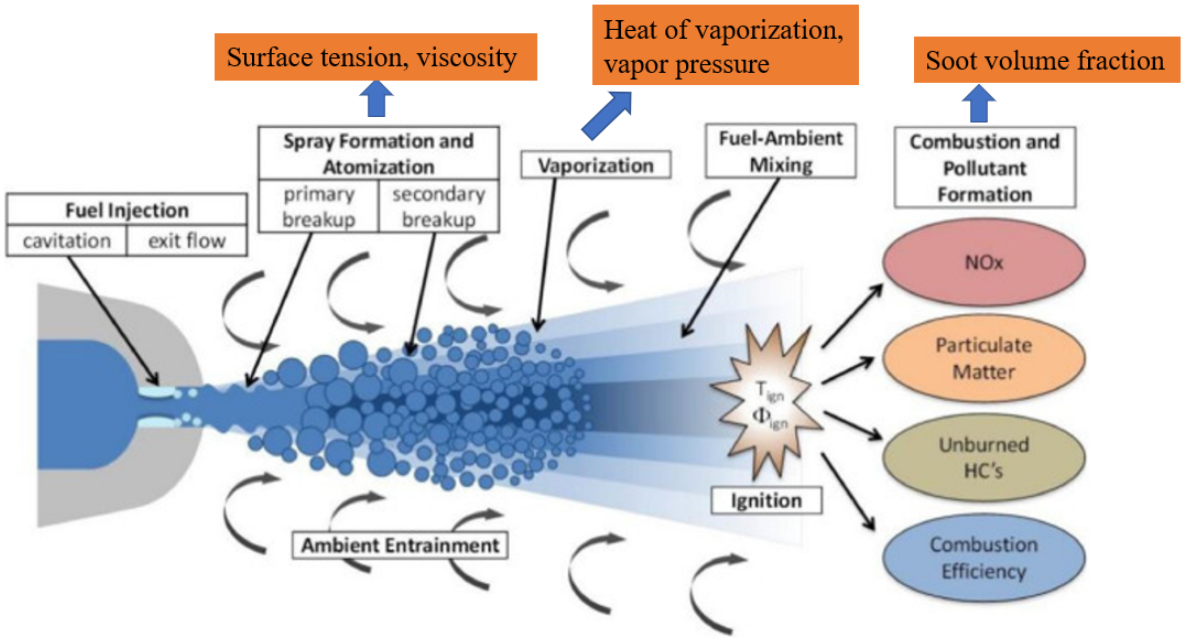

Figure 1.2. Fuel physical properties with respect to engine process [7].

1.2 Research Motivation

The development of biomass-derived fuels to serve as drop-in replacements or blending components with conventional transportation fuels requires small-volume, high-throughput measurement techniques for fuel physical properties with relevance to engine spray and combustion processes. These techniques should be capable of achieving sufficient accuracy and sensitivity to detect the influence of fuel composition changes. The techniques should further be able to investigate physical property dependence on temperature and pressure as relevant to in-cylinder, engine operating conditions. Finally, measurement techniques should have the ability to be integrated with companion tools being developed for combustion specific metrics. This work is motivated by the desire to develop droplet-based techniques to measure fuel physical properties through various unit phenomena exhibited by single droplets including oscillation, and evaporation at ambient and elevated temperatures.

1.3 Research Objectives

1. Study unit droplet phenomena including droplet oscillation, and evaporation with relevance to transportation fuels having known physical properties. The phenomena will be studied using experimental, analytical, and simulation techniques.

2. Develop experimental setups capable of observing and measuring unit droplet phenomena and use measurement data with analytical models and simulations to derive unknown physical properties for biomass-derived fuels.

3. Evaluate temperature and pressure dependence of fuel physical properties at conditions relevant to transportation fuels.

4. Implement measurement techniques into small-volume, high-throughput screening processes for emerging biomass-derived fuels with accuracy and sensitivity levels sufficient to detect fuel compositional change and impact on engine spray processes.

1.4 Literature Review

The need to search for biofuels that can be used in engines is pressing due to deteriorating climate change, increasing exhaustion of fossil fuels, and the rising demand for energy in this world. One of the ways to identify the most feasible biofuel candidates for gasoline engines is to measure the physical properties of candidate fuels that are closely associated with engine performance.

1.4.1 Surface Tension and Viscosity

Surface tension is closely related to secondary break-up in the stage of spray formation and atomization. After the primary separation of ligaments from the liquid jet, the ligaments are disintegrated and smaller fuel droplets are formed. During this process, surface tension appears strong enough to counter the disruptive inertial forces [8]. This secondary break-up sets the stage for the subsequent evaporation and combustion. Davanlou et al [9] found the spray angle increases sharply if the surface tension is reduced. The value of spray angle demonstrates how much gas has entrained into a spray, which controls the extent of fuel-air mixing, vaporization, combustion, the formation of NOx, and PM (particulate matter) emissions [10].

Surface tension also affects droplet size at low injection pressure. But at high injection pressure or high Reynolds number, the impacts of surface tension on droplet size changes are not obvious. The modes of break-up can either introduce some oscillations to the droplets or tear apart the droplet. Weber number (We), the ratio between inertial and surface tension, can be used to show different types of break-up modes. Figure 1.3 depicts a classification of secondary droplet break-up mode. The understanding of the break-up phenomena helps improve fuel efficiency, reduce combustion instabilities, and decrease exhaust gas emissions [11].

Viscosity is another important physical property closely related to fuel spray processes inside the engine. Mägi [8] found that bigger droplet sizes are formed when the viscosity is higher. Lefebvre and Ballal [13] mentioned the reason for larger droplet size for liquids with

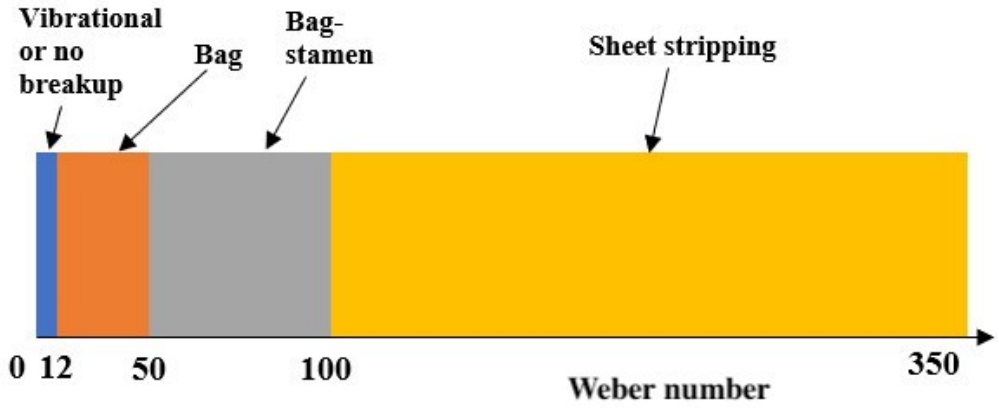

Figure 1.3. Weber number with respect to secondary droplet break-up mode [8, 12].

a higher viscosity to be related to the competition between aerodynamic forces (disruptive) and surface tension/viscosity (consolidating). Viscosity dampens the surface waves before the start of atomization. Yue and Som [14] analyzed the effects of surface tension, viscosity, and density on spray atomization process in Gasoline Direct Injection Engines using CFD (Computational Fluid Dynamics). They found spray gave 12% higher injection velocity and 5% lower mass flow rate compared with ethanol due to higher viscosity and density of the ethanol. Since the injection velocity is inversely proportional to $\sqrt{\rho}$, while the mass flow rate is proportional to $\sqrt{\rho}$ based on Bernoulli's equation for inviscid fluid with constant pressure drop. So higher density ethanol has lower injection velocity, but higher mass flow rate. Also, higher viscosity leads to lower injection velocity and mass flow rate because of higher friction forces compared with inviscid fuels. For lower viscosity fuels, a larger spray angle with increasing Reynolds number is to be expected [15]. Since there are stronger interactions between fuels and air for lower viscosity cases. Higher viscosity liquids with high injection pressures lead to larger droplet size during the breakup stage and the coalescence regime is postponed [9].

Consequently, for fuels having higher viscosity and lower Re, spray penetration as well as spray angle decreases. For fuels having higher surface tension, We number decreases and results in the poor breakup of the spray. Increasing Re and We promotes an increase in inertial forces leading to improved spray plume penetration and breakup.

According to the DOE Co-optima report in 2019 [16], the dynamic viscosity at 25°C for the top ten bioblendstocks for turbocharged gasoline engines with potential for highest engine efficiency is from 0.5 to 4.0 cSt, while the surface tension is in the range between 21 and 34 mN/m. The maximum dynamic viscosity at 25°C for the biodiesel used in compression-ignition engines can go up to 6-12 cSt [17, 18, 19], while the surface tension is about 25-33 mN/m [20, 21].

Temperature inversely affects fuel surface tension and viscosity. Both of these physical properties decrease as temperature increases [22, 23]. Temperature dependency of physical properties is more pronounced for biofuel based molecules, which are often hydrogenated or oxygenated. The sizes of biofuel based molecules are typically larger than conventional hydrocarbon fuel molecules. For fuels with higher density, surface tension, and viscosity, they require the use of preheating in some cases to reduce the values of those properties so that spray atomization and breakup processes can proceed optimally [24]. Fajgenbaum [25] found the temperatures during port fuel injection for gasoline and ethanol to range from 15 to 55°C. Fuel temperature during port injection can affect atomization parameters [25]. Aleiferis [26] found the fuel temperature range for a multi-hole injector with E85 and gasoline is between 20 and 120°C. Marriott et al [27] reported droplet sizes of gasoline and E85 are in the range 10–25μm using an 8-hole injector with injection fuel pressures at 110 bar and 200 bar, and fuel temperature is between 20 and 90°C.

Traditional popular ways for surface tension measurement depicted in Figure 1.4 include the methods of the du Noüy ring [28], the Wilhelmy plate [29], and the Pendant droplet [30].

$$P_{tot} = P_R + 4\pi R \cdot \gamma_{ideal} \tag{1.1}$$

$$\gamma = f\gamma_{ideal} \tag{1.2}$$

Both of the du Noüy ring and the Wilhelmy plate methods involve pulling an object with either a ring or plate shape geometry on the surface of liquids and measuring the

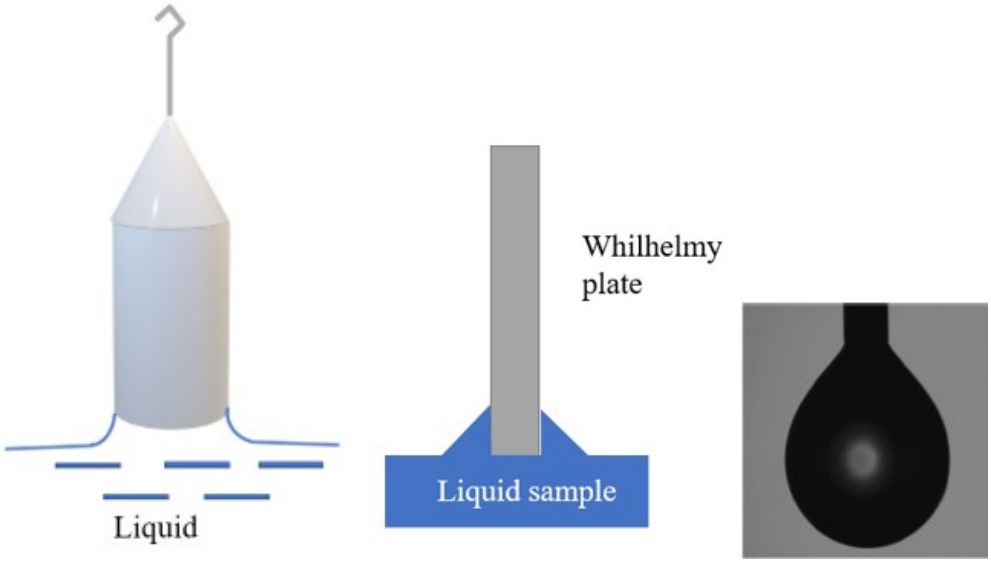

(a) Du Noüy ring method (b) Wilhelmy plate (c) Pendant droplet

Figure 1.4. Popular surface tension measurement methods.

pulling force [31]. Both of these methods have the total force term P_{tot}, which can be measured through connection to another object based on force balance. Eq. 1.1 and Eq. 1.2 show the mechanism of du Noüy ring method by equating the sum of the weight of the ring and the surface tension of the liquid to the total force on the ring (P_{tot}). P_R is the weight of the ring, R is the radius of the ring, f is the correction factor based on the shape of the ring, which has been defined by Padday, Harkins, Freud et al [32, 33, 34]. γ is the surface tension that needs to be calculated.

$$P_{tot} = P_P + c\gamma + \rho ghA \tag{1.3}$$

Eq. 1.3 shows the mechanism of the Wilhelmy plate method. c is the circumference of the plate. A is the area of the plate facing the fluid surface. h is the height relative to the fluid level.

The du Noüy ring and the Wilhelmy plate are force-based methods, while the pendant droplet method uses the Young-Laplace equation to determine surface tension through the shape changes of the pendant droplet. As per Eq. 1.4, Young-Laplace equation describes the profile of a pendant droplet [35]. $\Delta\rho$ is the density difference between the droplet and

the surrounding gas, R_o is the radius of the droplet curvature at the droplet apex, and β is the shape factor that can be calculated using Eq. 1.5 [36].

$$\gamma = \frac{\Delta \rho g R_0^2}{\beta} \tag{1.4}$$

$$\beta = 0.02664 + 0.62945 s^2 \tag{1.5}$$

where s=D_s/D_E, D_E is the maximum diameter of the pendant droplet in the horizontal direction, D_s is the droplet diameter in the horizontal direction at the vertical distance D_E from the droplet apex point [35]. The sketch for the parameters that need to be measured in the pendant droplet method is shown in Figure 1.5.

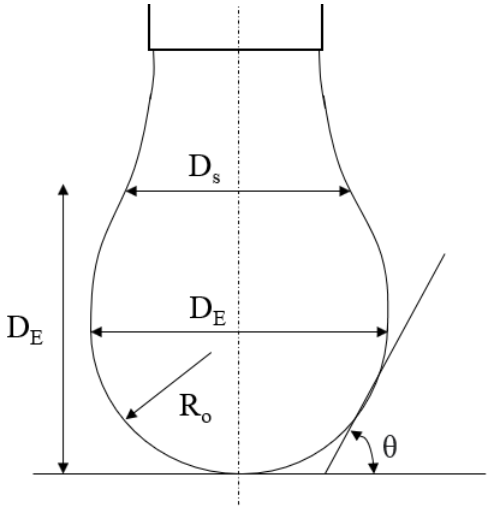

Figure 1.5. Sketch showing the parameters in pendant droplet method.

One of the best tensiometers on the market is equipped with the Wilhelmy technique (Kibron, Model Ez-Pi+), which requires a 0.5 mL sample and can get results of surface tension measurements in 30 s. The traditional way for viscosity measurement is to use a viscometer. One of the best viscometers on the market (Brookfield instruments, CAP1000+) can operate with less than 1 μL samples. Some researchers have used droplet shape oscillation dynamics to measure both surface tension and viscosity [37, 38, 39, 40, 41] either by using free-falling or levitated droplets.

At elevated temperature conditions, the measurement of temperature dependency of

surface tension and viscosity has been carried out with a traditional setup using the pendant droplet method [42], pendant/sessile drop combined method [43], and the differential maximum bubble pressure method [44]. The damping of the oscillation is closely related to temperature change and evaporation rate from numerical analysis [45].

1.4.2 Heat of Vaporization (HOV) and Vapor Pressure

Miles [46] introduced "revised merit function" as shown in Eq. 1.6 to evaluate the potential thermal efficiency of candidate fuels with different fuel properties and determine potential improvements in engine efficiency. Properties that are embedded in Eq. 1.6 include anti-knock index (AKI) of 87 E10 gasoline with research octane number (RON) of 91 and a motor octane number (MON) of 83. This leads to a sensitivity (S=RON-MON) of 8.

$$\begin{aligned} Merit = & \frac{(RON_{mix} - 91)}{1.6} - K\frac{(S_{mix} - 8)}{1.6} \\ & + \frac{0.085[ON/kJ/kg] \cdot ((HOV_{mix}/(AFR_{mix} + 1)) - (415[kJ/kg]/(14.0[-] + 1)))}{1.6} \\ & + \frac{((HOV_{mix}/(AFR_{mix} + 1)) - (415[kJ/kg]/(14.0[-] + 1)))}{15.2} \\ & + \frac{(S_{Lmix} - 46[cm/s])}{5.4} - H(PMI_{mix} - 1.6)[0.7 + 0.5(PMI_{mix} - 1.4)] \\ & + 0.008°C^{-1}(T_{c,90,conv} - T_{c,90,mix}) \end{aligned} \tag{1.6}$$

Where S_L is flame speed, AFR is the stoichiometric air-fuel ratio, and PMI is the particulate matter index.

As one of the terms in the merit function, HOV is an important physical property for engine efficiency assessment. The fuel droplet evaporation process impacts the values of HOV. The energy required for evaporation is provided by the ambient air surrounding the droplets in the engine cylinder. During evaporation, the temperature of the ambient air inside the cylinder reduces, which results in improved volumetric efficiency of gasoline engines [47]. HOV of fuel impacts evaporative cooling and also has a pronounced effect on knock suppression in direct-injected (DI) gasoline engines. Previous studies conducted on downsized boosted engines have shown that evaporative cooling provides an equivalent

effect of increasing the octane number of the fuel by about 5 units, which leads to an increase in compression ratio by 1 unit [48]. Increasing RON and S improves the knock resistance, which is commonly expressed in Eq. 1.7 through the octane index (OI) [49]. Higher HOV reduces charge temperature, and thus improves fuel anti-knock properties. This is directly evidenced by numerous studies considering the impact of ethanol and other alcohol blends on engine knock [48, 49, 50]. Knock mitigation allows a higher compression ratio to be used, which increases engine efficiency.

$$OI = RON - K \cdot S \tag{1.7}$$

where RON is the Research Octane Number and S is the octane sensitivity (RON-MON). K is an engine constant that depends on the pressure-temperature history of the unburned charge in the engine cylinder and typically has negative values at the most knock limited operating conditions. Although K is not a physical property of fuel, it is impacted by fuel composition and HOV. Higher HOV reduces charge temperature, leading to more negative values of K, and thus improves fuel anti-knock properties.

Given the importance of HOV on fuel combustion, evaporation, and transportation, suitable approaches are needed to get high-accuracy HOV measurements. Previous methods using the Clausius-Clapeyron equation from vapor pressure were able to get HOV for pure substances and ideal mixtures with high accuracy. But for non-ideal mixtures which cannot be defined by Raoult's law, vapor pressure and HOV predictions have higher error than ideal mixtures [51]. Methods for successful HOV measurement include a DSC/TGA (Differential Scanning Calorimetry/Thermogravimetric) approach [52]. The limitations of measuring HOV using DSC/TGA include the mass loss of the sample before the starting of the measurement [53].

Vapor pressure is another essential property that measures the pressure exerted by a vapor of a pure compound in thermodynamic equilibrium with its liquid phase at a specific temperature in a closed system [54]. Vapor pressure is widely used in assessing the quality

of gasoline along with other quantities such as distillation parameters, specific gravity, octane number, and octane index. Vapor pressure is directly related to the volatility of the fuel and has a direct influence on engine performance as well as fuel production and transportation logistics. Fuel vapor pressure is required to meet specific standards to ensure safety considerations in the transport and storage of fuels to avoid accidents and minimize losses through evaporation. Fuels with lower vapor pressure are harder to vaporize resulting in poor combustion efficiency [55]. On the other hand, fuels with high vapor pressure can generate volatile organic compounds leading to an uncontrolled air-fuel ratio affecting the combustion process. These considerations have made it a requirement to maintain fuel vapor pressure within an acceptable range.

The vapor pressure in the fuel industry is often being reported as Reid vapor pressure (RVP), which refers to the vapor pressure measured at 100°F (37.8°C) in a chamber with a volumetric ratio of 4:1 of vapor/liquid. RVP of alcohol gasoline blends (non-ideal mixtures) is higher than ideal mixtures or gasoline itself [56]. RVP links to cold-start and warm-up driveability. The usage of fuel with higher RVP can improve the fuel vaporization in a cold environment [57]. Volatility is a key gasoline characteristic for good driveability, which shows how gasoline inclines to vaporize. Gasoline fuel vaporization is the prelude to fuel combustion in the engine. As one of four properties for gasoline volatility measurement, vapor pressure is an important metric. The other three properties include distillation profile, vapor-liquid ratio, and driveability index. To achieve a good cold-start performance, higher values of vapor pressure are essential. But higher vapor pressure may increase VOC (Volatile Organic Compounds) and CO (Carbon Monoxide) emissions. Lower values of vapor pressure are suitable for the prevention of vapor lock issues. Vapor pressure would increase if blending ethanol with hydrocarbon-only gasoline. For example, 5.7% ethanol blending with 75% hydrocarbon only gasoline makes the vapor pressure increase by about 6.2 KPa when the original hydrocarbon gasoline has a vapor pressure of 48.3 KPa [58].

Table 1.2 shows three key stages of fuel RVP measurement histories from 100 years ago

Table 1.2. The evolution of RVP measurement schemes.

Stages	Years	Method	Sample size (mL)
1	**1920 - 1989**	Reid method and dry Reid method	100
2	**1990 - 1998**	Miniaturized method	1-10
3	**1999 - Now**	Triple expansions method	5-15

till today. At the beginning stage of RVP measurement, the major method is called the "Reid method and dry Reid method". At that time, only traditional hydrocarbon gasoline can be measured by ASTM D323 method. ASTM D323 is used as a measurement guide for gasoline and petroleum product through a sealed chamber with a vapor-to-liquid volume ratio of 4:1 at 100°F (37.8°C). A pressure gauge is used in the chamber to measure the vapor pressure, which is RVP. This method requires the pre-cooling of the samples before sending them into the sealed chamber. The second stage of RVP measurement uses the "Miniaturized method". From ASTM D5191, a miniaturized apparatus is applied and needs only 10% of the sample volume that is required by ASTM D323. The third stage from 1999 till today uses the "Triple expansions method" based on ASTM D6378 for determining the dissolved air in a sample. Both traditional gasoline and oxygenated gasoline/renewable fuels can be measured without prior cooling or drying during sample preparation. Also, the required sample size reduces from 100 mL to less than 10 mL [16]. The above-mentioned RVP measurement methods require a large sample size ($\mathcal{O}(ml)$). It may not be suitable to use for the cases when the fuel sample volume is limited, such as within ($\mathcal{O}(\mu l)$).

1.5 Outline of Manuscript

This thesis describes fuel physical property measurement techniques based on micron-sized droplets falling in quiescent air. Chapter 1 introduces the background of the research topics and the outline of this thesis. Chapter 2 describes surface tension and viscosity measurement for pure fuels at ambient temperature using droplet shape oscillation. Chapter 3 shows surface tension and viscosity measurement for pure fuels and fuel blends at elevated temperatures. Chapter 4 includes the heat of vaporization and vapor pressure

measurement using isothermal droplet evaporation simulation and experiments. Chapter 5 describes conclusions based on current research results and plans for future work.

Chapter 2
Droplet-based Surface Tension and Viscosity Measurement at Ambient Conditions

A droplet dynamics based approach is utilized to evaluate fuel surface tension and viscosity at atmospheric conditions. Two key considerations for the measurement approach are to operate with small volumes of high volatility liquid fuels ($\mathcal{O}(\mu l)$) and to achieve high throughput. These features would allow the measurement approach to enable the screening of emerging fuel blends, made available in limited quantities prior to further development. Several examples of techniques using droplet dynamics to measure physical properties of various fluids can be found in literature including those by [37, 38, 39, 40, 41, 59]. This chapter describes the theory of droplet oscillation dynamics, the experimental setup, and the results of experiments.

2.1 Theory

2.1.1 Droplet Oscillation Theory

The study of droplet oscillation in motion is of interest in this work because both surface tension and viscosity values can be calculated by observing the decay of the oscillation amplitude. Once a droplet pinches off from the nozzle orifice, the process of droplet deformation and restoration follows the response of a damped oscillator [60, 61]. Surface tension acts as a restoring force to maintain the mechanical equilibrium of the droplet after the application of an external perturbation. The rate at which the oscillation is damped is closely related to viscosity. For an isolated liquid droplet undergoing small-amplitude axisymmetric oscillation, the droplet shape, $R(\theta, t)$ as shown in Figure 2.1, can be described by [59, 60, 62],

$$R(\theta, t) = R_0 + \xi = R_0 + S_n \cdot sin(\omega_n t + \epsilon) = R_0 + \sum_{n=2}^{\infty} A_n(t) P_n(cos\ \theta) \tag{2.1}$$

This chapter was previously published as Dang, W., Zhao, W., Schoegl, I., & Menon, S. (2020). A small-volume, high-throughput approach for surface tension and viscosity measurements of liquid fuels. Measurement Science and Technology, 31(9), 095301. Reprinted with permission from IOP Publishing.

In Eq. 2.1, θ is the polar angle, R_0 is the initial radius of a spherical droplet at equilibrium free from other forces except surface tension, ξ is the surface deformation, S_n is a surface-harmonic of order n, which consists of Legendre polynomials P_n, ω_n is the oscillation frequency of the n^{th} mode, and ϵ is the phase shift, and $A_n(t)$ are the surface mode amplitude coefficients.

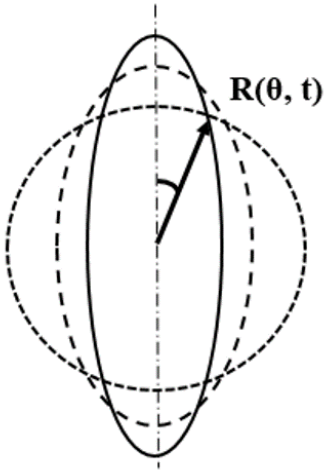

Figure 2.1. Sketch showing the variation of the droplet radius as a function of time and polar angle due to droplet oscillation.

Lamb [61] expressed the generalized linear solution for a free oscillating droplet with small-amplitude including the influence of the surrounding medium. The oscillation frequency of the n$^{\text{th}}$ mode, ω_n, is:

$$\omega_n^2 = (2\pi f_n)^2 = \frac{n(n-1)(n+1)(n+2)\sigma}{R_0^3\left[(n+1)\rho_l + n\rho_a\right]} \tag{2.2}$$

In Eq. 2.2, ρ_l is the density of droplet, ρ_a is the density of ambient air, n is the number of oscillation mode, and σ is the surface tension of the droplet. The viscous effects are introduced by Lamb who provided the following decay time constant, τ,

$$A_n(t) \propto e^{-\frac{t}{\tau}}, \text{ where } \tau = \frac{1}{(n-1)(2n+1)}\frac{\rho_l R_0^2}{\mu_l} \tag{2.3}$$

In Eq. 2.3, μ_l is the dynamic viscosity of the droplet. By measuring the decay time

constant τ and the oscillation frequency ω_n, viscosity and surface tension can be estimated after substituting the droplet and ambient densities into Equations 2.2 and 2.3.

2.1.2 Impacts of Temperature and Pressure on Surface Tension and Viscosity

As shown in Figure 2.2, surface tension and viscosity are dependent on temperature. As temperature increases, both surface tension and viscosity decrease. Temperature effects on surface tension and viscosity will be discussed in the next chapter.

The dependency of surface tension and viscosity on pressure is negligible within a pressure range from 0 to 30 bar as shown by Figure 2.3.

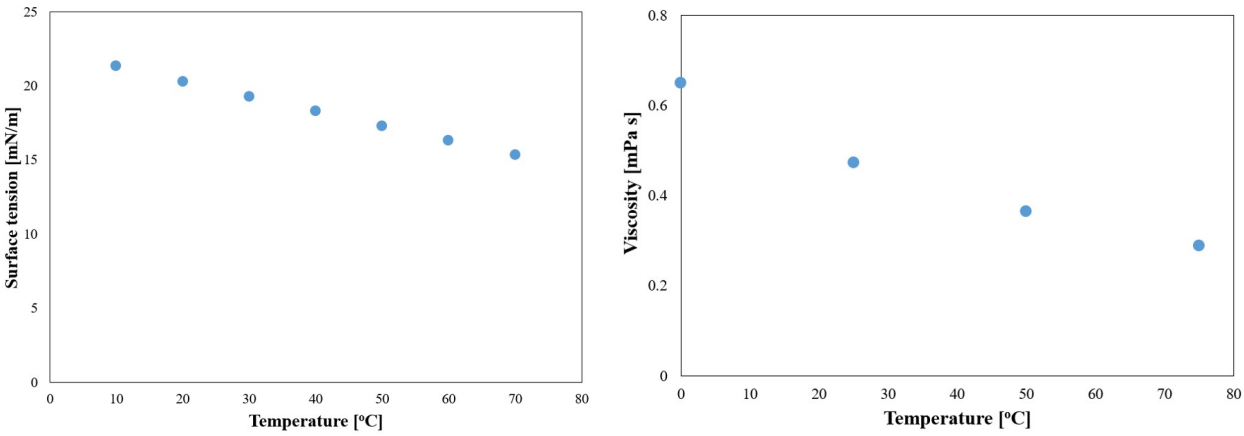

(a) n-heptane surface tension vs temperature [63].

(b) viscosity vs temperature [64].

Figure 2.2. Temperature impacts on surface tension and viscosity.

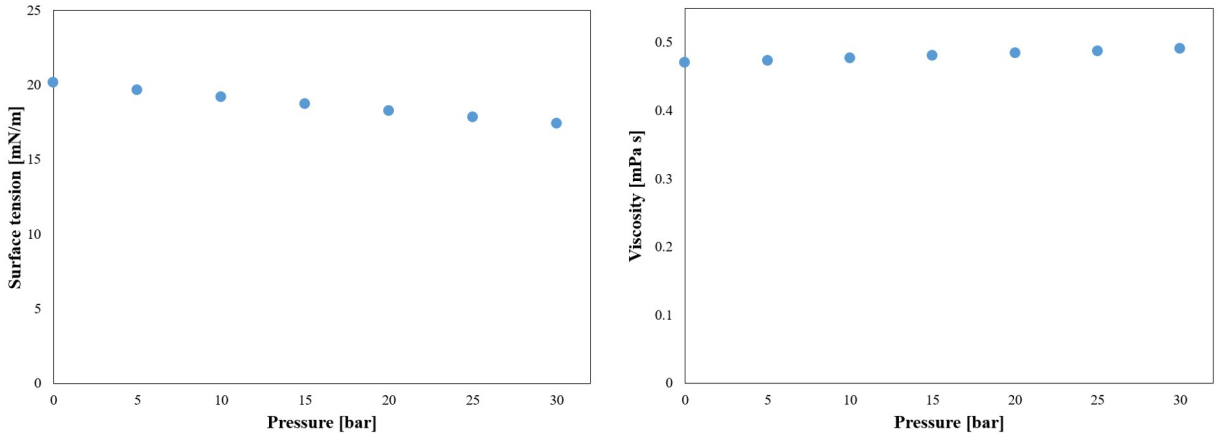

(a) n-heptane surface tension vs pressure [65].

(b) viscosity vs pressure [64].

Figure 2.3. Pressure impacts on surface tension and viscosity.

2.2 Experiment

2.2.1 Droplet Generation System Setup

Figure 2.4 shows details of the major components of the experimental setup, which include droplet generator, imaging components, pressure controller, vacuum pump, and signal generator. When the piezoelectric droplet generator (MicroFab PH-47) senses an external voltage pulse from the signal generator (Microfab JetDrive V (CT-M5-01)), the piezoelectric actuator expands or contracts according to the polarity of the waveform. This results in the generation of a droplet trail at the exit plane of the nozzle. A pressure controller (MicroFab CT-PT-21) is used to provide stabilizing back pressure to sustain a balanced force at the meniscus. The pressure controller is connected to a vacuum pump (Koge electronic, KPV20A-6A) and a compressed air source (Ultra-pure carrier grade air) allowing it to maintain positive or negative back pressure.

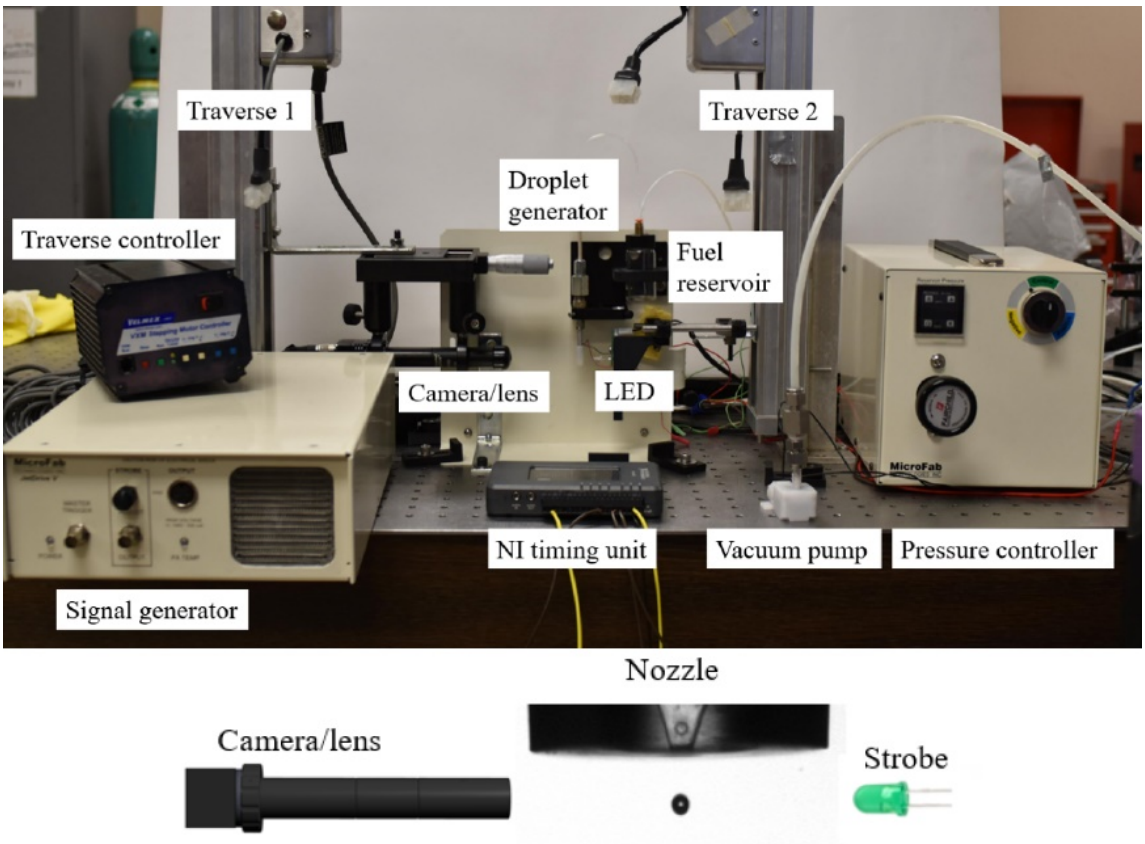

Figure 2.4. Experimental setup (Top); Droplet generator nozzle, strobe, and camera (Bottom, not to scale).

The reason for choosing a 30 μm nozzle based droplet generator originates from the estimation of 2 μl/min fuel volume flow rate that was dictated by a continuous micro-combustion apparatus for the measurements of fuel physical properties and combustion metrics [66]. Figure 2.5 shows the ranges for droplet diameters and jetting frequencies that are compatible with 2 μl/min flow rate target at 2 bar condition. 2 μl/min flow rate is guaranteed when the jetting frequency is between 100 Hz and 2 kHz and droplets sizes range from 35 to 60 μm in diameter. The frequency of the waveform pulse controls the droplet spacing.

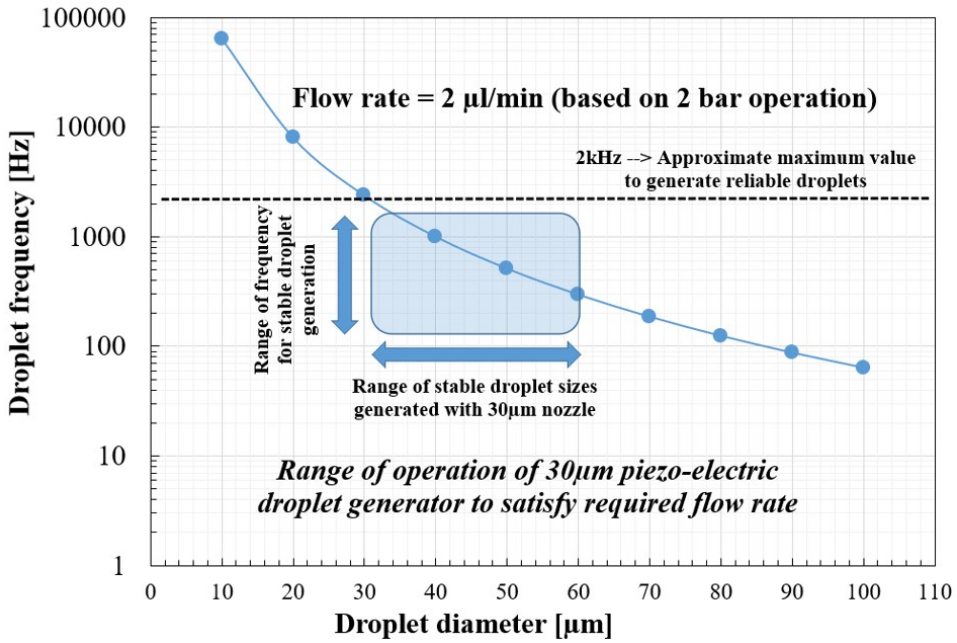

Figure 2.5. Fuel flow rate determines the selection of nozzle size.

For a droplet with 40 μm diameter and 2 μl/min flow rate, the uncertainty of flow rate is correlated with the uncertainty of droplet diameter as Figure 2.6 describes. Given that the uncertainty of droplet diameter measurement for a 40 μm diameter droplet is within 3.5% using the current camera/lens system having a resolution of 1.34 μm/pixel, the uncertainty of the corresponding volume flow rate is within 11%.

- **2.2.1.1 Droplet Generator**

Figure 2.7 and Figure 2.8 show a schematic and mechanism of the piezoelectric droplet generator, which include the driving waveform pattern, internal structure of piezoelectric

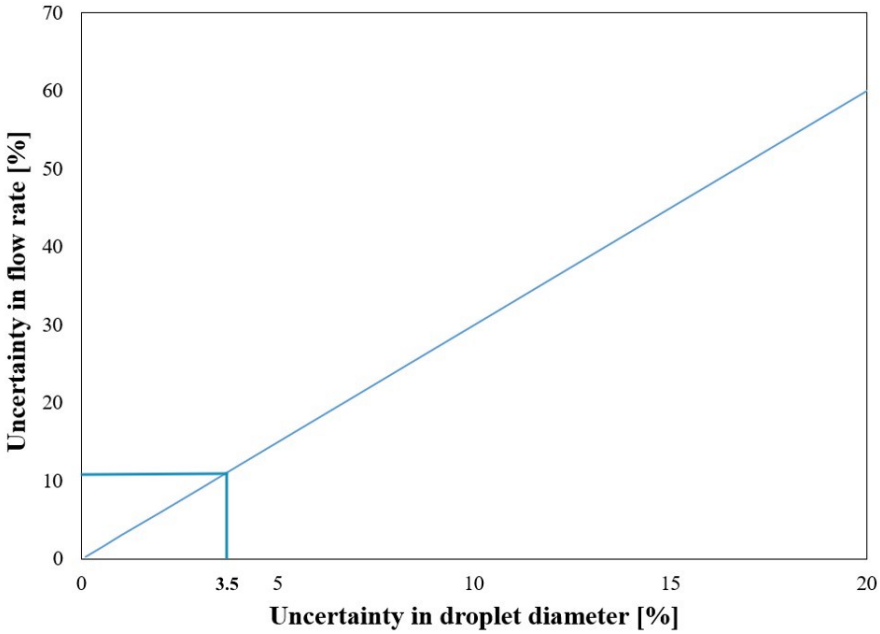

Figure 2.6. Uncertainty in flow rate with respect to uncertainty in droplet diameter.

droplet generator, and mechanism of the droplet generation. The waveform input to the droplet generator can be either unipolar or bipolar. As the voltage of the waveform increases, the piezoelectric material inside the droplet generator expands and the meniscus retracts due to reduced back pressure. As the voltage of the waveform stays steady, the expansion wave travels inside the glass tube that connects with the nozzle. As the voltage of the waveform reduces, the piezoelectric material compresses the glass tube while the droplet is ejected and leaves the nozzle orifice. As Figure 2.7 (b) shows, the piezoelectric material wraps around the inner glass tube so that the pressure wave can transport directly from the piezoelectric material to the inner glass tube. With the continuous expansion and contraction of the inner tube at prescribed operating parameters, a stable droplet trail is formed.

When the droplet generator senses an external voltage pulse from the signal generator (Microfab JetDrive V (CT-M5-01), as shown in Figure 2.8, the piezo element could either pull or push the fuel in the glass tube and nozzle, according to the polarity of the waveform. At the same time, the meniscus is pulled back or pushed forward, which results in the generation of a droplet train at the exit plane of the nozzle as Figure 2.9 shows.

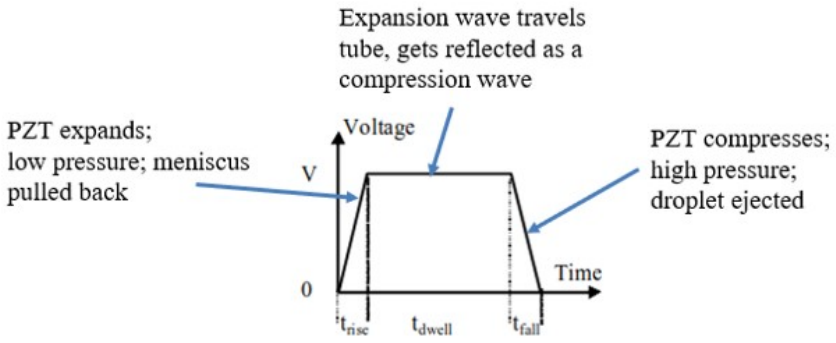

(a) Waveform applied to piezoelectric droplet generator.

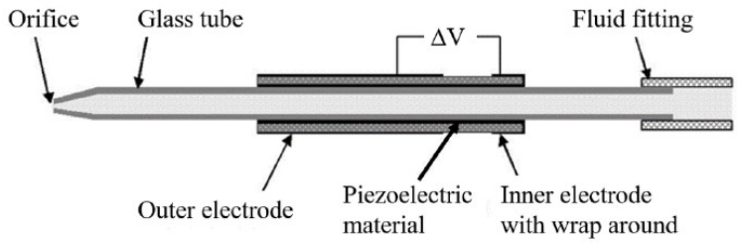

(b) Schematic of the piezoelectric droplet generator.

Figure 2.7. Droplet generator driving waveform and inner structure.

- **2.2.1.2 Imaging**

A monochrome CCD camera (STC-MB33USB) along with a telecentric lens (6X, 65mm WD Edmund Optics CompactTL) giving a resolution of 1.34 μm/pixel is mounted on a vertical traverse and used to obtain high-resolution images of the droplets. DOF (depth of field) of the telecentric lens is 50 μm, which is suitable for cases when the droplet displacement from the centerline is small. Given that droplet oscillation happens adjacent

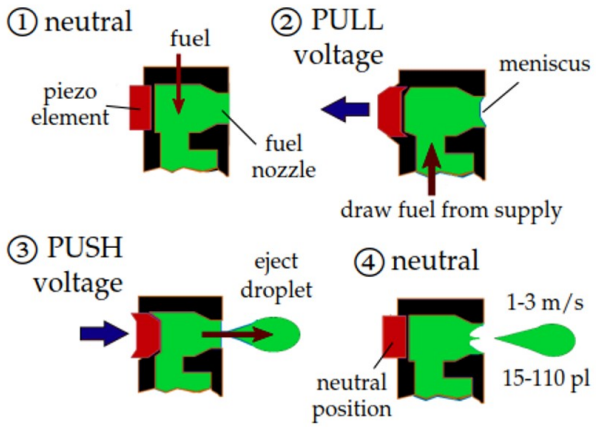

Figure 2.8. Mechanism of piezoelectric droplet generator.

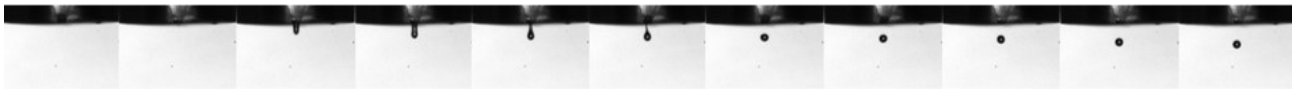

Figure 2.9. Droplet injection sequence of isobutanol at 22°C.

to the starting point of droplet generation near the nozzle orifice, the movement of the droplet can be well captured by the current lens/camera system. A green LED strobe (Broadcom HLMP-CM1A-560DD) located across from the lens and mounted on another vertical traverse is the light source for the camera. A green LED is chosen since the camera sensor reaches its highest spectral sensitivity at a wavelength of 500-520 nm. A transistor circuit is used to magnify the voltage across LED as shown in Figure 2.10. The transistor is PNP with part number 2N3906. Without the transistor circuit, the voltage across LED is about 1.2V. With the transistor circuit, the voltage across LED can go up to 2.1V. So the brightness of LED increases dramatically when using the transistor circuit. This setup provides high contrast droplet images by increasing the intensity gradient between droplet edge and background. Data acquisition primarily consists of capturing droplet images undergoing oscillation in flight using a stroboscopic approach. A time history of the droplet oscillation is generated by acquiring images of successive droplets in various stages of oscillation by progressively incrementing the delay between the jetting signal and the start of camera recording. The implementation and details of this technique are explained in more detail in Section 2.2.3.

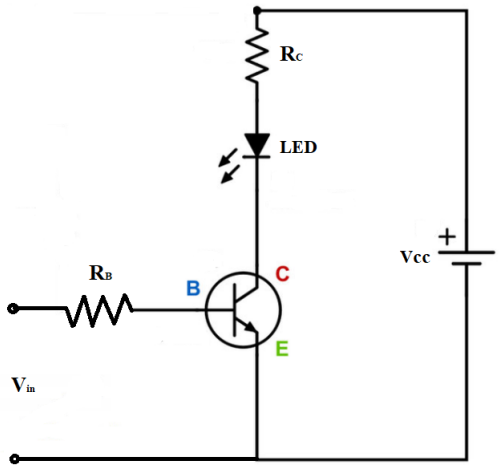

Figure 2.10. Transistor circuit for a brighter LED.

2.2.2 Operating Parameters for Stable Droplet Generation

Stable droplet generation is associated with correct setting of operating parameters in JetServer 4 software. The parameters determine the waveform applied to the piezoelectric actuator. By adjusting the values of operating parameters, the amplitude and shape of the waveform would change accordingly. As a result of parameters adjustment, either a stable droplet trail with measurable droplet sizes and velocities is formed, or no droplet is generated due to unbalanced pressure at the meniscus of the nozzle exit plane. The way to control the waveform parameters for jetting is through the adjustment of operating parameters on the panel of JetServer 4 software as shown in Figure 2.11. The key operating parameters that have significant influences on droplet size and velocity include the applied (driving) voltage and dwell time. Other parameters, such as jetting frequency and rise/fall time, have much smaller impact on droplet size and velocity.

Figure 2.11. Screenshot of Microfab's JetServer 4 software.

An experimental parametric study has been performed to present the impact of the applied voltage and dwell time on droplet size and velocity while the droplet moves. The experimental results in this work are shown in the following Figure 2.12, 2.13, 2.14, and

2.16. Figure 2.12 shows how the applied (driving) voltage and droplet velocity change with strobe delay times. It is obvious to see the higher the applied voltage, the larger values of droplet velocities will be obtained. Since higher voltage means larger deformation of the piezoelectric material, which leads to higher momentum of the ejected droplet. Strobe delay values show the time progression after the droplet leaves the nozzle and are proportional to the distance that a droplet travels. During droplet falls in a trajectory, the cases with higher applied voltages would have higher velocities than cases with lower applied voltages at a certain time or location. Figure 2.13 shows at 400 μs, three fuels (IPA, , and n-heptane) with increasing applied voltages lead to the increases in droplet velocities.

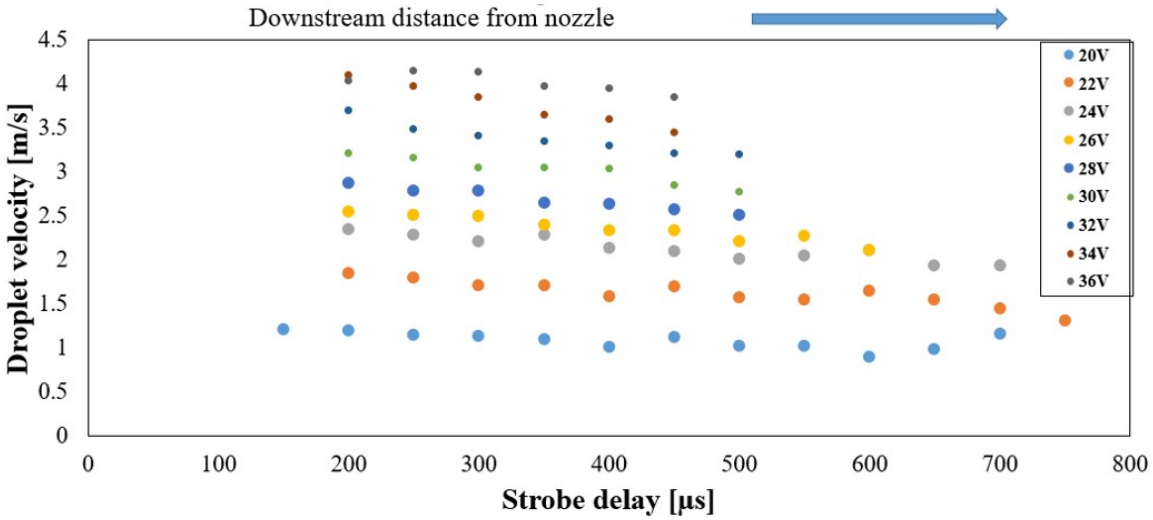

Figure 2.12. Effects of applied voltage on droplet velocity for water.

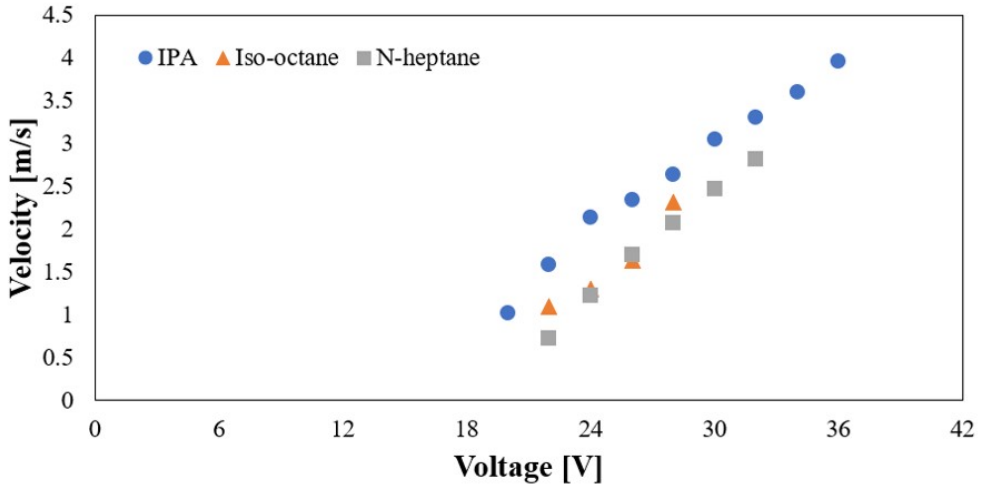

Figure 2.13. Effects of applied voltage on droplet velocity of 3 fuels at 400μs.

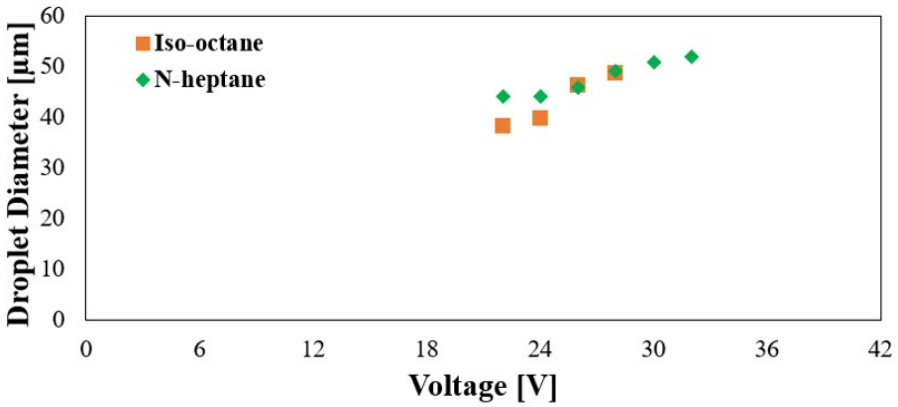

Figure 2.14. Effects of applied voltage on droplet size.

Figure 2.14 shows the droplet size changes for two fuels having different applied voltages. As applied voltages increase, the droplet mean diameter increases accordingly as a result of higher values of mass flow rate during jetting.

Figure 2.15 depicts the experimental results from Microfab [67], which shows the impact of dwell time on droplet velocity and droplet volume. Droplet velocity would increase initially as the increase of dwell time until reaching the maximum droplet velocity. Then the droplet velocity would decrease as dwell time increases. The relation between velocity and dwell time ideally should resemble the shape of a parabola with a local maximum value. A similar trend can be seen in relation to droplet volume as a function of dwell time. Figure 2.16 represents the relation between IPA droplet diameter and dwell time, which represents a similar trend as the correlations shown in Figure 2.15.

Therefore, the increase of applied voltage would increase both droplet velocity and diameter; the trends of increasing dwell time on droplet velocity and diameter follow a parabolic curve with local maximum velocity and diameter; there are no obvious impacts of jetting frequency and rise/fall time of the driving waveform on droplet velocity and diameter.

For the test cases presented in this chapter, droplet sizes have been measured within 30-45 μm in diameter, and the initial velocity leaving the nozzle is about 1 m/s. This range of combination of initial droplet size and velocity yielded stable, repeatable droplets, whose oscillation decay process could be captured by the camera with a sufficient number

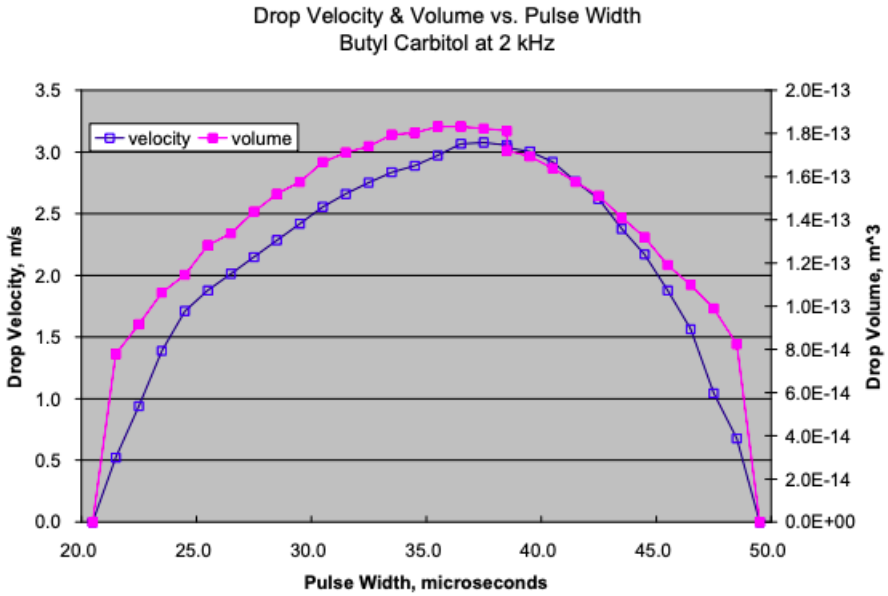

Figure 2.15. Effects of pulse width (dwell time) on droplet velocity [67].

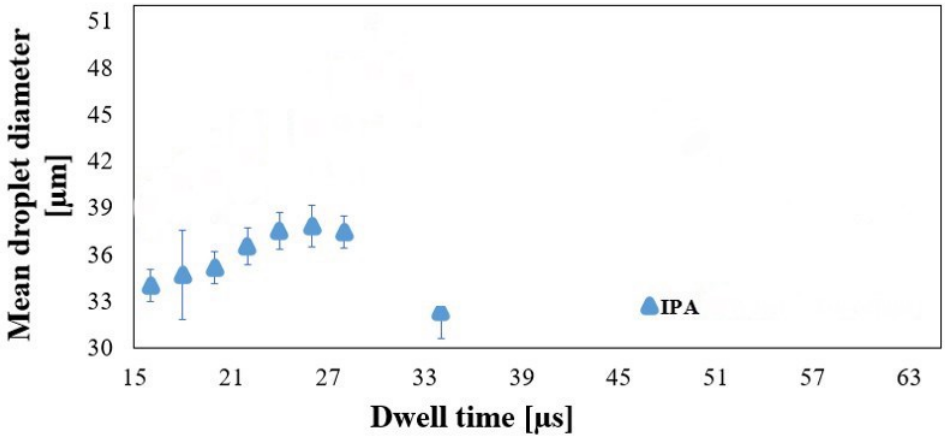

Figure 2.16. Effects of dwell time on droplet diameter.

of images to determine fuel physical properties.

2.2.3 Hardware Triggering for Signal Synchronization

In this section, two types of hardware triggering approaches for droplet generator, camera, and LED will be discussed. The first type of hardware triggering is used for droplet oscillation imaging in this work.

The first type of hardware triggering approach uses a National Instruments myRio unit, which sets the timing for camera and LED with respect to the jetting signal to synchronize the signals and acquire images from the camera. The timing diagram is shown in Figure 2.17. The generator signal refers to the voltage pulse supplied to the piezoelectric

device while the camera and LED signals refer to their respective trigger signals. While the signal generator produces the voltage waveform for the droplet generator, the camera and LED trigger signals are generated by the timing unit. A fixed time delay of 30 μs for all fuels separates the start of the camera trigger from the start of the LED trigger. This ensures that the camera sensor is fully operational and recording by the time the LED is triggered and thus overcomes the latency ($\approx$ 10 μs) of the camera. The LED duration is 4 μs for all cases. The camera trigger signal itself is separated from the generator pulse by a value which is incremented by a fixed amount (0.5 or 1 μs) per cycle. This provides the stroboscopic imaging required to generate a time series of droplet images for post-processing.

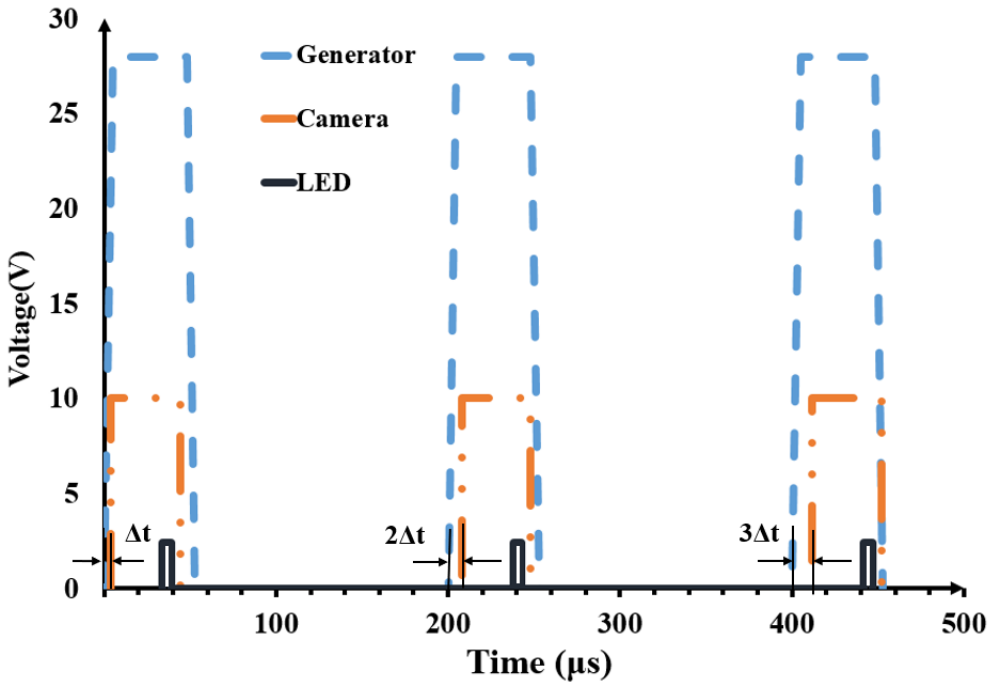

Figure 2.17. Timing diagram showing the generator waveform and hardware triggering.

The hardware triggered setup was developed due to the fact that initial tests showed the supplier provided imaging technique to be unsuitable for this work due to two reasons. One, the timing was software controlled and subject to latency issues. This resulted in the background lighting being inconsistent from one image to another. Two, with the stroboscopic technique, the minimum time separation between successive images was limited

to 1 μs. The current setup ensures a single LED flash for each image and the timing is tuned to ensure that only a single droplet is present in each image. The images obtained by hardware triggering have a consistent background improving the accuracy with which the droplet edge is detected.

Figure 2.18 shows the in-flight oscillation process for a 40 μm sized droplet of 2,5-dimethylfuran. The background intensity of the series of images is observed to be highly uniform. Further, the hardware triggered approach allows the time resolution to be less than 1 μs. This is required for measurements of fuels with higher viscosity (such as isobutanol), since the damping rate of the droplet oscillation is higher.

Table 2.1 shows information for the settings corresponding to the droplet generator, the camera, and the LED used in this work. A range of values used for the various fuels tested in this work is mentioned where appropriate.

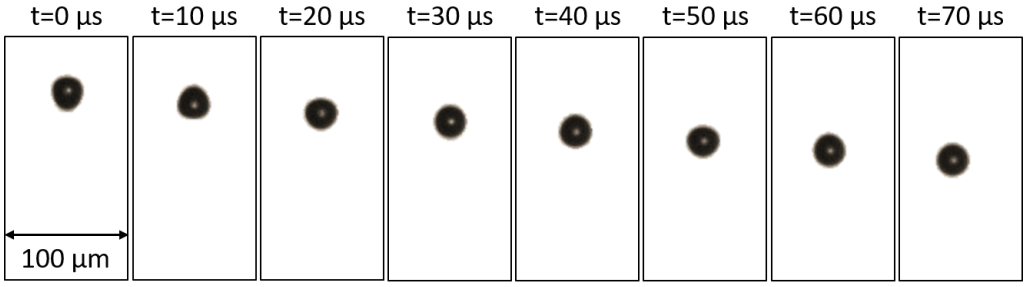

Figure 2.18. A sequence of images obtained using strobed imaging showing the oscillation of a 40 μm sized 2,5-dimethylfuran droplet.

Table 2.1. Jetting parameters set for the various test cases.

Voltage	**Dwell time**	**Rise/Fall time**	**Frequency**	**Back pressure**	**Strobe duration**	**Strobe delay**
26–40	31–48	5	300	-0.5– 0.1	4	0.5–1
V	μs	μs	Hz	in. of Hg	μs	μs

Previous lab colleague William Ard proposed another type of hardware triggering approach as shown in Figure 2.19, which is a little simpler than the first approach. In this approach, a signal generator (Siglent SDG1025) is used instead of the myRio. The LED is not triggered but is used as a constant light source. CH1 and CH2 are set to the same frequency with a pulse wave having 4V high voltage, and 0V low voltage. CH1 signal is sent

to JetDrive V which initiates the droplet generation, and CH2 signal is sent to the camera which synchronizes the camera action with respect to the droplet generation. Through the adjustment of the phase knob on the signal generator, different strobe delays can be set enabling the capture of droplet images at different times/locations. A continuous strobe sweep is used to track how the droplet falls from the nozzle exit plane to the bottom of the frame. The advantages of this method are its simplicity and low cost. It is much easier to build this setup compared with the first approach. But the frequency of jetting is constrained by the maximum frequency of the camera, which is 60 Hz. Since the current CCD camera cannot be hardware triggered if using frequencies higher than 60 Hz. Besides, the minimum pulse width from CH2 is 16.6 μs if the jetting frequency is 60 Hz, which is much larger than the first approach and cannot be used for droplet oscillation imaging. Since the imaging of droplet oscillation requires the pulse width for LED to be no more than 1 μs. Besides, the strobe delay is achieved by turning the phase shift knob step by step, which takes much more effort than the first approach where the myRio associated Labview program does the automatic strobe delay operation without human input.

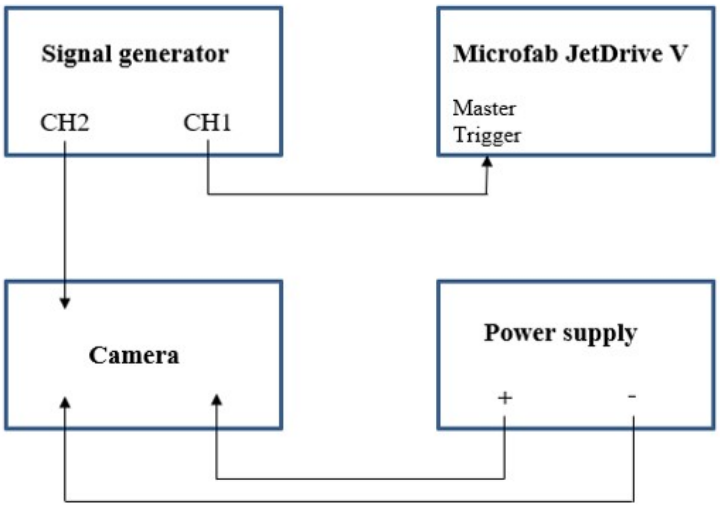

Figure 2.19. Second type of hardware triggering.

Therefore, the first type of hardware triggering approach with high resolution ($<$1 μs) is suitable for both droplet oscillation and evaporation process with full automation; the second type of hardware triggering approach can be applied to droplet evaporation scenario

due to longer time duration between two adjacent images.

2.2.4 Reference Measurements

The reference measurements conducted in this study utilized a tensiometer (Attension Theta by Biolin Scientific) and a viscometer (Cannon Fenske Routine Viscometer) to evaluate surface tension and viscosity of fuels at ambient temperature for comparison with literature data as well as results obtained using droplet oscillation dynamics. The minimum sample volumes required for surface tension and viscosity measurements are 15 mL and 7 mL respectively. The manufacturer supplied uncertainty for the surface tension measurement is 0.01 mN/m and for viscosity is 0.16% of the measured value.

2.2.5 Measurement Procedure

Prior to the measurement, the camera, generator, and strobe are aligned and the camera is focused on the nozzle tip. Next, the meniscus at the nozzle orifice is adjusted using the pressure controller to achieve equilibrium. Following this, a software program that controls the droplet generator is used to start the jetting process with the required process parameters. Jetting refers to the process where the liquid jet is repeatedly pinched off at the nozzle exit plane by the action of the piezoelectric device resulting in the formation of a continuous stream of droplets. Once stable droplet generation is observed on the live video mode of the camera, the hardware triggered image acquisition is activated. The timing device triggers the camera to take images that are transmitted over USB to a computer running an image recording program. The sequence of strobed images is saved as a video or MAT file on the computer. During image processing, individual frames are either extracted from a video file or converted from matrix form for further image processing using MATLAB. This will be elaborated further in the next section.

2.2.6 Image Processing

Once images are obtained, a sequence of post-processing steps are carried out in MATLAB to determine the droplet radius as a function of polar angle θ at different times. These steps are shown in Figure 2.20.

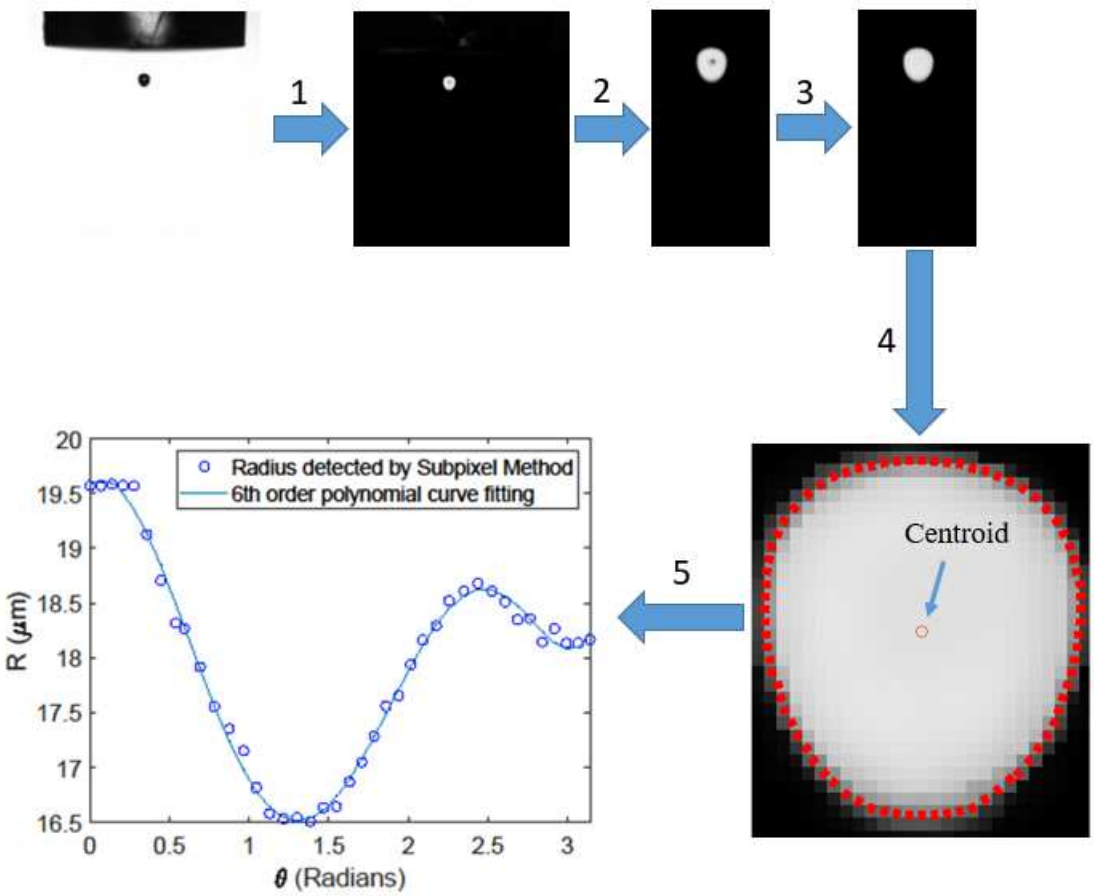

Figure 2.20. Image processing steps to obtain the droplet radius as a function of the polar angle.

Step 1 is background subtraction. After selecting an image without a droplet as the background, applying the image subtraction removes noise from the background.

Step 2 involves a batch cropping process so that the droplet is the only object retained in the series of images.

Step 3 uses anisotropic filtering [68]. While traditional Gaussian filters blur the edge while eliminating noise, the anisotropic diffusion method preserves the edges and thus provides greater contrast to aid in edge detection.

Step 4 includes edge detection by applying the Subpixel edge detection [69] algorithm to locate points on the droplet edge. There are a number of edge detection algorithms available, such as Canny, Sobel, Prewitt, and Roberts [70]. The Subpixel edge detection method is used in this work due to its ability to provide well-resolved edge details, such

as magnitude, orientation, position, and curvature with higher accuracy as compared to traditional gradient based approaches [69]. The Subpixel algorithm provides one edge point for each pixel located on the droplet edge in the image. For the droplet shown in Figure 2.20, 78 points are detected on the droplet edge. Figure 2.21 compares the edge detection results on curved edges of a droplet using both Subpixel and Prewitt algorithms. It is obvious to see Subpixel performs better in detecting edges with curved features. So it is a better option to select the Subpixel algorithm for droplet edge detection. Step 4 also involves the determination of the droplet centroid by averaging the x- and y-coordinates of the droplet edge points as determined by the Subpixel edge detection algorithm.

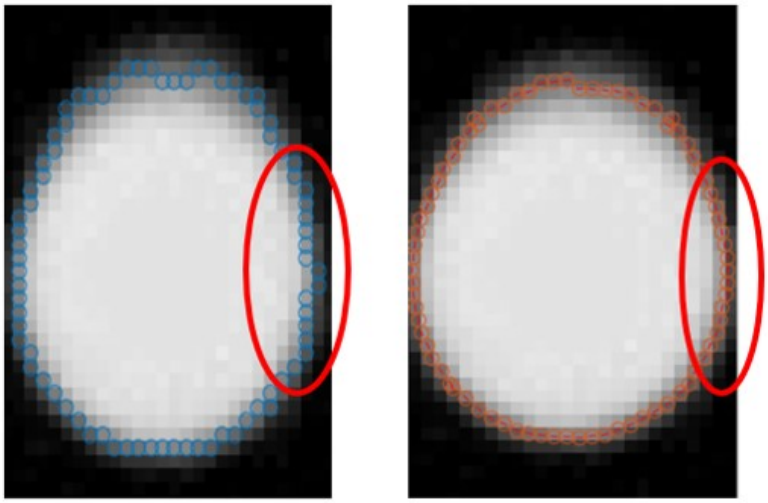

Figure 2.21. Subpixel (RHS) excels Prewitt (LHS) in the detection of the curved edges.

Step 5 involves the use of a 6^{th}-order polynomial fitting routine to fit the points detected by the Subpixel algorithm. This is found to be necessary in order to capture an accurate representation of the droplet shape particularly towards the end of the oscillation decay process. Figure 2.20 shows the droplet edge locations determined using the Subpixel algorithm and the polynomial curve fitting plotted as a function of the polar angle, θ. Only half of the droplet image is used to estimate the droplet radius as a function of θ, since vertical symmetry is assumed along the centerline of the droplet. Following this step, Eq. 2.1 is solved using a least-squares method to determine the mode amplitude coefficients including those for the zeroeth (R_0) and second (A_2) order modes. The modes, $n = 0$, and

$n = 1$ do not describe any oscillations following Eq. 2.2. The second-order mode (A_2) is used to calculate surface tension and viscosity. Figure 2.22 shows the ratio of A_n to R_0 plotted for modes 2, 3, and 4. The mode for $n = 2$ is clearly seen to have a much larger amplitude compared to the other modes.

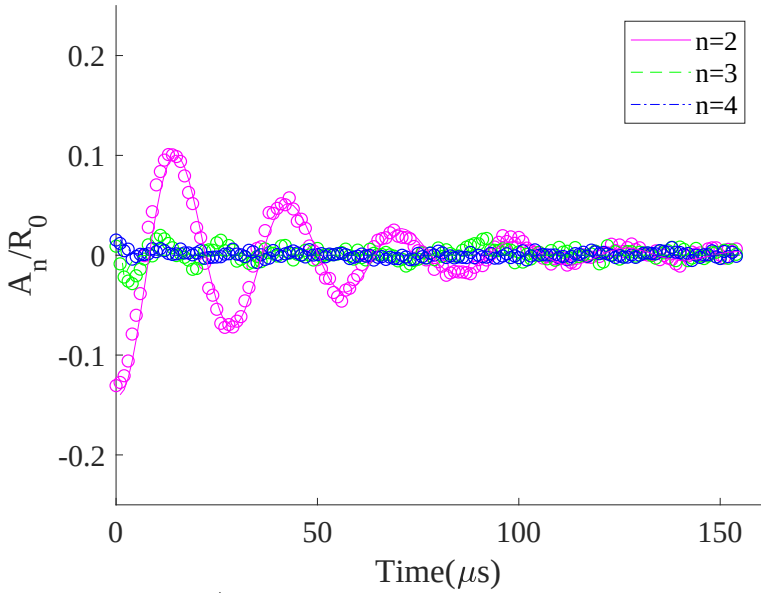

Figure 2.22. Ratio of A_n/R_0 for modes 2, 3, and 4 plotted as a function of time.

Figure 2.23 compares the droplet oscillation in both horizontal and vertical directions. The oscillation in the horizontal direction is much smaller than in the vertical direction. Therefore, mode 2 droplet oscillation in the vertical direction is studied in this work.

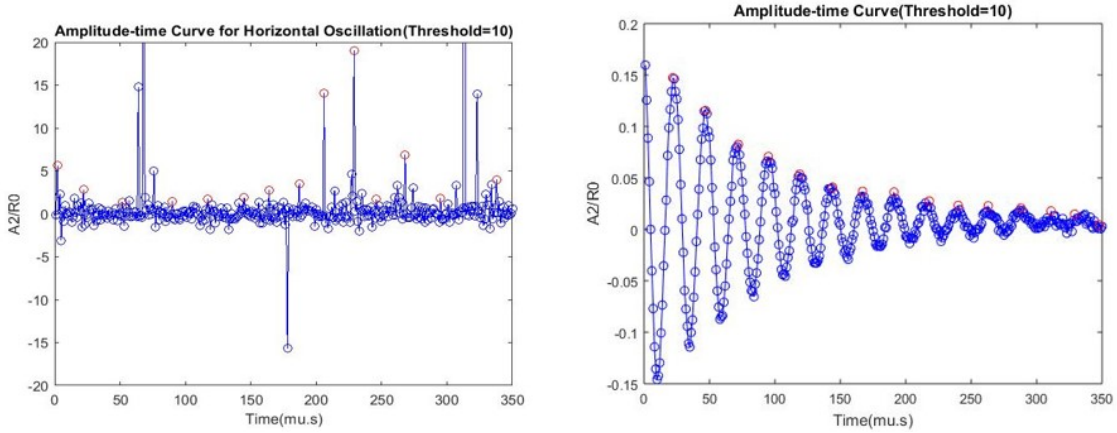

(a) Droplet oscillation in horizontal direction. (b) Droplet oscillation in vertical direction.

Figure 2.23. Droplet oscillation directions.

2.2.7 Fuels Tested

Six fuels of interest were tested in this work. This includes isooctane and n-heptane, which are primary reference fuels, whose blends are used extensively as surrogates to model gasoline combustion [71]. The remaining four fuels are bio-derived functional group fuel molecules deemed to be of interest as a drop-in replacement or blended component with gasoline for boosted SI engines [1]. Table 2.2 summarizes the six fuels tested in this work with reference to desirable properties as relates to use in advanced SI engines [4].

Table 2.2. Properties of fuels tested in this work as relevant for use in advanced SI engines.

Name	**Functional group**	**Formula**	**RON**	**MON**	**HOV**	**LHV**	**Density**	**Water solubility**
isooctane	Alkane	C_8H_{18}	100	100	306.9	44.3	691.9	2.44
n-heptane	Alkane	C_7H_{16}	0	0	364.9	44.9	683.8	3.4
Isobutanol	Alcohol	$C_4H_{10}O$	105	90	685.4	33.2	797.6	85000
Butylacetate	Ester	$C_6H_{12}O_2$	100.8	100	369.3	27.43	876	8400
2,5-dimethylfuran	Furan	C_6H_8O	101.3	88.1	332	32.9	895	1.47
Cyclopentanone	Ketone	C_5H_8O	101	89.4	504	31.99	944.1	60000
					kJ/kg	MJ/kg	g/L	mg/L

2.3 Results and Discussions

2.3.1 Repeatability of Oscillation Dynamics

The strobed imaging approach used in this work has the key advantage that it is not required to follow a single droplet through its oscillation dynamics using an expensive, high-speed camera.

However, an inherent assumption in this approach is that each successive droplet is generated in exactly the same manner and the oscillation dynamics that follow are exactly repeatable for the successive droplets. To gauge the validity of this assumption, tests were carried out where a large number of images were obtained at a fixed strobe delay time. Droplet edge contours detected from the images were overlaid and the x- and y-coordinates of the droplet centroid were compared. This was repeated for a few different strobe delay values. Figure 2.24 shows overlaid droplet edge contours for 20 μm-sized water droplets at a fixed strobe delay of 110 μs. 523 droplet edge contours are overlaid in Figure. 2.24. The

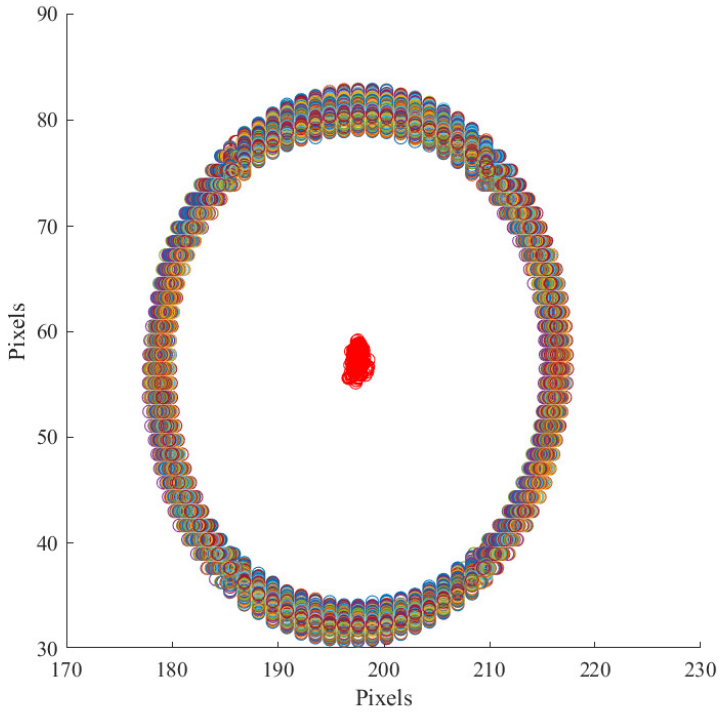

Figure 2.24. Overlaid image showing edge contours and centroid locations for 523 20-μm water droplets captured at the same strobe delay time.

standard deviation for the x-coordinate of the centroid location is 0.28 μm, while that for the y-coordinate location is 0.67 μm. This indicates a very high degree of repeatability is ensured for the purposes of using the strobed imaging approach.

2.3.2 Droplet Oscillation Decay Curves

Figure 2.25 shows plots illustrating the damping of droplet oscillations for each of the six fuels investigated in this work. The symbols in each plot show the ratio of the second-order mode amplitude coefficient (A_2) to the equilibrium radius (R_0) as a function of time. A_2 and R_0, respectively are obtained through a least-squares fitting of the droplet radius at each time instant (Figure 2.20) to the Legendre polynomial function following Eq. 2.1.

The range of values selected for the ratio, A_2/R_0, for each fuel is based on three main criteria. One, data points (or droplet images) right after the droplet separates from the liquid column in the nozzle of the piezoelectric device are discarded since the droplet still has a "tail" attached to it. This is illustrated in Figure. 2.26. Two, the oscillation theory is

applicable to an isolated liquid drop subjected to small-amplitude axisymmetric oscillation. Accordingly, any data points having A_2/R_0 values greater than 0.3 are discarded following previous work [72, 73]. In addition, data sets where the droplet motion does not follow a vertically downward path with symmetric oscillation about the vertical axis are discarded. Such non-ideal behavior is found to occur due to factors such as improper alignment of the meniscus, or accumulation of liquid fuel at the exit plane of the nozzle. Three, the minimum value of A_2/R_0 in each case is limited to a value of 0.01. The values smaller than 0.01 with minor variations are ignored.

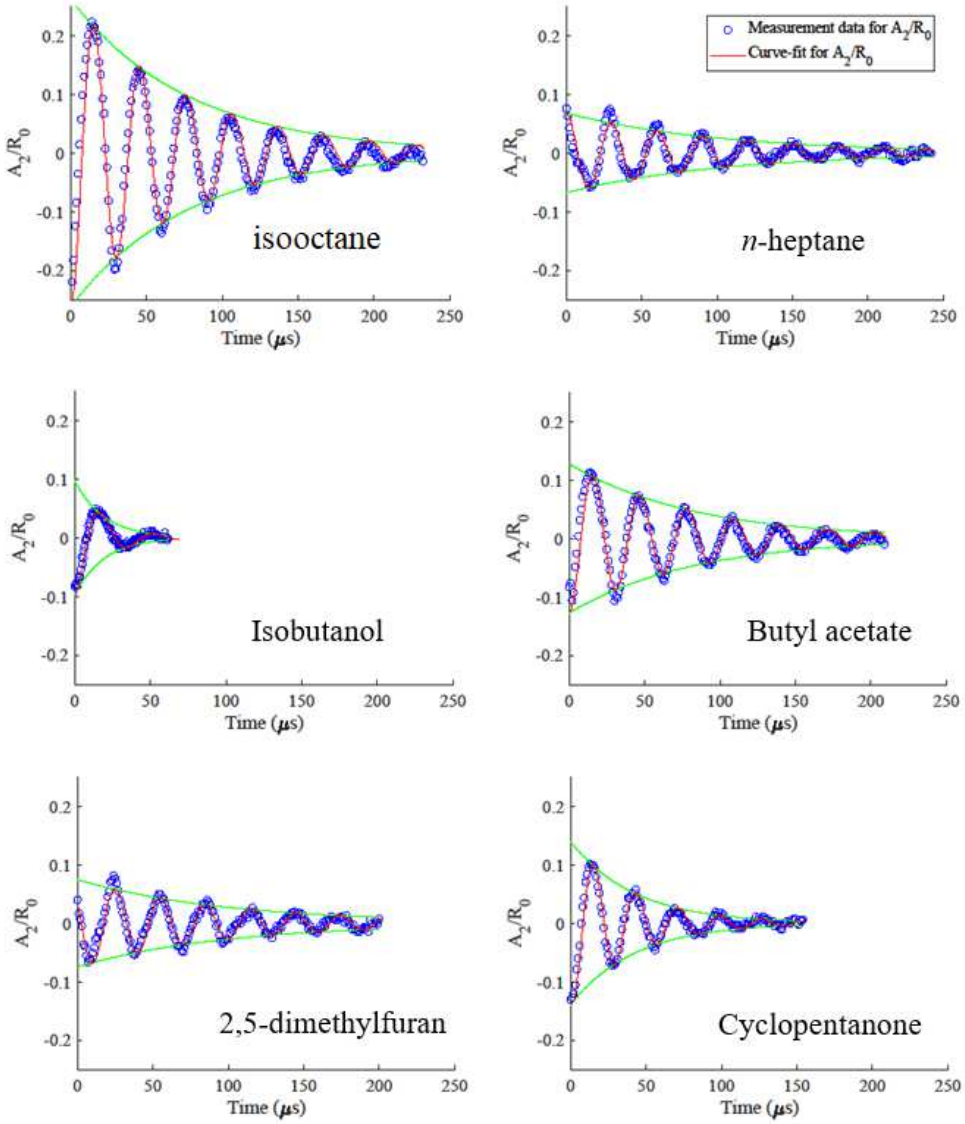

Figure 2.25. Representative droplet oscillation decay curves for each of the six fuels tested in this work.

In order to estimate the surface tension (σ) and viscosity (μ_l) using Equations 2.2 and 2.3 using the decay of the second order oscillation mode ($n = 2$), it is required to estimate the oscillation frequency of that mode (ω_2), and the corresponding decay time constant (τ). Figure 2.25 shows curve fits applied to the dataset in each plot following the form,

$$y(t) = C_1 e^{-C_2 t} cos(C_3 t + C_4) \tag{2.4}$$

where C_1, C_2, C_3, and C_4 are constants evaluated using a least-squares fitting to the data points in each plot. The curve fits obtained for each data set are overlaid on the data points in each of the plots presented in Figure 2.25. Once the constants in Eq. 2.4 are evaluated for each data set, surface tension and viscosity can be calculated using Eq. 2.2 and 2.3 given that, $C_3 = \omega_2$, and $C_2 = 1/\tau$. The oscillation frequency (ω_2) can also be calculated using a Fourier transform of the dataset and both approaches yield very similar results. It is to be noted that the value of R_0 in Equations 2.2 and 2.3 are obtained using an average value for each data set. The standard deviation in R_0 for each data set is of the order of 0.1 μm.

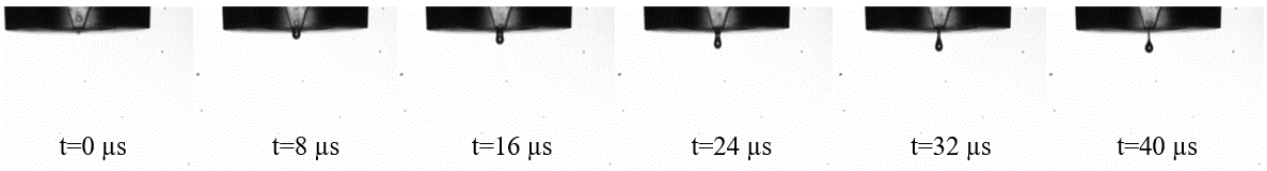

Figure 2.26. Initial sequence of butyl acetate droplet formation at the nozzle exit.

The damping curves for the various fuels shown in Figure 2.25 provide direct insight into their physical properties of interest in this work. The decay time constant is inversely related to viscosity (Eq. 2.3) and accordingly, fuels with higher viscosities such as Cyclopentanone (μ=1.17 cP, τ=50 μs) and Isobutanol (μ=3.60 cP, τ=20 μs) show rapid decay in the oscillation amplitude due to viscous damping. Fuels with higher surface tension such as Cyclopentanone ($\sigma_l = 33.2\ mN/m$) and 2,5-dimethylfuran ($\sigma_l = 26.5\ mN/m$) have higher oscillation frequencies, 35.7 kHz and 33.4 kHz, respectively over, isooctane ($\sigma_l = 18.6\ mN/m$) which has a frequency of 32.9 kHz, following Eq. 2.2.

2.3.3 Surface Tension and Viscosity Measurements

Table 2.3 summarizes the results for surface tension and viscosity obtained for the six fuels tested in this work. Measurements obtained in this work using droplet oscillation dynamics and standard instruments (tensiometer and viscometer) are compared with literature data from various sources [63, 64, 74, 75, 76, 77, 78, 79, 80]. The measured values reported for each fuel using droplet oscillation are averaged values calculated from 4—7 data sets. The measurements reported from the standard instruments are averages calculated from 3 data sets.

Table 2.3. Surface tension and viscosity measurement results.

	Surface tension (mN/m)			**Viscosity (mPa.s or cP)**		
	Literature	Tensiometer	Droplet oscillation	Literature	Viscometer	Droplet oscillation
isooctane	18.60 [63]	19.26±0.3	19.60±0.43	0.52 [64]	0.50±0.1	0.54±0.01
***n*-heptane**	20.02 [74, 63]	20.14±0.15	21.59±0.23	0.40 [74, 75]	0.40±0.01	0.44±0.02
Isobutanol	22.81 [63, 76]	22.83±0.01	22.35±1.14	3.44 [76]	3.66±0.10	3.02±0.21
Butylacetate	25.16 [74, 63]	24.94±0.05	26.26±0.68	0.73 [74]	0.69±0.01	0.76±0.04
2,5-dimethylfuran	26.50 [63, 77]	26.17±0.33	26.17±0.77	0.53 [78]	0.49±0.03	0.53±0.06
Cyclopentanone	33.21 [74, 63]	33.65±0.07	31.57±0.25	1.11 [79, 80]	1.11±0.05	1.32±0.05

Table 2.3 also reports the uncertainties in the measurement results using the reference instruments as well as droplet oscillation. The uncertainty values [59, 81] are computed for a 95% confidence interval based on a Student's t-distribution which is more appropriate for the sample sizes used in this work. The formula for uncertainty calculation using Student's t-distribution is written in Eq. 2.5.

$$U = TS/\sqrt{n} \tag{2.5}$$

where U is the uncertainty, S is the standard deviation, n is the number of samples, and T value can be found in Column "P = 0.025", Table A.2, Appendix A, in the Statistical Methods textbook [82]. T values are 4.3027, 3.1824, 2.7764, 2.5706, 2.4469, 2.3646 when

the sample size ranges from 3 to 8. For example, the calculation of the uncertainty of 2,5-dimethylfuran surface tension requires the inputs of the standard deviation S=0.7366 mN/m, the number of sample n is 6, T=2.5706 has found from Table A.2 from the block corresponding to n-1=5 and P=0.025. Then, substituting S, T, n values into Eq. 2.5 gives the uncertainty of surface tension U=0.7730 mN/m.

The primary sources of uncertainties comprise the resolution of the camera, uncertainty in droplet diameter measurement using the edge detection algorithm, the curve fitting functions applied to droplet radius versus polar angle, the selections of first and last images in each data series, and the residual of the least-square function fitted to the damping curve. Since these uncertainties cannot be easily described in the form of functions. So, error propagation has not been used for uncertainty analysis. Instead, Student's t-distribution has been used in this work for uncertainty calculation based on a 95% confidence interval.

The measurements obtained using the reference instruments show a maximum deviation of 4% for surface tension and 8% for viscosity from literature data. The measurements obtained using the droplet oscillation approach show a maximum deviation of 7% for surface tension and 13% for viscosity. The highest deviations in the measurements obtained using droplet oscillation are seen for the fuels with the highest viscosity for which the oscillations decay rapidly. Figure 2.27 shows the measurement results and literature data compared for the various fuels on the same plot to highlight the range of variation of physical properties measured using the oscillation technique. Fuel surface tension values range from 19–33 mN/m, while viscosity ranges from 0.4–3.5 cP. The uncertainties associated with literature and measurement data are added as error bars in Figure 2.27.

On average, about 5 μl of each candidate fuel is required for analysis. This includes the quantity of fuel required during the initialization of the experimental setup, when some fuel is used for purging the nozzle. The average data collection time for each fuel is about 20 s.

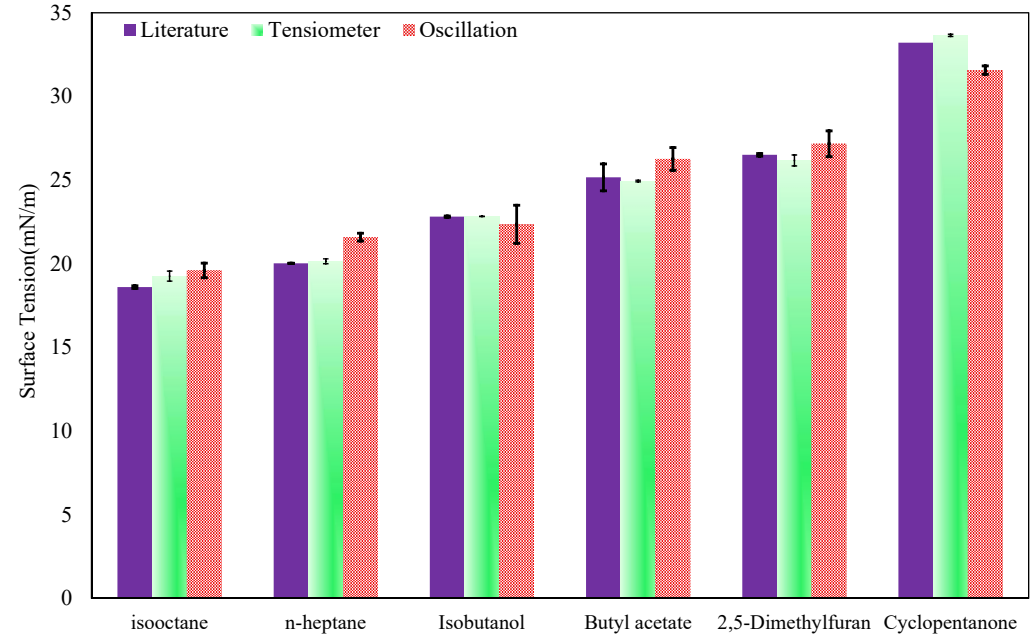

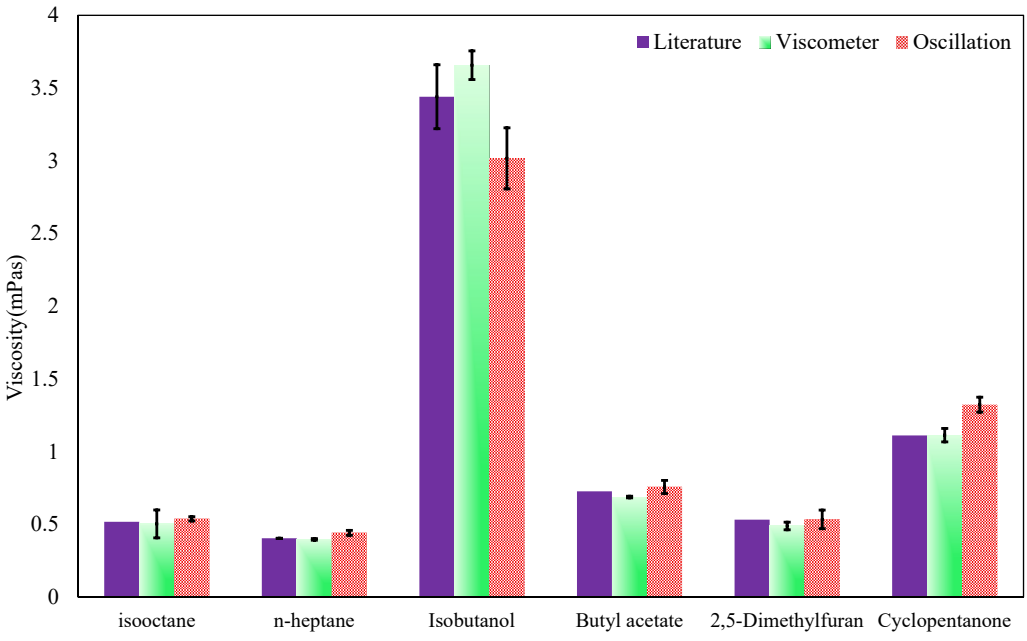

Figure 2.27. Comparison of measured and literature data for viscosity and surface tension.

Chapter 3
Droplet-based Surface Tension and Viscosity Measurement at Elevated Temperatures

Chapter 1 describes the tiered fuel-screening process developed by DOE researchers, where down selection of candidate fuels with acceptable values of surface tension and viscosity is one of the important steps. In this work, the droplet-based fuel property measurement approach for surface tension and viscosity is extended to include cases at elevated temperature conditions.

This chapter is organized as follows. The experimental approach is described following the droplet oscillation theory for elevated temperatures conditions. Then, details of numerical simulation used to study the heated droplet oscillation processes are provided. Finally, results from experiments and simulations are presented and compared.

3.1 Theory

Figure 3.1 shows a series of droplet images for isobutanol at 55°C representing the process from droplet formation/pinch-off to droplet motion. Table 3.1 shows a sequence of images for isobutanol at two temperatures of 30°C and 55°C, illustrating the decay of the droplet oscillation. An initially perturbed droplet in motion undergoes oscillations, that eventually gets damped out. Isobutanol droplet at 55°C needs longer time to reach equilibrium status compared with the case at 30°C due to temperature effects.

Figure 3.1. Droplet injection sequence of isobutanol at 55°C. Images spaced 25 μs apart.

Eq. 2.2 and 2.3 are used for surface tension and viscosity calculation at both ambient and elevated temperature conditions. For a heated droplet, it is useful to find how temperature affects the oscillation process through surface tension and viscosity. Considering a 40 μm diameter isobutanol droplet with second mode oscillation, $\sigma_l \propto T^{-1.3}$, $\rho_l \propto T^{-0.4}$, $\rho_a \propto$

This chapter was previously published as Dang, W., Gurunadhan, M., Schoegl, I., & Menon, S. (2021). Temperature effects on droplet oscillation decay with application to fuel property measurement. Atomization and Sprays, 31(10). Reprinted with permission from Begell House, Inc.

Table 3.1. Droplet oscillation decay processes for isobutanol at two different temperatures.

	0 μs	10 μs	20 μs	30 μs	40 μs	50 μs	60 μs
55°C							
30°C							

T^{-1}, and $\mu_l \propto T^{-8.6}$, using air as the ambient gas. Based on Eq. 2.2 and 2.3, the following correlations can be derived, $f_n \propto T^{-0.5}$, and $\tau \propto T^{8.2}$. Therefore, the oscillation frequency f_n should scale as $T^{-0.5}$, while the decay time constant τ should scale as $T^{8.2}$. According to the above scaling analysis, as temperature increases, surface tension decreases and the oscillation frequency reduces due to a smaller restoring force to return the droplet to its equilibrium status. Similarly, viscosity decreases as temperature increases, which leads to longer decay time due to the reduced ability for the fluid to dampen out the oscillation.

In this work, both experimental and numerical methods have been used to study the droplet shape oscillation process. Through the observation of droplet shape oscillation, the surface tension and viscosity of the transportation related fuels can be measured. Lamb's theory used in this work is only applicable to cases with small-amplitude oscillation. Typically, small-amplitude oscillation assumption is valid when the value of A_2/R_0 is less than 0.1, and the Ohnesorge number ($Oh = \mu_l/(\sqrt{\rho_l R_0 \sigma_l})$) is also less than 0.1 [41, 72, 83]. For fuels with higher viscosity, Lamb's linear theory is not suitable due to the higher Ohnesorge number. The sizes of the droplets in experiments are small, about 30–45 μm in diameter to guarantee 2 μl/min flow rate and satisfy the research objective of using small sample sizes to get physical properties measurement. However, the small droplet size also contributes to a higher Oh number.

Further, when a heated fuel droplet is injected into ambient air, there is relative motion between the droplet and ambient air, causing convective heat transfer leading to droplet

temperature change and transient changes in fuel properties. In addition, mass transfer introduces droplet mass loss through evaporation, which reduces the size of the droplet. Although it is challenging to study these non-ideal effects in experiments directly, numerical simulations are able to show the related physics by studying each individual parameter at a time.

3.2 Experiment

The experiment setup, measurement procedure, imaging processing, and fuels tested are now described. Together they are used to study the transient oscillation process of heated fuel droplets, using which, fuel physical property changes with temperature are evaluated.

3.2.1 Experimental Setup

Figure 3.2 shows the components that constitute the experimental setup in this work. The major differences between this setup and the setup in Chapter 2 reside in two components: piezoelectric droplet generator with heating elements and PID controller. The piezoelectric droplet generator (MicroFab PH-41) equipped with a heating element is used to generate a continuous trail of droplets. The heating element, having a power rating of 200W at 120V, is attached to an aluminum body with a polypropylene reservoir containing the fuel to be dispensed. A K-type thermocouple assembled inside the aluminum body of the reservoir provides real time temperature reading to a PID (Proportional-Integral-Derivative) controller. On receiving the temperature reading from the K-type thermocouple, the PID controller (Extech 48VFL) controls the corresponding power output so that the fuel in the reservoir can be heated to the desired temperature within 1 minute. Figure 3.3 depicts the wiring diagram for the PID controller with a solid state relay and heating elements. Considering the limitation of the material of the reservoir, the maximum temperature that the fuel can be heated to is about 70°C. All other components are the same as the setup in Chapter 2.

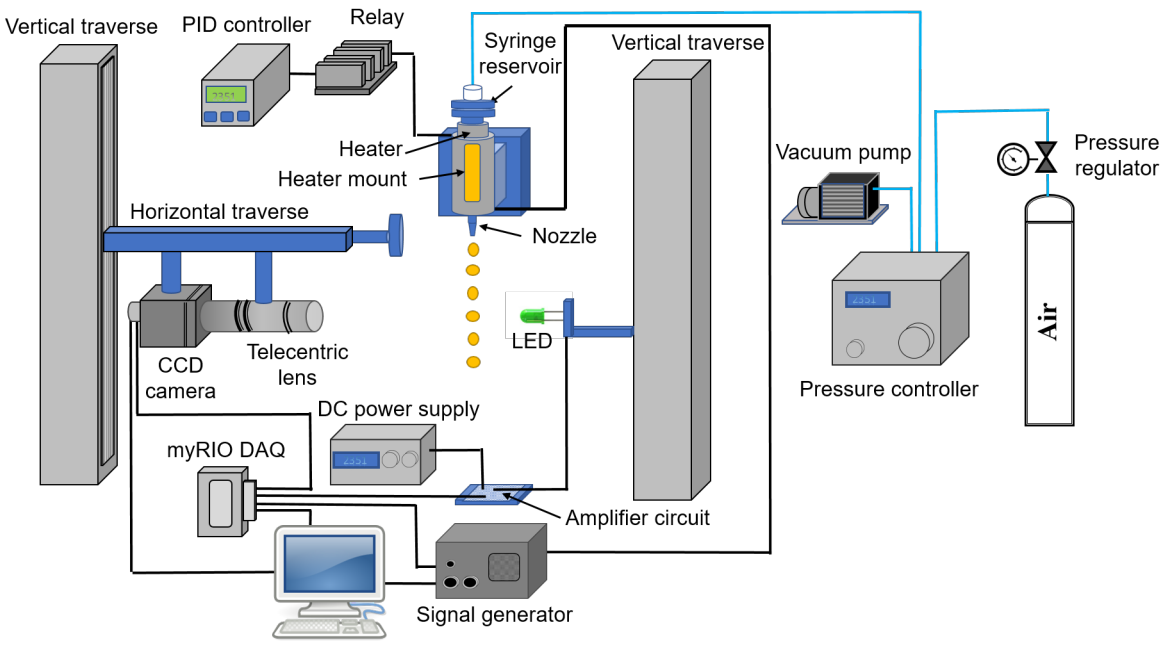

Figure 3.2. Experimental setup.

3.2.2 Measurement Procedure

The measurement procedure follows the following major steps. First, the camera and LED are aligned and focused on the nozzle exit plane, and the fuel samples in the reservoir are heated to the desired temperature before the measurement. Second, both the back pressure and operating parameters (applied voltage, dwell time, rise/fall time, and jetting frequency) are adjusted through pressure controller (MicroFab CT-PT-21) and JetServer 4 software until a stable meniscus is formed at the exit plane of the nozzle. Third, on clicking the jetting button in the JetServer 4 software, a continuous droplet trail is issued, while hardware triggering is initiated at the same time. Real time droplet images are captured by the CCD camera using the stroboscopic imaging technique.

When the fuel sample was heated in a polypropylene reservoir, the material of the reservoir became soft when the temperature measured was higher than 60°C. During heating, nozzle clogging happened frequently, which may be the result of heating the reservoir to a higher temperature or chemical incompatibility between polypropylene and fuels. According to a "Chemical compatibility guide" [84], polypropylene has poor compatibility with

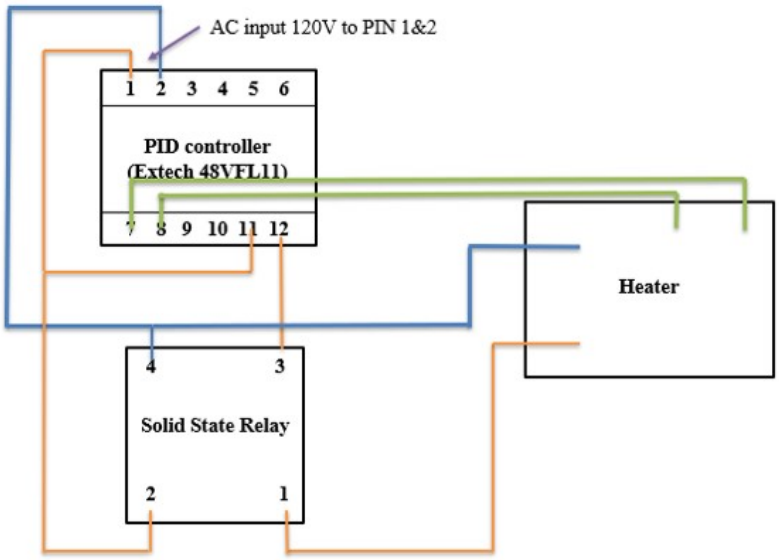

Figure 3.3. PID controller wiring diagram for fuel heating control.

at 50°C. So the operation of removing nozzle clog with heated fuel setup is indispensable for continuous and stable droplet generation. Methods to unclog the nozzle include back-flushing the debris using a high vacuum, as well as using an ultrasonic sonicator to loosen the debris.

3.2.3 Image Processing

Image processing was carried out using routines written with Matlab codes. The process is the same as the process in Chapter 2, which includes background subtraction, batch cropping, anisotropic filtering, edge detection by a Subpixel method, and use of a 6^{th} order polynomial for accurately capturing the droplet shape. A detailed description of these steps can be found in previous work [85].

3.2.4 Fuels Tested

As the issues of climate change and transportation fuel related emissions persist, there is an increasing need to provide renewable fuels to the automotive and aerospace industries. Corn-derived ethanol is widely used by blending with gasoline in various ratios in the United States [86]. As one of the most popular bioblendstocks, isobutanol can be obtained from the biomass production process and has successfully mixed with gasoline and diesel fuels for engine use. Popuri and Bata's work [87] explains the addition of isobutanol to

gasoline resulted in more power, higher thermal efficiency, and lower BSFC (brake specific fuel consumption) than adding methanol and ethanol to gasoline. Isobutanol blended with diesel has also been analyzed for HC, NOx, and CO emissions[88]. Given isobutanol has higher energy content, lower Reid vapor pressure, and reduced emissions, it has become a fuel of choice as a blending component with gasoline in many biofuel research centers [89]. Therefore, isobutanol(Alfa Aesar, 99%) becomes one of two candidates fuels tested in this work given its significance as a bioblendstock.

The other fuel tested in this work is PRF 84, where PRF stands for Primary Reference Fuel and 84 corresponds to a blend of 84% isooctane (Acros Organics, 99.5%) with 16% *n*-heptane (Acros Organics, 99.5%) by volume. PRF 84 is a popular and simple two-component surrogate for gasoline fuels [90]. PRF 84 has been extensively employed by the engine research community to study various aspects of SI engine combustion including ignition delay [90], flame speed [91], autoignition [92], chemical kinetics, and exhaust composition [93].

The two fuels selected reflect the application space, where this proposed rapid screening approach is of relevance, which is to provide temperature sensitivity to properties for bioblendstocks and their blends with conventional fuels. Table 3.2 shows settings for droplet jetting as employed in the tests. Given the high viscosity of isobutanol, it was important to choose closely spaced images to capture the details of the damping process with very high resolution. Accordingly, the time separation between two adjacent images as set by the strobe delay is 0.5 μs for isobutanol, while for PRF 84 cases the time separation was set as 1 μs due to its lower viscosity. The frequency of droplet generation was set to 300Hz for all cases.

Table 3.2. Jetting parameters set for the various test cases.

Fuel	**Temperature[°C]**	**Voltage[V]**	**Dwell Time[μs]**	**Rise/Fall time[μs]**	**Frequency[Hz]**
Isobutanol	30-55	21-34	31-32	5	300
PRF 84	30-55	26-27	30-35	5-7	300

3.3 Simulation

Numerical simulation is a helpful tool that provides the analysis of the effects of heat transfer and evaporation on the process of droplet oscillation and predictions of surface tension and viscosity. Simulation allows variation of one parameter at one time while keeping other parameters unchanged. This is difficult to achieve in experimental work. It is not easy to keep parameters such as droplet size, velocity, back pressure, and operating parameters (applied voltage, frequency, dwell time, and rise/fall time) unchanged during an experiment. For example, increasing temperature may change the settings of operating parameters to obtain stable droplet generation, so the droplet size may not be the same in each data set.

Therefore, numerical simulation serves as an essential supplement to the experiments in this work. The following subsections will discuss the setup, initial conditions, mesh, and boundary conditions accordingly.

3.3.1 Setup

Given the consistent changing interface between droplet and ambient air due to droplet oscillation, the selection of an interface tracking algorithm is of great importance. This algorithm should accurately track the interface with minor spatial and temporal diffusion. Eulerian and Lagrangian methods are the most common methods for interface tracking. Lagrangian method can clearly define, and track the interface in time [94]. But in current work, the needs to do remeshing and reconstruction are inevitable, which is a result of large interface deformation. This makes Lagrangian method not a good option for this work. Instead, Eulerian method is selected in this work. Especially, the Volume of Fluid (VOF) algorithm [95] was chosen in the simulation for its effectiveness and accuracy in capturing interface changes in multiphase flow fields [94].

$$\frac{\partial(\alpha_p \rho_p)}{\partial t} + \nabla \cdot (\alpha_p \rho_p u) = 0 \tag{3.1}$$

As Eq. 3.1 shows, the volume fraction of individual phases (α_p) is advected through the velocity field of the liquid-gas mixture using VOF method. The interface location is reconstructed in each time step. The pressure-implicit scheme with PISO method [96] is selected for pressure-velocity coupling. The number of PISO cycles (N_p) was set as 2 for all the simulation cases. The volume fraction continuity equation is discretized in time and the interface reconstruction was carried out by Piecewise Linear Interface Calculation (PLIC) scheme [97].

According to previous work [98] and [99], droplet evaporation models using VOF have successfully captured the phenomena of droplet evaporation. Both the equations of interfacial mass and energy balance are solved and the rate of vaporization is imposed as a volumetric mass source (vapor) and mass sink (liquid), in their respective mass conservation equations. Being the volumetric source term in the energy equation, the continuously updated values of heat loss due to vaporization are required. Also, a UDF (User-defined Function) was used to evaluate the vaporization rates and mass source term. Parallel computation is selected instead of serial computation in this work. The effects of conduction within the droplet, convective heat transfer concerning droplet and ambient air, and heat loss as a result of droplet vaporization are modeled in the simulation.

Table 3.3 summarizes the details of the numerical models and discretization information. ANSYS Fluent Version 18.2 was used to solve the equations for mass, momentum, energy, and species conservation. The total simulation time was set the same as the droplet oscillation decay time. The convergence criteria for each governing equation at each step are as follows. 10^{-5} was set for the momentum and continuity equations, 10^{-6} was set for the energy and the VOF equation. The simulation was taken using LSU High Performance Computing (HPC) facility with $\sim$80 cores/case.

3.3.2 Mesh and Boundary Conditions

Figure 3.4 shows a 2D domain, which represents a rectangular shape computational domain. The boundary conditions have marked in the figure. The left, right, and top edges

Table 3.3. Numerical models and discretization.

Numerical aspect	**Solution method**
PV coupling	PISO
Gradient	Green Gauss Node based
Pressure	PRESTO!
Momentum, Species, Energy (convective)	Second order upwind
Multiphase	VOF (Explicit Geo Reconstruct -PLIC)

of the domain are prescribed as pressure outlet boundary conditions. The bottom line is also the axis of the droplet and the 2D domain.

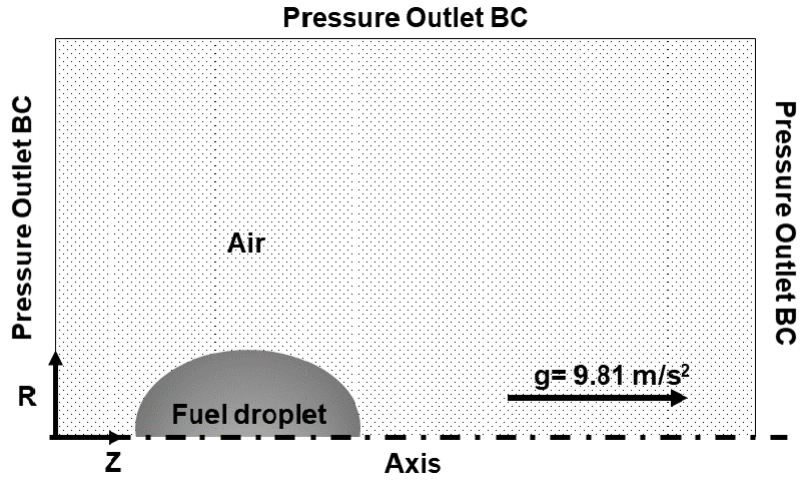

Figure 3.4. Representative computational domain along with imposed boundary conditions.

The simulation cases used a similar scale of magnitude for droplet velocity (∼1m/s) and diameter (∼32—40 μm diameter) as experiments. Because of this similarity, a grid convergence study is conducted using a typical droplet oscillation case with 32 μm diameter isobutanol droplet having 20% deformation as an initial condition. The maximum reduction in droplet diameter in the vertical direction was defined as the deformation. During droplet oscillation, the shape of the droplet goes through prolate–oblate cycle back and forth until it reaches equilibrium condition with an almost circular shape. Figure 3.5 shows the oscillation decay for three mesh densities. Mesh density (Δ_R) defines the number of mesh points along the radius of the droplet in the vertical direction. With different mesh density values, the variation in droplet oscillation frequency and damping time constant

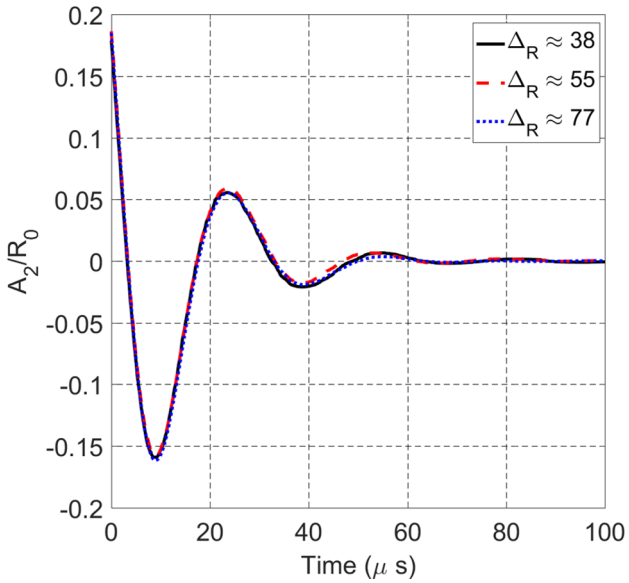

Figure 3.5. Mesh convergence study results showing oscillation decay for three different mesh densities.

was less than 1%. From the results of the convergence study, a mesh density of 60 was selected and applied to all the simulation cases in the current work. For isobutanol cases, ∼0.3 million mesh points were needed. While for PRF 84 cases, ∼0.8 million mesh points were required due to longer oscillation decay time.

3.3.3 Initial Conditions and Thermophysical Properties

A deformed fuel droplet, at four different initial temperatures of 30, 40, 50, and 55 °C, is injected into the ambient air with temperature initialized as 22 °C. The droplet diameter is assumed to be constant as 40 μm in all numerical simulation cases. The initial droplet velocity or the injection velocity is set to be 1 m/s for all the cases. Only the vertical velocity in the direction of gravity is considered in this work. And the gravitational acceleration is 9.8 m/s^2 along the positive Z direction. An initial deformation of 20% (relative to droplet radius) was applied as an initial condition for all cases.

The phases in the simulation include the primary phase (air) and the secondary phase (fuel). The deformed droplet with a constant initial velocity, diameter, and deformation at a specific temperature, is placed into a 2D axisymmetric domain with the axis of droplet movement path aligned with the bottom edge of the domain. Numerical simulations were

conducted with isobutanol and PRF 84. The temperature dependent physical properties of the liquid fuels were expressed as functions of temperature. The reference values of these properties at different temperatures can be found in various literature sources [63, 100, 101]. Some key physical properties used in the simulation are summarized in Appendix A, which are applicable in the temperature range from 273 to 340 K. The mass diffusion coefficient between two liquid components of PRF 84 was assumed to be $1.2 \times 10^{-9}\,\mathrm{m}^2/\mathrm{s}$. The physical properties for the gaseous phase such as air and fuel vapor for isobutanol and PRF 84 are from empirical correlations [102], and reference data is provided by Cantera [103] whose functional forms are shown in Appendix A.

3.4 Results and Discussions

3.4.1 Droplet Oscillation Decay

After the initial perturbation issued by the piezoelectric droplet generator, fuel droplets are formed and undergo oscillation processes while moving through the air with an initial velocity. The stroboscopic imaging technique is used to capture the droplet oscillation process. The time duration between two adjacent droplet images for isobutanol is set as 0.5 μs, and for PRF 84 is 1 μs. Figure 3.6 includes the values of A_2/R_0 as a function of time in eight plots for two fuels at four different temperatures ranging from 30 to 55°C. Each plot shows three data series, which involve raw experimental data for A_2/R_0, curve-fit data for A_2/R_0, and a damping decay curve-fit. The function that was used to illustrate the values of A_2/R_0 as a function of time is as follows.

$$y(t) = C_1 e^{-t/\tau} \cos(2\pi f_2 t + C_2) + C_3 \tag{3.2}$$

where C_1, C_2, and C_3 are constants evaluated using the least squares curve-fits algorithm. A consistent set of criteria are applied in selecting the data series representing the values of A_2/R_0 as a function of time as plotted in Figure 3.6. The small-amplitude oscillation based on Lamb's theory is guaranteed by constraining the maximum value of A_2/R_0 as

0.25 [41]. Given the resolution constraints of the current imaging system, the negligibly small oscillation at the end of the damping period is discarded. The threshold value for the minimum A_2/R_0 is set to be 10% of the initial deformation so that there is a 90% reduction in oscillation amplitude. The oscillation frequency (f_2) and decay time constant (τ) can be calculated from the damping curves. Table 3.4 summarizes the oscillation frequency, decay time constant, Oh number, and droplet radius from experimental results with respect to each case plotted in Figure 3.6.

The impacts of temperature on the droplet oscillation decay process for isobutanol can be seen in Figure 3.6. As temperature increases, more time is required for the oscillation to decay, which agrees well with the results from scaling analysis in Section 3.1. Since the fuel viscosity decreases due to temperature increase, the decay time constant should increase. Similarly, PRF 84 needs a longer time for oscillation decay than isobutanol at the same temperature. This is because PRF 84 has a lower viscosity than isobutanol at the same temperature.

From the scaling analysis, the frequency should decrease as the increase of temperature. On the contrary, the oscillation frequency of isobutanol from experiments shown in Figure 3.6 increases with an increase in temperature. The opposing trends of oscillation frequency from experiment and scaling analysis arise due to the non-constant droplet radius in different data sets in the experiment. This is a limitation of the experiment. It is difficult to control droplet size and temperature independently for data sets with different temperatures. As temperature changes, the required back pressure to reach force balance at the meniscus to keep stable droplet generation changes. Subsequently, the operating parameters set in JetServer 4 software change if the temperature changes. The difficulty in controlling droplet radius results in the coupled effects on changes to the oscillation behavior. Simulation approaches can be used to remove these coupling effects by considering droplet radius for all cases to be constant.

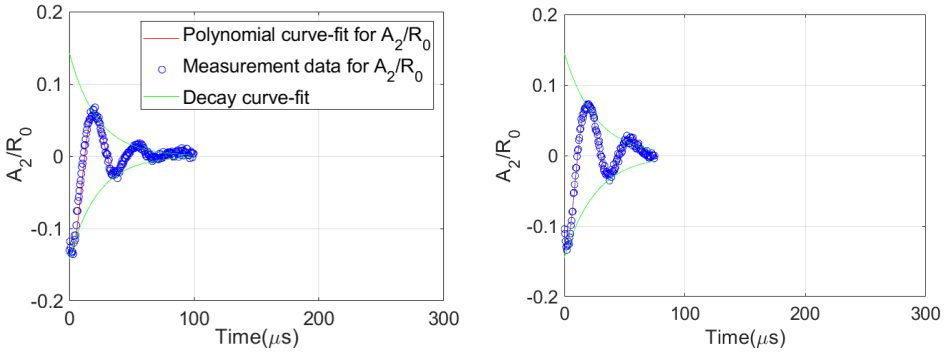

(a) Isobutanol at 30°C

(b) Isobutanol at 40°C

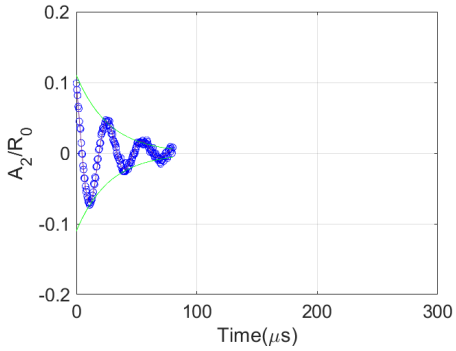

(c) Isobutanol at 50°C

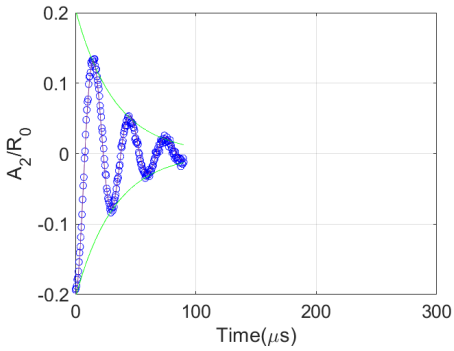

(d) Isobutanol at 55°C

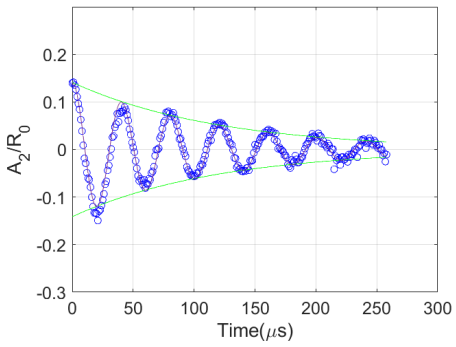

(e) PRF 84 at 30°C

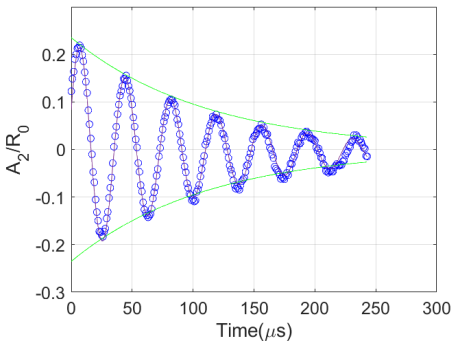

(f) PRF 84 at 40°C

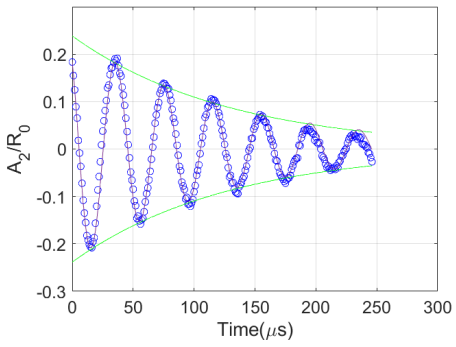

(g) PRF 84 at 50°C

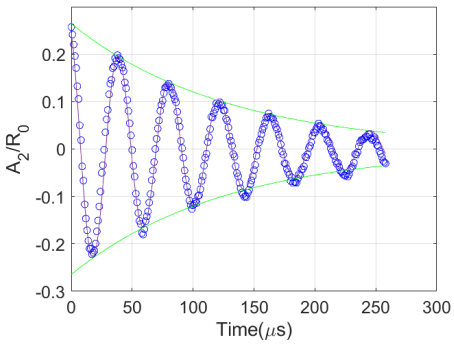

(h) PRF 84 at 55°C

Figure 3.6. Droplet oscillation decay curves for fuels tested in this work at various temperatures — Experimental results.

Table 3.4. Oscillation decay parameters from experimental measurements.

Fuel	**Temperature [°C]**	**Droplet radius** [μm]	Oh	f_2 **[Hz]**	τ **[μs]**
Isobutanol	30	18.95	0.14	28659	22
	40	18.94	0.12	28918	26
	50	15.96	0.10	36626	24
	55	16.83	0.09	33553	31
PRF 84	30	20.93	0.03	24991	125
	40	19.64	0.03	27048	113
	50	20.63	0.03	24615	128
	55	21.12	0.03	23477	139

Table 3.4 includes the values for the Oh, which is a representation of the ratio of viscous forces to inertial and surface tension forces. The values of Oh have been studied by researchers in the past [41, 73] to suggest the applicability range of Lamb's theory, which is based on the irrotational flow assumption. If Oh is greater than $\sim$0.1, Lamb's theory may not be applicable. This issue will be discussed further in Section 3.4.3.

Table 3.5 shows the simulation results for a 40 μm diameter isobutanol droplet with shape oscillations at 55°C. Isocontour plots of the temperature field are overlaid to show the heat transfer process between the droplet and ambient air. The simulation results were processed in a similar procedure as the experimental results by extracting the ratio of A_2/R_0 and using Eq 3.2 to do damping curve fitting so that both the oscillation frequency and time constant can be obtained, and the oscillation decay curves can be drawn as shown in Figure 3.7. The curve fitting results for simulation results are expressed in the form of second-mode oscillation frequency and time constant, which are summarized in Table 3.6. Figure 3.7 shows eight damping curves for both isobutanol and PRF 84 at four different temperatures. Those four temperatures are the same as those in the experiments. The major difference between Table 3.6 and Table 3.4 is the initial droplet size. Given the motivation to study the impacts of temperature effects solely, simulation results in Table 3.6 represent the same trends as scaling analysis by using the same initial droplet size for all cases to emphasize the leading order temperature effects on the oscillation decay process.

Figure 3.7 shows the oscillation decay curves make a right-ward phase shift for both

Table 3.5. Simulation results showing the oscillation process for an isobutanol droplet at 55°C colored by temperature contours.

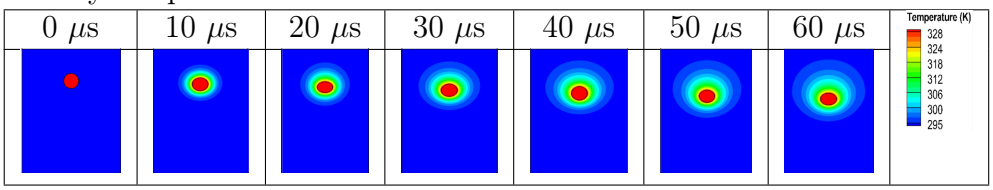

Table 3.6. Oscillation decay parameters from numerical simulations.

Fuel	**Temperature** [°C]	**Droplet radius** [μm]	Oh	f_2 **[Hz]**	τ [μs]
Isobutanol	30	20	0.15	26300	29
	40	20	0.12	26199	36
	50	20	0.09	26073	46
	55	20	0.08	25955	52
PRF 84	30	20	0.03	26380	126
	40	20	0.03	25980	131
	50	20	0.03	25585	127
	55	20	0.03	25357	131

fuels as temperature increases. This trend indicates a decreasing frequency and an increasing time constant. In Figure 3.7, the frequency decreased induced phase shift for PRF 84 is seen to be more pronounced than that for isobutanol. This is because PRF 84 has a greater oscillation frequency change with temperature. Figure 3.7 depicts cases with 20% initial deformation of amplitude. Consistent results were obtained when using 10% and 15% initial deformation.

3.4.2 Surface Tension and Viscosity Calculations

By substituting oscillation frequency and time constants from experiment and simulation into Eq. 2.2 and Eq. 2.3 based on Lamb's theory, surface tension and viscosity can be calculated. Tables 3.7 and 3.8 show the results from experiment and simulation with respect to literature data [63, 64, 76, 104]. In the experiments, there are multiple data sets for a specific temperature. So the average values of surface tension and viscosity for each fuel at certain temperatures are presented in these two tables. Deviations between average measurement data and literature data are calculated using Student's t-distribution. For pure component fuel, the calculation of surface tension and viscosity is quite straightforward by applying Eq. 2.2 and Eq. 2.3. But for multi-component fuels such as PRF 84, the

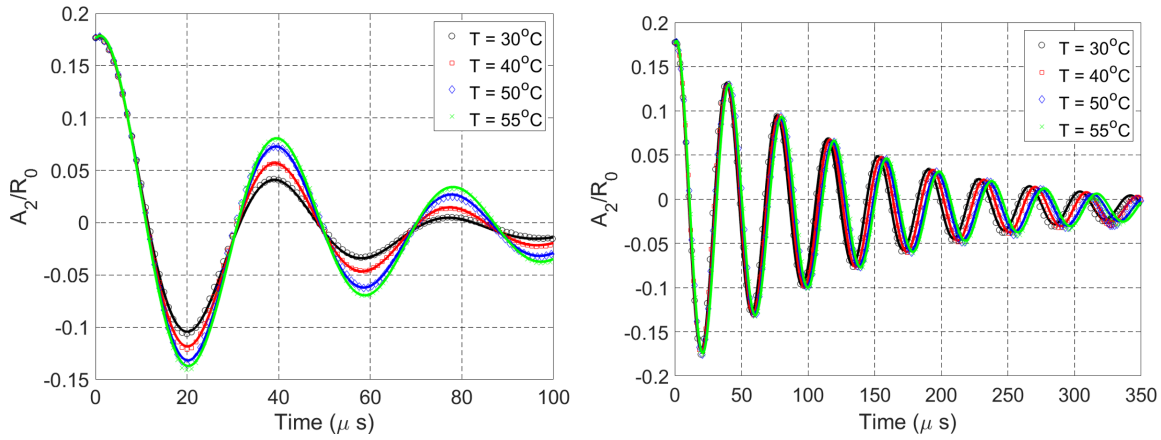

(a) Isobutanol (b) PRF 84

Figure 3.7. Droplet oscillation decay curves for fuels tested in this work at various temperatures – Simulation results.

surface tension and viscosity can be calculated using Eq. 3.3 and Eq. 3.4 by considering the mole fraction of each component.

$$\sigma_m = X_1\sigma_1 + X_2\sigma_2 \tag{3.3}$$

$$\ln \mu_m = X_1 \ln \mu_1 + X_2 \ln \mu_2 \tag{3.4}$$

where X_1 and X_2 are mole fractions. The literature data for each component of PRF 84 can be found in literature [63, 64, 104]. The uncertainty calculation with respect to the experimental data is based on Student's t-distribution at a 95% confidence interval, which is a suitable selection considering the sample size tested in the experiment.

Table 3.7. Surface tension and viscosity results for isobutanol.

	Viscosity [mPa·s]			**Surface Tension [mN/m]**		
Temperature	**Measurement**	**Simulation**	**Literature**	**Measurement**	**Simulation**	**Literature**
30	2.62±0.10	2.21	2.85	22.41±0.78	21.75	22.23
40	2.18±0.10	1.73	2.17	22.04±1.18	21.37	21.50
50	1.65±0.07	1.35	1.64	20.82±0.57	20.93	20.76
55	1.41±0.05	1.19	1.43	20.46±0.44	20.64	20.39

According to the results in Tables 3.7, for isobutanol, the maximum deviation between experimental data and literature data is 3% for surface tension and 8% for viscosity. The results in Tables 3.8 represent the maximum deviation between experimental data and

Table 3.8. Surface tension and viscosity results for PRF 84.

	Viscosity [mPa·s]			**Surface Tension [mN/m]**		
Temperature	**Measurement**	**Simulation**	**Literature**	**Measurement**	**Simulation**	**Literature**
30	0.47±0.01	0.44	0.46	19.24±0.24	18.91	18.14
40	0.45±0.02	0.42	0.44	18.45±0.24	18.14	17.23
50	0.45±0.01	0.42	0.43	17.52±0.34	17.37	16.33
55	0.42±0.03	0.41	0.41	16.53±1.82	16.93	15.89

literature data for PRF 84 is 7% for surface tension and 5% for viscosity. Simulation results show the maximum deviations of surface tension and viscosity for isobutanol are 5% and 22%, and for PRF 84 are 7% and 5%.

Simulation results with respect to viscosity are lower than the reference data for both two fuels. This prediction agrees with the results from some researchers [41, 83], who classified this underprediction effect to the irrotational flow assumption based on Lamb's theory. So both the oscillation decay rate and fuel viscosity are underpredicted.

Tables 3.7 and 3.8, as well as bar charts in Figure 3.8 show a clear trend of the decrease in surface tension and viscosity for both fuels as the temperature increases. Although the initial droplet size and operating parameters for droplet generation are not the same in each case thus impacting results for droplet oscillation frequency and time constants, these variations do not have any effects on the measurement results of surface tension and viscosity. The seemingly counter-intuitive finding follows the nature of small-amplitude oscillation decay process in reaching an equilibrium state as described by Lamb's theory. For the same fluid regardless of its original droplet size or velocity, its surface tension and viscosity would not change at a given temperature using Lamb's droplet oscillation theory. These results show the validity of using experiments to predict surface tension and viscosity of unknown fuels with unknown properties with reasonable accuracy and repeatability. Although there are non-idealities that have been expressed through heat and mass transfer and higher Oh number due to smaller droplet sizes, the experimental results are promising and can be applied for rapid fuel property screening.

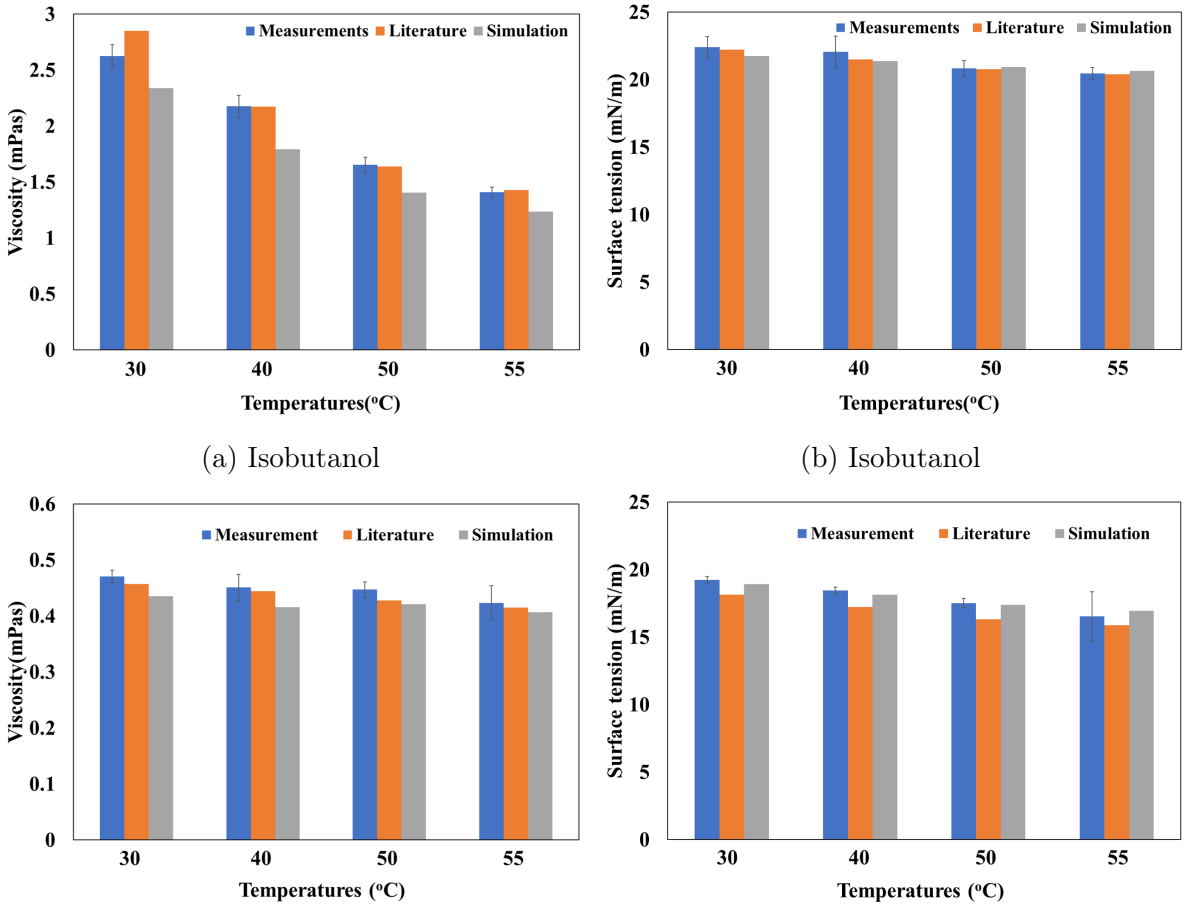

(a) Isobutanol

(b) Isobutanol

(c) PRF 84

(d) PRF 84

Figure 3.8. Results for viscosity and surface tension of the two fuels from measurements and simulations compared with reference data from literature.

3.4.3 Non-ideal Effects in Damped Oscillations

Given that simulations were carried out with constant initial droplet size and initial deformation rate different from experiments, non-ideal effects are analyzed based on the simulation data only. Non-ideal effects are related to droplet mass loss, heat transfer, and the impacts of Oh number on the droplet oscillation process.

The analysis of droplet size is the analysis of the equivalent radius of a sphere. The instantaneous droplet size is a function of polar angle. So the first step is to transform the instantaneous non-spherical droplet size to the equivalent spherical droplet size. From the simulation results, the equivalent radius shows less than 0.2% decrease for isobutanol and 1% decrease for PRF 84 for all the cases. The reason for the higher droplet size change for

PRF 84 attributes to lower heat of vaporization (HOV) values for PRF 84 (321 KJ/kg), while isobutanol has HOV of 693 KJ/kg. So PRF 84 has a higher evaporation rate than isobutanol at the same temperature.

Transient simulation results were used to calculate the temperature field of the droplet during the oscillation process. The maximum temperature drops for isobutanol and PRF 84 were predicted to be 2% and 12% with respect to the cases at 55 °C. PRF 84 has a larger temperature drop than isobutanol. Since PRF 84 has a lower HOV and higher evaporation rate that lead to a higher vapor mass fraction at the interface at a certain temperature. The maximum temperature drop for isobutanol can incur 0.4% decrease in surface tension and 1% decrease in viscosity. The maximum temperature drop for PRF 84 can bring about 3% decrease in surface tension and 5% decrease in viscosity. Simulation for temperature field can not only obtain the bulk temperature change of the droplet, but also capture the non-uniformity in temperature changes within the droplet during the oscillation process. Figure 3.9 compares two plots for the changes of droplet bulk temperature during the whole oscillation period for two fuels. PRF 84 shows a larger temperature drop than isobutanol. The maximum bulk temperature drop is about 7°C for PRF 84 droplet at 55 °C. Figure 3.10 shows two plots with temperature distribution within the isobutanol and PRF 84 droplets at 55 °C at different times during the oscillation period. Isobutanol droplet shows an almost uniform temperature distribution within the droplet. On the other hand, PRF 84 has some temperature gradients inside the droplet with no more than 8°C temperature drop during oscillation for the cases at initial temperature of 55 °C. Although both temperature non-uniformity within the droplet and bulk temperature drop of the droplet have comparable values of temperature reductions during the oscillation decay process, their impacts on the predictions of surface tension and viscosity are minimal as above analysis.

Lamb's theory [61] is based on an irrotational flow assumption. Previous work [41, 73] studied this assumption and vorticity generation related fuel physical properties and changes in droplet size through the Oh number. At a high Oh number, the viscosity term

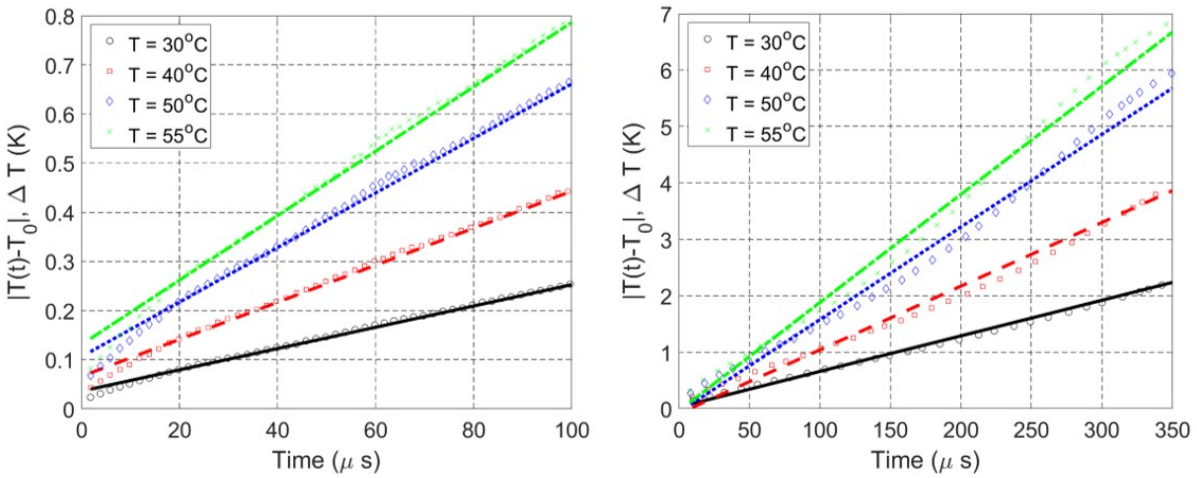

(a) Isobutanol (b) PRF 84

Figure 3.9. Bulk temperature drop during oscillation process for isobtuanol and PRF 84.

has significant impacts on momentum and interfacial stress balance equations that makes the irrotational flow assumption invalid. Some researchers [105, 106, 107] used a linear stability analysis to study the impacts of viscosity on droplet oscillation. For a viscous fuel droplet, the oscillation frequency and time constant can be expressed as the roots of the characteristic equation as shown in Eq. 3.5.

$$-\frac{(\omega_{\mathrm{n}})^2}{\beta^2}+\frac{2(\mathrm{n}^2-1)}{\kappa^2{\mathrm{R}_0}^2-2\kappa\mathrm{R}_0Q_{\mathrm{n}+1/2}}-1+\frac{2\mathrm{n}(\mathrm{n}-1)}{\kappa^2{\mathrm{R}_0}^2}\left[1-\frac{(\mathrm{n}+1)\mathrm{Q}_{\mathrm{n}+1/2}}{0.5\kappa\mathrm{R}_0-\mathrm{Q}_{\mathrm{n}+1/2}}\right]=0 \qquad (3.5)$$

where,

$$Q_{\mathrm{n}+1/2}=\frac{\mathrm{J}_{\mathrm{n}+3/2}(\kappa\mathrm{R}_0)}{\mathrm{J}_{\mathrm{n}+1/2}(\kappa\mathrm{R}_0)}, \qquad \kappa=\sqrt[2]{\frac{\beta\rho_l}{\mu_l}} \qquad \beta={\omega_{\mathrm{n}}}^*+i\,({\tau_{\mathrm{n}}}^*)^{-1}$$

Eq. 3.5 was numerically solved to find out the error introduced by the irrotational flow assumption. The solution process follows the work of Suryanarayana et al [108] to obtain surface tension and viscosity as a function of Oh number. This solution is applicable for the oscillation process of a viscous droplet with negligible ambient gas density, negligible internal droplet motion, and gravitational effects. Therefore, this solution is feasible to be used for fluids with higher viscosity, such as isobutanol, to provide an estimation for the

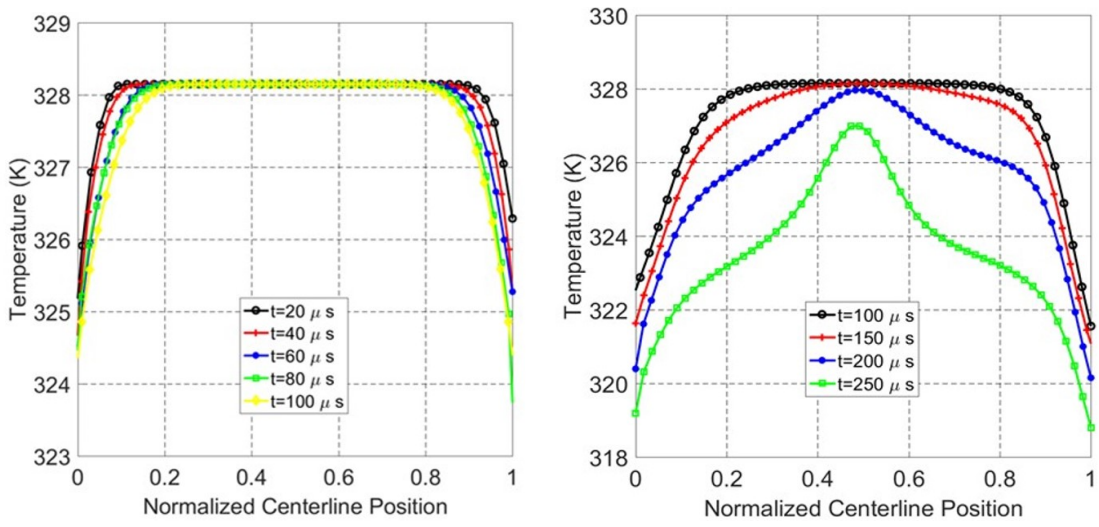

(a) Isobutanol (b) PRF 84

Figure 3.10. Transient centerline temperature distribution within droplets of isobutanol and PRF 84 at 55 °C.

errors from viscous effects.

Figure 3.11 shows two ways to calculate errors of surface tension and viscosity. One way uses the Eq. 3.5 for the "predicted error" calculation, which is shown in Figure 3.11 including the viscous effects that were overlooked by Lamb's theory. The other way is based on Lamb's equation (Equations 2.2 and 2.3) for the "observed simulation error" calculation, which shows the difference between the simulation results based on Lamb's theory and literature data. Figure 3.11 indicates that the first way of the error calculation by Eq. 3.5 overpredicts the error from viscous effects for both two fuels. From the magnitudes of the errors from both two ways, the contribution of viscous effects on the oscillation decay process is large.

Isobutanol has a higher Oh number than PRF 84 due to higher viscous effects. Oh number is closely related to vorticity and droplet size. Hence it is is easier to form vortices in isobutanol than PRF 84 at the interface which subsequently diffuses into the center of the droplet [109]. Also, the droplet size in this work is small (about 40 μm), which leads to a higher Oh number. Figure 3.12 shows these effects using simulation results by plotting time evolution of normalized vorticity as a function of radial distance for two fuels at 30°C.

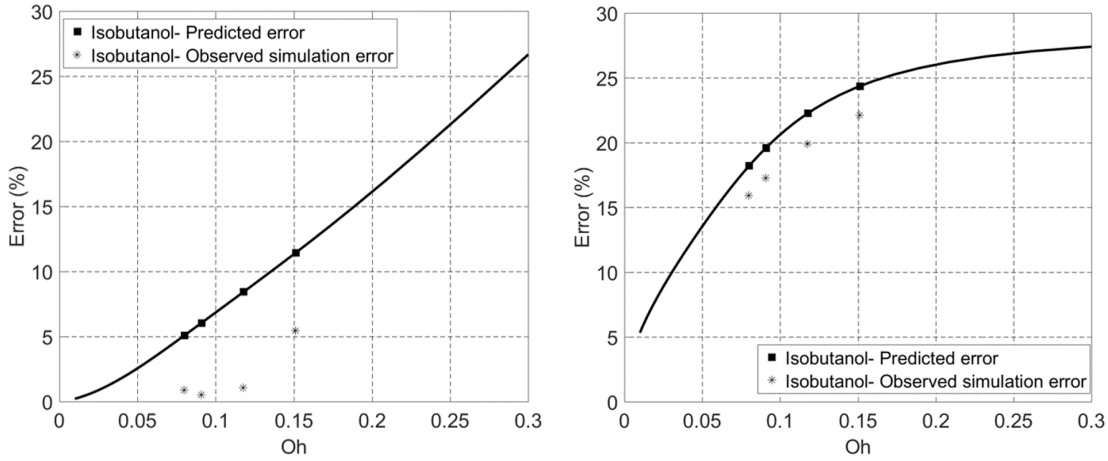

(a) Surface tension (b) Viscosity

Figure 3.11. Error in viscosity and surface tension arising from viscous effects.

Vorticity has the highest magnitude at the interface between droplet and air. The value of vorticity decreases towards the center of the droplet. Considering isobutanol has a higher Oh number, vorticity diffuses faster than PRF 84. This causes isobutanol to deviate from the inviscid and irrotational flow assumption. Figure 3.13 is the isocontours of normalized vorticity. Isobutanol shows higher values of vorticity than PRF 84 at the interface. This shows that tracking changes in the Oh number can be used to capture the deviation from the irrotational flow assumption. Factors that make Oh number vary include the changes in fluid properties, temperature, or droplet size.

To sum up, viscous effects induced by a higher Oh number have the highest impact on the error in surface tension and viscosity prediction. The bulk temperature drop and non-uniform temperature distribution within the droplet have less impact on error than viscous effects. Mass loss due to evaporation appears to have the lowest impact on error.

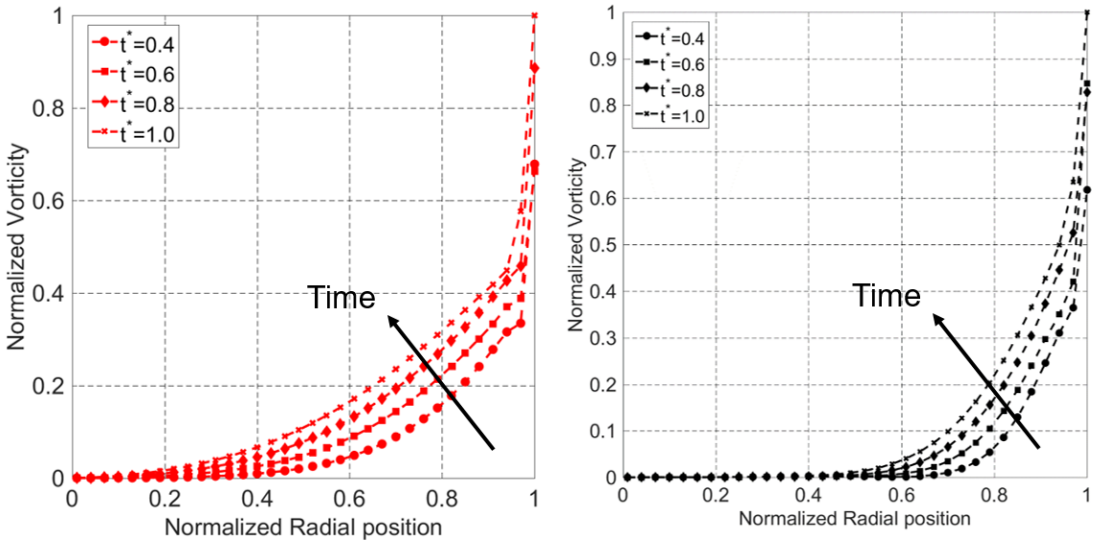

(a) Isobutanol, Oh=0.15 (b) PRF 84, Oh=0.03

Figure 3.12. Time evolution of normalized vorticity as a function of radial distance for the two tested fuels at the same initial temperature of 30°C.

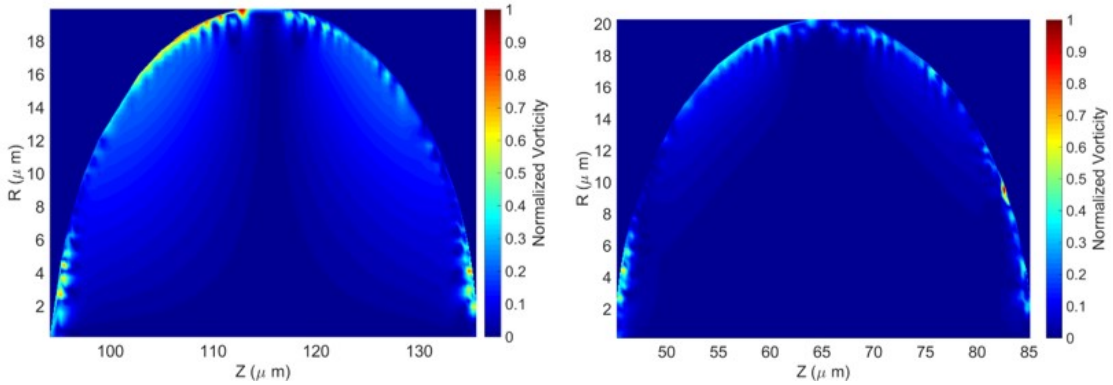

(a) Isobutanol (b) PRF 84

Figure 3.13. Detailed normalized vorticity for isobtuanol and PRF 84.

Chapter 4
Droplet-based Heat of Vaporization and Vapor Pressure Measurement

Once the fuels are atomized into a distribution of finely-sized droplets, evaporation and fuel-air mixing processes are directly associated with the heat of vaporization and vapor pressure of the fuel, as dictated by the ambient conditions surrounding the fuel droplets [6]. Heat of vaporization (HOV) or latent heat is the energy required for phase change of the liquid fuel. Vapor pressure (P_{vap}) is a measure of the pressure exerted by the fuel vapor in thermodynamic equilibrium condition with its liquid phase. Heat of vaporization (HOV) and vapor pressure (P_{vap}) can be related to each other through the Clausius-Clapeyron equation.

Given the importance of HOV and P_{vap} for evaporation and fuel/air mixing, it is now attempted to pursue droplet-based approaches to measure these properties.

This chapter is outlined as follows. The approach section discusses three algorithms for HOV and P_{vap} calculations based on an inverse AS (Abramzon and Sirignano) model. The focus of this work is to use the Scheme-I algorithm for the calculations. Then, the experiment section describes the experimental setup, measurement procedure, image processing, and fuels tested. In the results and discussion section, the measurements from fuel droplet evaporation experiments at different temperatures are supplied as inputs to Scheme-I so that HOV and P_{vap} can be obtained. The fuels being tested include pure fuels and a gasoline surrogate. Results are discussed and conclusions are presented.

4.1 Approach

In previous chapters, a droplet oscillation based approach for the measurement of surface tension and viscosity at both ambient and elevated temperatures has been presented. Droplets were generated using a piezoelectric droplet generator. The sample size is on the scale of μl. The proposed approach in this chapter intends to use the droplet evaporation process after oscillation, to measure HOV and P_{vap}. The combination of the previous droplet oscillation based approach and the current droplet evaporation approach is able

to constitute a streamlined approach by utilizing the minute volume of the fuel with μl in sample size and having data collection only in ms. Thus, the whole process from droplet jetting until evaporation ensures a rapid screening approach for physical properties measurements utilizing with small sample size in ms. Finally, with minor modifications and packaging, it is possible to integrate the physical property evaluation techniques based on droplet oscillation and evaporation with chemical kinetic property evaluation techniques being developed using a micro-combustor setup [66].

There are several review articles [110, 111, 112] about the modeling of the droplet evaporation process. Droplets being studied are either stationary or moving in a controlled temperature environment. Factors that impact the droplet evaporation process include heat and mass transfer between the droplet and ambient gas, HOV, second-order effects such as circulation within the droplet, gas motion around the droplet, and water condensation on the droplet surface. The approach used in this chapter is to apply an existing droplet evaporation model [110] for the calculations of HOV and P_{vap}. The droplet size change as a function of time, which is measured by an experimental setup, is used as the input to the model. HOV and P_{vap} are coupled to each other through the Clausius-Clapeyron equation.

Ray [113] used a similar approach by observing the size change of evaporating droplets at stationary conditions through droplet levitation to estimate the ultra-low vapor pressure of the fluids in aerosol research. An MLE (Maximum Likelihood Estimation) approach was used by Ray to determine physical properties such as HOV and P_{vap}, and molecular dynamic parameters such as the Lennard–Jones potential parameters. The current approach differs from Ray's paper in several aspects. Ray used stationary droplets by levitation, while this work uses moving droplets giving a simpler experimental setup. Ray's method only applies to liquid with low volatility, while this work can be used for fuels with high volatility. This work utilizes the Abramzon and Sirignano (AS) model [110] to simulate the evaporation process of moving droplets. The Abramzon model incorporates Stefan flow and effects of convective heat and mass transfer using a "film theory", which in essence in-

troduces a vapor-gas film between the droplet surface and ambient atmosphere, effectively providing resistance to heat and mass exchange as shown schematically in Figure 4.1. Model assumptions include quasi-steady heat and mass transfer, temperature dependent thermophysical properties, uniform temperature and fuel vapor concentration on the droplet surface, spatially uniform but time-varying droplet temperature, and no velocity field within the droplet.

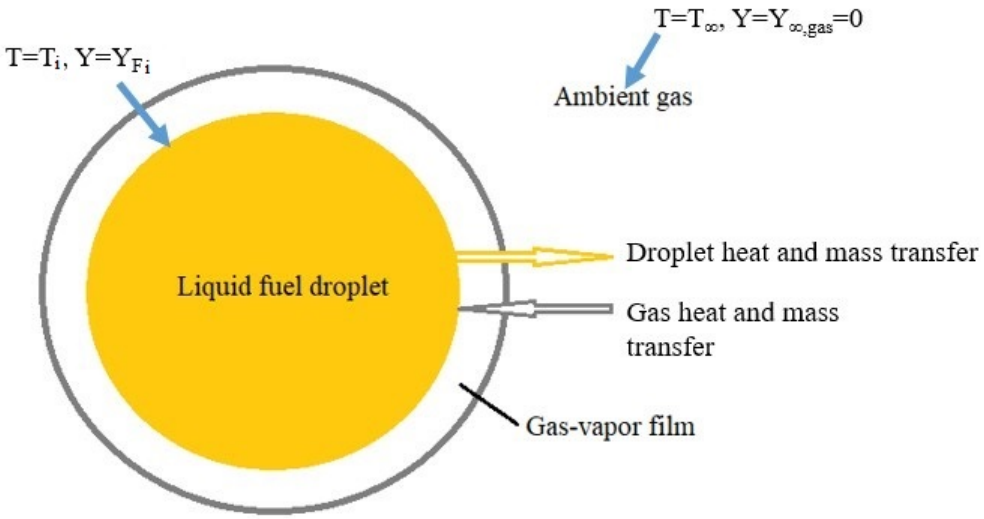

Figure 4.1. Droplet evaporation model incorporating the liquid-vapor film.

Source terms considered in the model include:

- **Droplet velocity:**

$$\frac{du}{dt} = -\frac{3C_D\bar{\rho}_f}{4D_l\rho_l}(u-u_\infty)^2 + g_0\left(1-\frac{\bar{\rho}_f}{\rho_l}\right) \tag{4.1}$$

  where $\bar{\rho}_f$ is the density of the vapor in the film, g_0 is the acceleration due to gravity, C_D is the drag coefficient, u is the droplet velocity, u_∞ is the ambient gas velocity, D_l is the droplet diameter and ρ_l is the liquid density.

- **Droplet diameter:**

$$\frac{dD_l}{dt} = -\frac{2\dot{m}_l}{\pi\rho_l D_l^2} \tag{4.2}$$

where $\dot{m}_l$ is the instantaneous evaporation rate of the droplet in kg/s.

- **Droplet temperature:**

$$\frac{dT_l}{dt} = \frac{\dot{Q}_l}{m_l C_{pl}} \tag{4.3}$$

where $\dot{Q}_l$ is the rate of heat transfer to the liquid droplet and m_l is the mass of the droplet.

In the above transient governing equations, C_D, $\dot{m}_l$, and $\dot{Q}_l$ are defined based on the operating conditions and properties of the fuel and carrier gas. From the mass and energy balance equations at the interface, evaporation rate, $\dot{m}_l$ is defined as:

$$\dot{m}_l = \pi \bar{\rho}_f \bar{D}_{fc} D_l \mathrm{Sh}^* ln(1 + B_M) = \pi \frac{\bar{k}_g}{\bar{C}_{pF}} D_l \mathrm{Nu}^* ln(1 + B_T) \tag{4.4}$$

where,

$$B_M = \frac{(Y_{Fi} - Y_{F\infty})}{(1 - Y_{F\infty})}, \quad B_T = \frac{\bar{C}_{pF}(T_\infty - T_i)}{H_f(T_i) + \frac{\dot{Q}_L}{\dot{m}_l}} \tag{4.5}$$

In the above equations, $\bar{D}_{fc}$ is the diffusion coefficient of the gas mixture in the film, B_M refers to the mass transfer number, calculated from fuel vapor mass fraction at the droplet interface (Y_{Fi}) and in the far-field ambient ($Y_{F\infty} = 0$), and B_T refers to the heat transfer number, calculated from the droplet interface temperature T_i, far-field ambient temperature T_∞, heat of vaporization of the fuel H_f evaluated at droplet temperature T_i and the average specific heat of fuel vapor in film ($\bar{C}_{pF}$) evaluated at film temperature $\bar{T}_{fi}$. Nu^* and Sh^* are the modified Nusselt number and Sherwood number, respectively, for a spherical droplet, considering the effect of blowing. The definition of Nusselt number, Sherwood number, and film temperature, based on the work of Abramzon et al [110], is provided in Appendix B.

The heat transfer rate $\dot{Q}_l$ can be evaluated using the combined equations of heat transfer number (Eq. 4.5) and interfacial energy balance (Eq. 4.4). In the transient equation for

droplet velocity (Eq. 4.1), drag coefficient C_D for spheres is based on the correlation for "standard drag curve", which is quite accurate when Re<1000, provided in the work of Putnam et al [114], defined as:

$$C_D = \frac{24}{Re}\left\{1 + \frac{Re^{2/3}}{6}\right\} \tag{4.6}$$

where Re is the Reynolds number, defined as $\frac{\bar{\rho}_f D_l |u - u_\infty|}{\bar{\mu}_f}$. All the gas properties in the film are defined as a function of average fuel vapor mass fraction $\bar{Y}_f$ in the film and average temperature of the film ($\bar{T}_{fi}$). The equations used for film properties, used in the current work, are detailed in Appendix B.

In the conventional AS method, the governing equations given by Equations 4.1, 4.2, 4.3, and 4.4 are solved using an explicit transient solver. Both the fuel transport properties and initial conditions are the inputs to the model. In Figure 4.2 regarding the simulation results of PRF-84 droplet evaporation at two ambient air temperatures, it is obvious to see that after the initial transients within the initial 10 ms, the temperature (T_i) and velocity of the droplet reach a quasi-steady-state and the square of droplet diameter (D_l^2) exhibits a quasi-linear behavior (constant slope) with time. This work is desired to implement an inverse AS algorithm that uses measurement data from observations of droplet evaporation at steady states at controlled conditions as inputs to estimate unknown fuel physical properties. In pursuing this goal, there are multiple ways of using the above logic to obtain the physical properties of the fuels depending on how many parameters including droplet size, velocity, and temperature can be measured in the experiments. The more parameters we can measure, the more physical properties of the fuels can be derived, since those measured quantities are used as inputs to different algorithms. Some physical properties for the unknown fuel may also be required as inputs to the algorithm. These details are summarized in Tables 4.1, 4.2, and 4.3. Each table provides details of the inputs involving the measured quantities and known physical properties required for each inverse AS algorithm. Also, the outcomes of the numerical predictions are presented in the form of properties with a tick

symbol. Note that properties mentioned in all three tables pertain to the values for the fuel vapor. Further, numerical predictions obtained for fuel physical properties correspond to those at a steady state temperature (T_i) as reached by a droplet during droplet evaporation measurements.

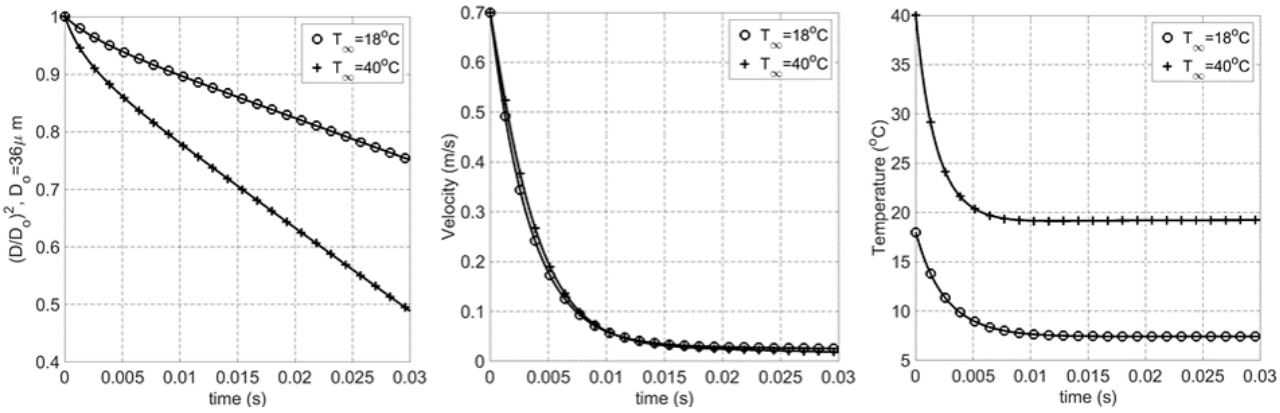

Figure 4.2. Predictions for droplet evaporation using the AS model for a droplet of PRF-84 at two different ambient temperatures showing variation of the square of the droplet diameter, droplet velocity, and droplet temperature as a function of time.

Table 4.1. Summary of required inputs and the outputs predicted by the numerical method, (**Scheme-I**)

Input Data		**Numerical predictions**
Measurements	**Properties**	
• $\frac{dD_l^2}{dt}$, D_l (Droplet diameter)	• Density (Liquid, vapor) • Viscosity • Thermal conductivity • Specific heat • Diffusion coefficient • Boiling point	✓ Vapor pressure, P_{vap} ✓ Heat of vaporization, H_f

As is summarized in Table 4.1, 4.2, and 4.3, the different schemes utilize different numbers of measured quantities and known physical properties as inputs to give numerical predictions for unknown physical properties. As can be observed, as the number

Table 4.2. Summary of required inputs and the outputs predicted by the numerical method, (**Scheme-II**)

Input Data		**Numerical predictions**
Measurements	**Properties**	
• $\frac{dD_l^2}{dt}$, D_l (Droplet diameter) • $\frac{du}{dt}$, u (Droplet velocity)	• Density • Viscosity • Thermal conductivity • Specific heat • Boiling point	✓ Vapor pressure, P_{vap} ✓ Heat of vaporization, H_f ✓ Diffusion coefficients ✓ Lennard Jones, (σ, ϵ)

Table 4.3. Summary of required inputs and the outputs predicted by the numerical method, (**Scheme-III**)

Input Data		**Numerical predictions**
Measurements	**Properties**	
• $\frac{dD_l^2}{dt}$, D_l (Droplet diameter) • $\frac{du}{dt}$, u (Droplet velocity) • T_i (Droplet temperature)	• Density • Viscosity • Thermal conductivity	✓ Vapor pressure, P_{vap} ✓ Heat of vaporization, H_f ✓ Diffusion coefficients ✓ Lennard Jones, (σ, ϵ) ✓ Specific heat $(\bar{C}_{PF})$ ✓ Boiling point, (T_{boil})

of measured quantities increases from Table 4.1 to Table 4.3, the required number of known physical properties to be used as inputs to the algorithm decreases. Further, in the case of Scheme-II and III, it is noted that more measurement data should be taken from droplet evaporation experiments. Numerical predictions listed for each scheme represent temperature-dependent values that can be obtained from the calculations except for

Lennard Jones parameters which are temperature-independent. In this work, the major focus is on predictions of temperature-dependent HOV and P_{vap}. Accordingly, the details of Scheme-I as summarized in Table 4.1 is the selected algorithm in this work. While pursuing Scheme-I does imply that several physical properties of the fuel of interest are known beforehand and used as inputs to the algorithm, successful implementation of the algorithm will validate the approach and lay the groundwork for the pursuit of Scheme-II and III in future studies.

In the **Scheme-I** algorithm summarized in Table 4.1, droplet diameter and the quasi-linear slope of change in square of droplet diameter (D_l^2), are provided by the experiment. Fuel vapor properties are evaluated using empirical/analytical equations. Using these inputs, droplet temperature (T_i), temperature specific vapor pressure (P_{vap}) and heat of vaporization (H_f) can be evaluated using an iterative approach. The algorithm for the Scheme-I approach is shown in the form of a flowchart in Figure. 4.3.

The detailed description of each step in the **Scheme-I** algorithm is listed below:

1. To start the algorithm, the initial droplet temperature is assumed to be equal to far-field ambient temperature ($T_i = T_\infty$). This temperature will be corrected iteratively.

2. Using the droplet temperature (T_i), experimental data, and property inputs as listed in Table 4.1, the interfacial mass balance equation is solved for fuel vapor mass fraction at the droplet interface. Accordingly, Eq. 4.4 can be rewritten as an implicit function of droplet temperature and interface fuel mass fraction.

$$\dot{m} - \pi \bar{\rho}_f \bar{D}_{fc} D_l \mathrm{Sh}^* ln(1 + B_M) = F(Y_{Fi}, T_i) = 0 \tag{4.7}$$

   The above equation can be solved for unknown interface mass fraction Y_{Fi}, using any standard root finding technique. It is to be noted that the mass flow rate ($\dot{m}$) and droplet diameter (D_l) used in Eq. 4.7 correspond to values after a steady-state droplet temperature is achieved.

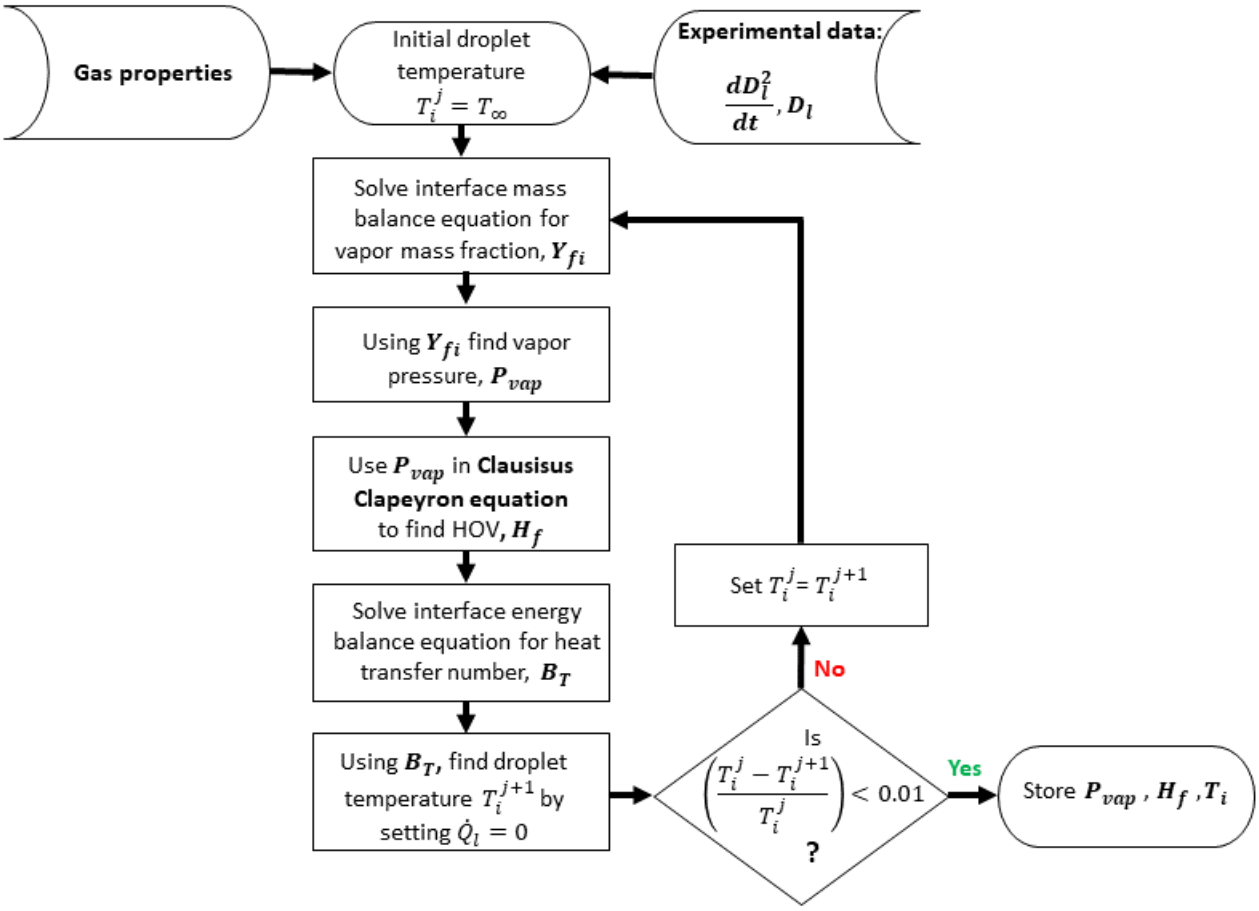

Figure 4.3. Flowchart showing approach used in HOV and vapor pressure estimation using measurements and the droplet evaporation model **(Scheme-I)**.

3. The interface mass fraction (Y_{Fi}) is utilized to find the instantaneous vapor pressure of the droplet, which is defined as

$$P_{vap} = P_\infty \left\{ \frac{Y_{Fi} MW_c}{MW_F + Y_{Fi}(MW_c - MW_F)} \right\} \tag{4.8}$$

where MW is the molecular weight of carrier gas (subscript 'c') and fuel (subscript 'F').

4. With P_{vap} as the input, HOV is evaluated using the Clausius-Clapeyron equation, as shown below:

$$H_f = -\ln\left(\frac{P_{vap}}{P_\infty}\right) \frac{R_u}{MW_F \left[\frac{1}{T_i} - \frac{1}{T_{boil}}\right]} \tag{4.9}$$

where T_{boil} is the fuel boiling point at the ambient pressure during the experiment.

5. The interface mass fraction is further utilized to evaluate the heat transfer number B_T. Similar to step 2, the interfacial energy balance equation Eq. 4.4 can be rewritten as an implicit function of B_T, T_i and Y_{Fi}, given by:

$$\dot{m} - \pi \frac{\bar{k}_g}{\bar{C}_{pF}} D_l \mathrm{Nu}^* ln(1 + B_T) = G(Y_{Fi}, T_i, B_T) = 0 \tag{4.10}$$

   The above equation is solved for unknown heat transfer number B_T, using any standard root finding technique.

6. As observed from simulations using the AS model, the fuel droplet reaches a quasi-steady temperature, after the initial transients, which implies that the net heat transfer rate $\dot{Q}_l = 0$. Using this observation, the equation for heat transfer number B_T (Eq. 4.5), is modified for the unknown droplet temperature T_i.

$$T_i = \frac{-B_T H_f}{\bar{C}_{pF}} + T_\infty \tag{4.11}$$

7. The droplet temperature is updated using the above value and the Steps 1 to 6 are repeated until the temperature change, from the previous iteration, is negligible (until convergence). In the numerical trials conducted, convergence was observed in less than 15 iterations.

The algorithm Scheme-I is now used with evaporation measurements for various fuels of interest to demonstrate the validity of the approach.

4.2 Experiment

4.2.1 Experimental Setup

The experimental setup for droplet evaporation is shown schematically in Figure 4.4. A piezoelectric droplet generator (Microfab PH-41, 30μm nozzle) is placed inside a closed, cylindrical metal chamber, and used to inject a continuous stream of droplets into the

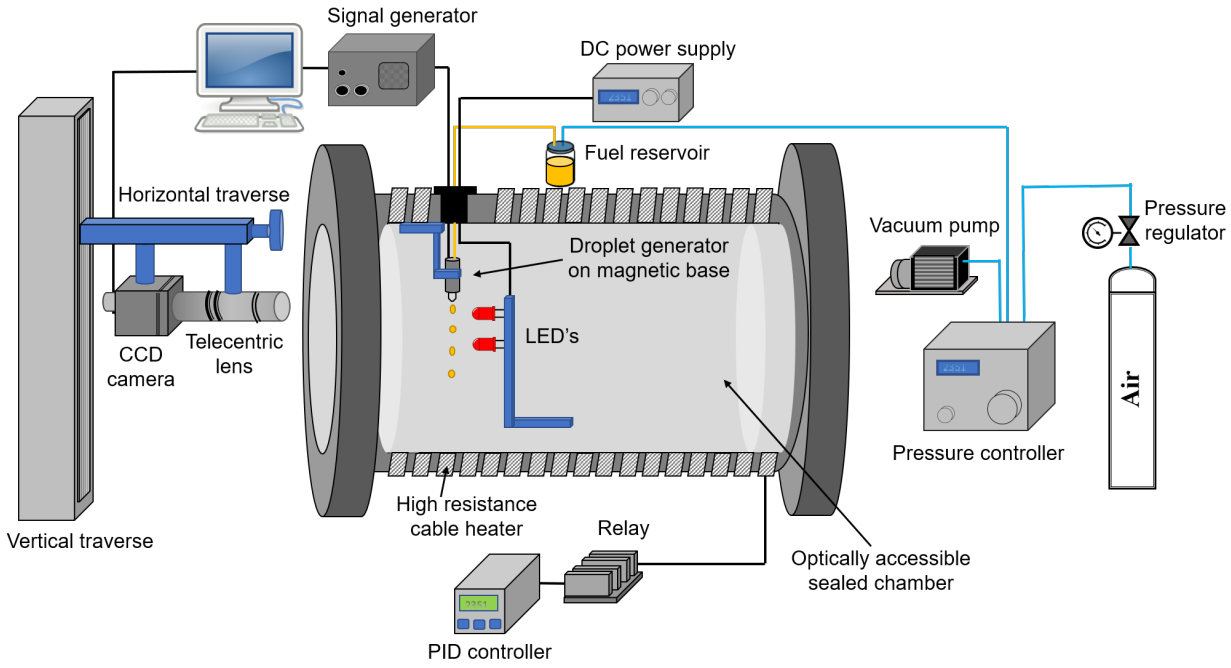

Figure 4.4. Droplet evaporation experimental setup.

chamber. A PID controller (Extech 48VFL) along with a heating element wrapped around the chamber is used to control the chamber temperature. Fuel is supplied to the droplet generator from a reservoir kept outside the chamber at room temperature (22°C). A signal generator (Microfab JetDrive V (CT-M5-01)) provides pulses to actuate the droplet generator. The piezoelectric element on the actuator expands or contracts according to the polarity of the signal. Droplets are formed at the nozzle tip as a result of the fast deformation of the piezoelectric material. A pressure controller (MicroFab CT-PT-21) is used to select positive or negative back pressure to sustain a balancing force on the fluid column at the exit plane of the nozzle. The back pressure is provided by a compressed air source and a vacuum pump (Koge electronic, KPV20A-6A), which respectively provide positive and negative back pressures to the pressure controller.

The frequency of the waveform pulse controls the droplet spacing. A machine vision camera (Sentech STC-MB33USB) mounted on a vertical traverse is used to obtain a live video of the droplet trail within the chamber. Images are extracted from the video for processing. The camera has optical access into the chamber through the quartz windows

located on either side of the pressure chamber. The camera has a resolution of 4.56 μm/pixel using a Precise Eye lens with adapter 1-61445. The light source for the camera is comprised of four LEDs (Broadcom HLMP- CM1A-560DD), which are soldered on a circuit board located inside the chamber and provided with constant voltage using an external power supply (BK Precision Model 1621A).

4.2.2 Measurement Procedure

To conduct the tests, the chamber doors are closed at atmospheric pressure. Next, the temperature controller is set to the desired set-point for chamber ambient temperature. Chamber ambient temperature is monitored at different locations until they reach steady state values. This typically takes about 30-40 minutes. Once the desired temperature is reached inside the chamber, the back pressure controller is used to purge some of the fuel thereby producing a well-defined liquid meniscus that can be seen from the camera interface to a computer. Next, using the back pressure controller, the meniscus is carefully aligned with the exit plane of the glass nozzle. Once aligned, the desired waveform pulse is applied to produce the liquid droplet train with the required frequency. The camera is used to take a live video of the droplet trail at various downstream locations from the nozzle by moving it using the vertical traverse. The distance that the camera moves along the vertical traverse is measured using a fixed graduated ruler mounted inside the chamber or by measuring the relative vertical distance between two adjacent droplets in the same droplet trail. Distance measurements are facilitated by an image calibration that provides a pixel to micron conversion. Using the calibration, droplet size and location from the nozzle exit are determined. Images are also used for droplet velocity measurement. Given the highly repeatable nature of the droplet generation process, it is possible to directly use the distances between consecutive droplets with the timescale for droplet generation to estimate droplet velocity. The timescale between two adjacent droplets during droplet generation corresponds to the inverse of the operating frequency of the droplet generator, which is maintained constant during the experiment.

4.2.3 Image Processing

Image processing and analysis to capture the droplet edge and estimate droplet diameter was carried out using a custom Matlab package. The process includes background subtraction, batch cropping, anisotropic filtering, and edge detection by a Subpixel method to capture the droplet shape. A detailed description of these steps can be found in previous work [85].

4.2.4 Fuels Tested

Fuels of interest to this work comprise pure components and blends which have been researched as part of the DOE Co-Optima program to develop bioblendstocks for use in advanced internal combustion (IC) engines. While this includes a large number of pure components and blends, the current work focuses on a subset of these as listed in Table 4.4. Tests were conducted using pure *n*-heptane, isobutanol, and PRF 84. *n*-heptane has a Cetane number similar to that of commercial diesel fuel and has been used as a diesel surrogate in the studies of advanced combustion strategies, such as Homogeneous Charge Compression Ignition (HCCI) [115] and Reactivity Controlled Compression Ignition (RCCI) [116]. Isobutanol has been identified by DOE's Co-Optima program as being one of the top ten bioblendstocks for turbocharged gasoline engines [3] and can be directly produced from biomass [117]. PRF 84 represents a simple two-component gasoline surrogate used in conventional Spark Ignition IC engines [90].

Table 4.4 lists reference values for various fuel physical properties including RVP and vapor pressure measured at 100°F (37.8°C). It is seen that while RVP measurement requires evaluating vapor pressure at 100°F and a vapor/liquid ratio of 4:1, a rough estimate of RVP can be obtained simply by considering the fuel vapor pressure at 100°F. This approach is assumed to be acceptable for fuel screening, which forms the ultimate goal of the methods proposed in this work to evaluate fuel physical properties.

Table 4.4. Properties of fuels tested in this work as relevant for use in advanced SI engines [63, 118].

Name	**Functional group**	**Formula**	**Boiling Point**	**RVP**	**Vapor pressure @ 100°F**	**HOV @ 25°C**
n-heptane	Alkane	C_7H_{16}	98.4	12.4	11.1	364.8
Isobutanol	Alcohol	$C_4H_{10}O$	108	3.3	3.3	692.5
PRF-84	Blend	16% C_7H_{16}, 84%C_8H_{18}	98.7	N/A	11.6	319.8
			$°C$	kPa	kPa	kJ/kg

4.3 Results and discussion

4.3.1 Measurements

Figure 4.5 is a composite image showing a continuous trail of n-heptane droplets generated by the droplet generator. Figure 4.5 also shows droplet size and velocity changes during the evaporation process as the droplets move downstream from the nozzle exit. The square of the droplet diameter is plotted as a function of time and shows a quasi-linear slope. Droplet velocity is seen to decrease during an initial transient. This results from the drag experienced by the droplets once they are propelled from the exit plane of the nozzle by the motion of the piezoelectric droplet generator.

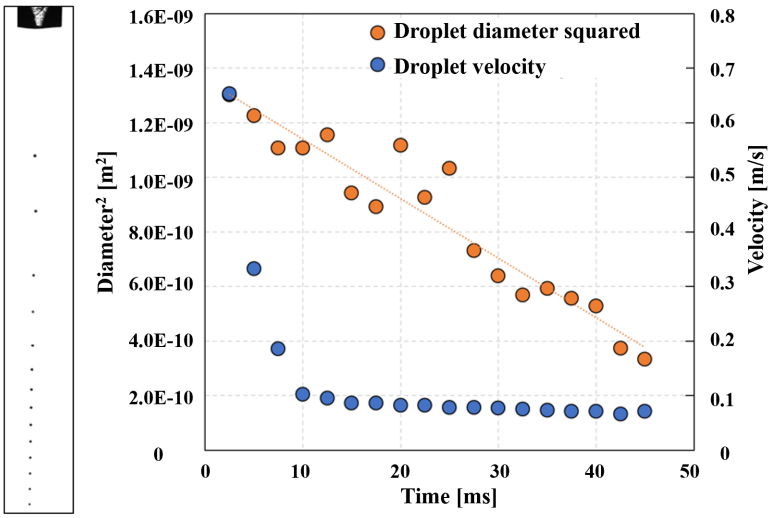

Figure 4.5. Composite of camera images showing a trail of n-heptane droplets after leaving the nozzle orifice.

Figure 4.6 shows the evaporation rate expressed as dD^2/dt as a function of ambient

temperature for the three different fuels tested in this study. As can be observed, dD^2/dt increases with temperature for all fuels as expected. Further, dD^2/dt for n-heptane closely tracks that of PRF 84 given that the second component making up PRF 84 (*iso*octane) has a volatility, very similar to that of n-heptane. Table 4.4 shows that isobutanol has a lower vapor pressure than the other two fuels, which leads to a lower evaporation rate for the same ambient temperature. Figure 4.6 also represents the uncertainty estimates for each fuel at different ambient temperatures. The uncertainty estimates have been obtained using a Student's t-distribution as appropriate for a small sample size with a 95% confidence interval. The sources of the uncertainties come from the resolution of the imaging setup and the droplet edge detection techniques.

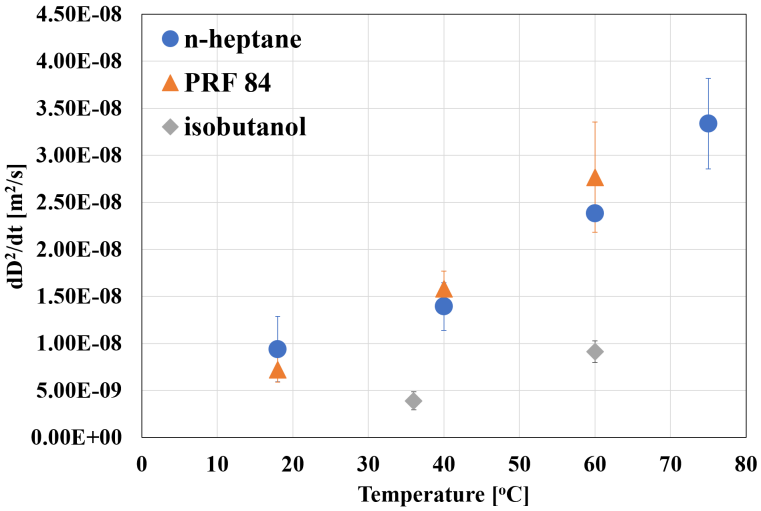

Figure 4.6. Evaporation rate as expressed by the change in diameter-squared as a function of ambient temperature for the fuels tested in this work.

4.3.2 Physical Property Predictions Using Scheme I

Figure 4.7 shows droplet temperature and predicted HOV during the course of the solution procedure used for Scheme-I as summarized in Table 4.1. As observed in Figure 4.7, the solution converges within 4–5 iterations.

Table 4.5 shows the results obtained from Scheme-I calculations using experimental measurements at different ambient temperatures reported in Figure 4.6. Predicted values for temperature dependent HOV and vapor pressure for the three fuels tested in this work are presented along with reference values obtained from the literature. It should be noted

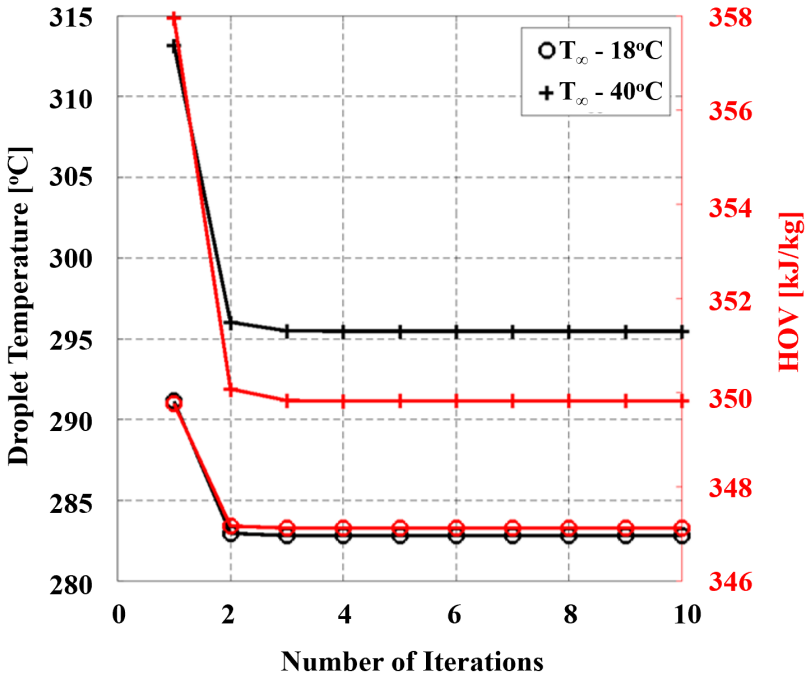

Figure 4.7. Droplet temperature and HOV as a function of the iteration number for PRF-84 at two different ambient temperatures.

Table 4.5. Results from calculations using Scheme-I.

Fuel	**Temperature**	**HOV**			**Vapor Pressure**		
		Predicted	Reference	Deviation	Predicted	Reference	Deviation
n-heptane	18	340 ± 50	374	9.1	2.78 ± 0.9	2.41	15.4
	40	390 ± 40	367	6.4	3.86 ± 0.7	4.6	16
	60	370 ± 10	363	2.1	6.51 ± 0.1	6.84	4.9
	75	364 ± 40	360	1.1	8.44 ± 1.2	8.71	3.1
PRF 84	18	343 ± 20	328	4.7	2.04 ± 0.4	2.60	21.7
	40	339 ± 20	323	5.3	4.13 ± 0.5	4.88	15.3
	60	325 ± 50	318	2.2	6.83 ± 1.4	7.34	6.9
isobutanol	36	676 ±60	690	2.0	1.39 ± 0.3	1.44	3.0
	60	673 ± 50	674	0.1	3.02 ± 0.4	3.18	5.0
	°C	kJ/kg		%	kPa		%

that data presented in Table 4.5 and further plotted in Figure 4.8 are results averaged over multiple experimental data sets. Table 4.5 includes uncertainties calculated using Student's t-distribution as discussed earlier. Deviation reported in Table 4.5 is computed as the difference between predicted and reference values.

Figure 4.8 shows predicted HOV and vapor pressure as a function of ambient temper-

atures. Results shown in Table 4.5 and Figure 4.8 indicate a deviation of 0.1-9% in HOV prediction and 3-22% in vapor pressure prediction. Literature data are overlaid on the plots for direct comparison with the predicted data. As observed in the figure, HOV is relatively insensitive to temperature. Vapor pressure shows higher sensitivity to temperature and increases with temperatures. Figure 4.8 also shows a higher HOV for isobutanol, which is also consistent with its lower vapor pressure, given its lower volatility. Predicted results for *n*-heptane and PRF 84 closely follow each other consistent with the similar evaporation rate for both fuels as presented in Figure 4.6.

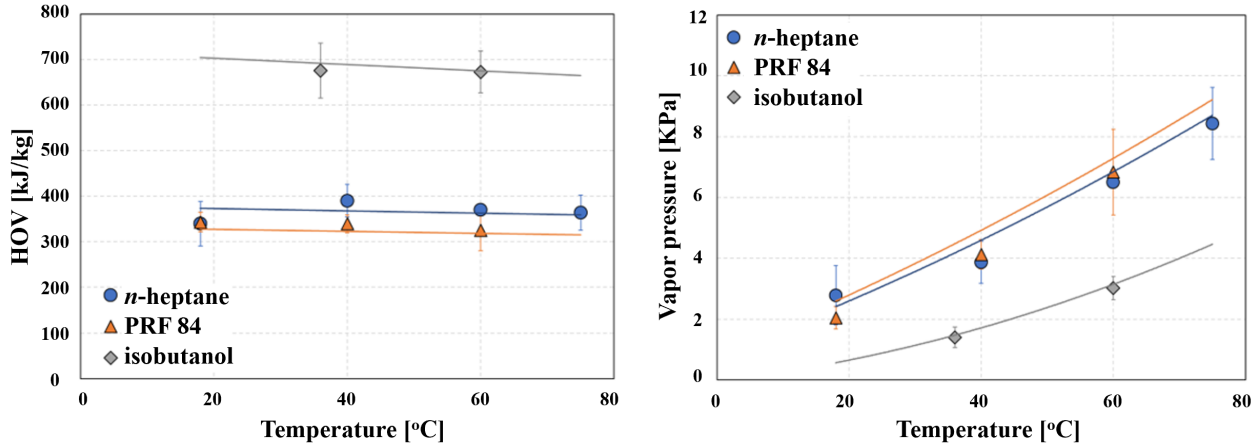

Figure 4.8. HOV and vapor pressure predictions as a function of ambient temperature for the three fuels tested in this work.

Figure 4.9 shows bar charts comparing predictions for HOV at 25°C and RVP of the three fuels tested in this work. HOV is obtained by interpolating data shown in Figure 4.8. A similar procedure is followed to determine RVP by interpolating data for vapor pressure as presented in Figure 4.8 to obtain the vapor pressure at a droplet temperature of 37.8°C. However, the ambient air temperature that corresponds to droplet temperature of 37.8°C is very close to 95°C for *n*-heptane and PRF 84, which is outside of the temperature range of the current experiment setup as Figure 4.8 show. In the current setup, the ambient air temperature inside the chamber cannot exceed 80°C to prevent the severe nozzle clogging issue and unstable droplet generation. The deviation in HOV for predictions as compared to reference values is observed to be in the range of 2–3%. However, for RVP, higher

deviations are observed in the range of 10–15%. The higher deviations observed for RVP can be attributed to the error in droplet evaporation rate measurement and the use of the Clausius-Clapeyron equation shown as Eq. 4.9 to relate HOV to vapor pressure. As seen from Eq. 4.9, small errors in HOV and droplet temperature can lead to large errors in vapor pressure due to the exponential nature of the relationship. This trend can be observed in Figure 4.10, which shows the sensitivity of error induced in vapor pressure due to error in HOV for isobutanol at 40°C.

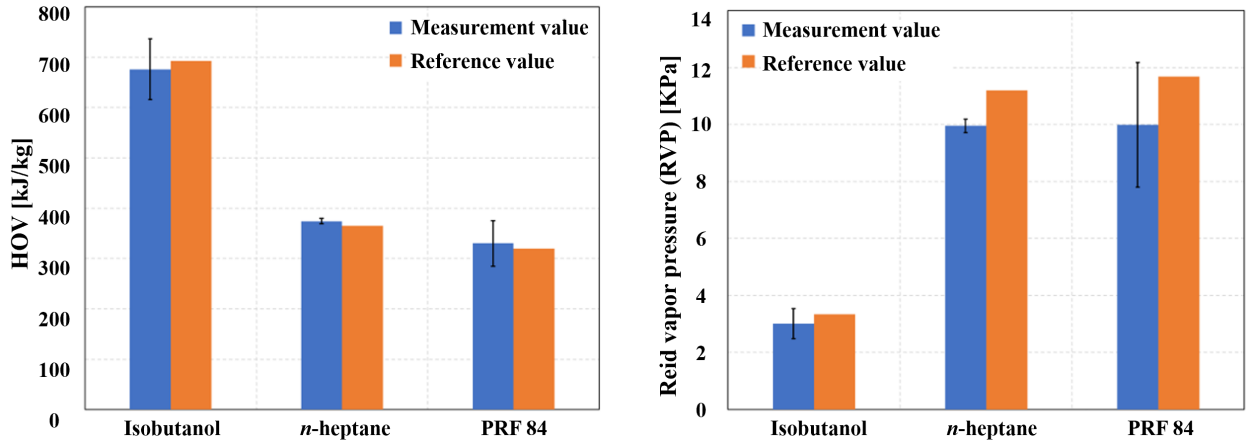

Figure 4.9. Measurement results compared with reference data for HOV estimated at 25°C and RVP estimated at 37.8°C. Both temperatures refer to the fuel temperature.

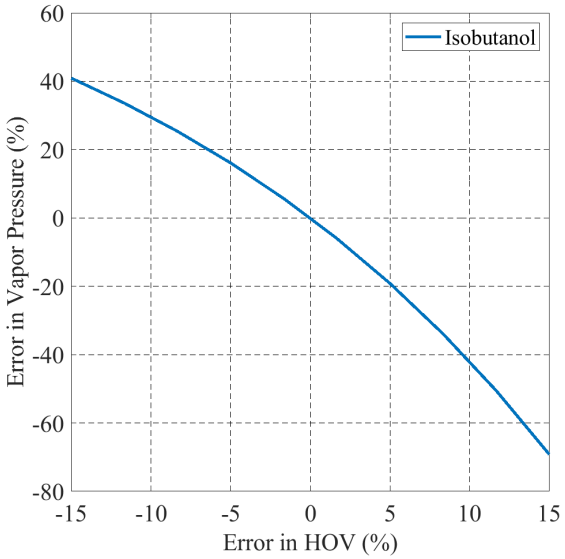

Figure 4.10. Sensitivity analysis of vapor pressure error induced by HOV error at 40°C.

The baseline Scheme-I algorithm requires the droplet evaporation rate, while Scheme-

II & III additionally require droplet velocity and droplet temperature. Although droplet velocity could be measured using the current setup as Figure 4.5 shows, more reference measurements are required to verify the results of droplet velocity measurements from the current setup. Therefore, only Scheme-I is included in this work.

Chapter 5
Conclusions and Future Work

5.1 Conclusions

The development of bioblendstocks for emerging fuels compatible with advanced SI engines requires approaches to evaluate fuel physical properties relevant to engine performance. The large number of possible bioblendstocks that can be produced motivates the development of screening approaches that can utilize small quantities of liquid fuels and rapidly evaluate relevant properties. This work presents droplet-based approaches to measure several physical properties including surface tension, viscosity, heat of vaporization, and Reid vapor pressure of candidate liquid fuels using micro-liter quantities using droplet oscillation and droplet evaporation.

Damped, decaying oscillation dynamics of single droplets are used to measure fuel surface tension and viscosity. The oscillation of single droplets produced by a piezoelectric droplet generator is analyzed using hardware triggered stroboscopic imaging. Image processing and edge detection techniques are used to obtain the droplet radius as a function of polar angle during the course of its motion. The oscillation of the second-order mode and its damping is analyzed to obtain a decay time constant as well as a fundamental frequency, which can be related to fuel viscosity and surface tension. Measurements are obtained for primary reference fuels (isooctane and n-heptane) as well as candidate biofuels from the alcohol, ketone, ester, and furan functional groups. Experimental results are compared with literature data as well as measurements obtained using reference instruments. Droplet oscillation measurement results show a maximum of 7% deviation in surface tension and 13% deviation in viscosity from literature data. The uncertainty in surface tension measurement through droplet oscillation ranges from 1–5% while that in viscosity ranges from 3–12%. The repeatability of the droplet oscillation process was confirmed through direct imaging. Measurement results for the current set of fuels utilized an average of 5 μL per fuel and required about 20 s per sample for data collection. In comparison, standard

tensiometers and viscometers require about 15 ml and 7 ml of fuel sample respectively, and require about 2-3 minutes of operation each, to generate surface tension and viscosity measurements. Overall, the measurements show that the droplet oscillation dynamics based technique using a piezoelectric droplet generator provides a pathway to develop a small-volume, high-throughput fuel screening technique.

Droplet oscillation dynamics were further used to evaluate the effects of elevated temperatures on surface tension and viscosity of hydrocarbon fuels. The experimental approach, utilizing a droplet generator setup was shown to be capable of measuring fluid properties using $\mathcal{O}(\mu\text{l})$ of fuel based on stable generation of 35–60 μm diameter droplets. Measurement results showed deviations within $\sim$10% from literature values for viscosity and surface tension over the range 30–55°C. The oscillation decay process, which forms a central part of the measurement, is shown to be dependent on fluid properties, which affect oscillation frequency as well as decay time. While experiments are shown capable of measuring physical properties, lack of independent control on droplet size and temperature precludes observation of expected trends predicted by a simple scaling analysis. These trends, which include a decrease in oscillation frequency and an increase in oscillation decay time with an increase in fluid temperature are observed using numerical simulations, which permit independent control on droplet size and temperature. The numerical simulations incorporated all the relevant physics of the experiment including heat and mass transfer from the droplet with interface capture implemented using a Volume-Of-Fluid approach.

Simulation results are further used to evaluate the effect of non-idealities introduced by the experiment including droplet heat and mass transfer, as well as the irrotational flow assumption in the droplet oscillation theory. The latter is particularly relevant to this work given that the small size of droplets used in this work (35-60 μm in diameter) cause an increase in the Ohnesorge number, which has been critically linked to the irrotational flow assumption. Simulation data are analyzed to determine droplet mass loss due to evaporation and temperature drop due to heat loss. The effect of mass loss during the

short oscillation period ($\approx$ 350 μs) is found to be negligible with less than 1% change in diameter change. Temperature change is found to have a stronger effect, particularly for the more volatile fuel, PRF 84, accounting for up to 3% error in surface tension and 5% error in viscosity for the highest temperature case of 55°C. Corresponding values for isobutanol are 0.4% and 1%. The contribution of viscous effects was investigated using the predictions of an analytical model developed for a fluid droplet at the viscous limit, which was numerically solved. The results, which are valid for the more viscous fuel, isobutanol, suggest that viscous effects are responsible for a significant part of the error introduced in oscillation decay rate, and hence the fluid viscosity, calculated using the linear droplet oscillation theory developed for an inviscid, irrotational case. This finding reinforces the influence of the Ohnesorge number and its physical manifestation through vorticity generation as a limitation on the use of droplet oscillation theory to calculate fluid physical properties.

Results from experiments and simulations indicate that the oscillation decay process can be successfully used with heated droplets moving through an ambient environment to determine temperature-dependent properties of fluids with unknown chemical composition using fuel samples of $\sim$0.6 μl. In comparison, viscometers are available commercially that can operate with fuel samples of 1 μl while tensiometers require sample sizes of the order of 0.5 ml. This is a significant finding that can aid the development of rapid screening tools for down selecting candidate biomass-derived fuel molecules for investigation as drop-in replacements for conventional hydrocarbon fuels. However, for cases involving fluids or conditions resulting in a higher Ohnesorge number, particularly greater than $\sim$0.1, efforts should be directed towards an improved formulation of the droplet oscillation decay theory, where the potential flow assumption can be relaxed or eliminated.

Finally, a droplet evaporation-based approach was used for the measurement of heat of vaporization and vapor pressure of liquid hydrocarbon fuels including pure component and two-component fuels. The approach is based on the measurement of evaporation

rates of single liquid droplets of the fuel as they move through an isothermal chamber and use evaporation rate along with the Abramzon-Sirignano droplet evaporation model to estimate heat of vaporization. The Clausius-Clapeyron equation is used to determine vapor pressure. This approach is applied to determine heat of vaporization and vapor pressure for isobutanol, *n*-heptane, and PRF 84 as functions of temperature. Results obtained from calculations are compared with literature data. The deviation in HOV for predictions as compared to reference values is observed to be in the range of 2–3%. However, for RVP, higher deviations are observed in the range of 10–15%. The larger deviations for RVP potentially arise due to the use of the Clausius-Clapeyron equation. The proposed approach described as Scheme-I, nonetheless demonstrates the validity of using droplet evaporation measurements with a model for droplet evaporation to predict fuel physical properties. Additional Schemes described as Scheme II & III can be derived where progressively more inputs obtained from experimental measurements can be used to increase the number and accuracy of fuel property predictions.

Overall, droplet-based fuel property measurements based on droplet oscillation dynamics and evaporation processes are proven to be viable approaches for the prediction of physical properties including surface tension, viscosity, heat of vaporization, and RVP with good accuracy.

5.2 Future Work

Future work should focus on the following aspects.

1. To study oscillation dynamics for cases with a high Oh number, such as larger than 0.1, work is required to find improved formulations to express droplet oscillation decay theory when the irrotational flow assumption is not fully satisfied.

2. There is significant potential for continued development of droplet-based property measurement techniques to include multi-component fuels over a larger range of temperatures and pressures including preferential evaporation effects.

3. There is potential to improve the accuracy of fuel property predictions through

improvement in diagnostic techniques. This includes the potential use of techniques such as holography to measure droplet size and shape, and laser-based techniques such as PDPA (Phase Doppler Particle Analyzer) to measure droplet size and velocity, LIF (Laser-Induced Fluorescence) to measure droplet temperature, and PIV (Particle Image Velocimetry) to measure droplet flow field and internal circulation. These measurements can also facilitate the use of Schemes II & III to measure additional fuel properties.

4. There are opportunities to extend droplet-based techniques to combustion-specific property measurements. This includes measurements of PMI (Particulate Matter Index) for soot emission prediction using droplet combustion experiments.

Appendix A
Supplemental Information for Chapter 3

Table A.1. Empirical relationships for temperature dependent physical properties of fuels considered in this work.

Property (ϕ)	$\phi = AT^3 + BT^2 + CT + D$ (T is in deg K)		
	Isobutanol	PRF 84	
		Isooctane	***n*-heptane**
Viscosity (Pa.s)	A=0, B=7.157×10^{-7}, vc C=-5.085×10^{-4}, D=9.1×10^{-2}	A=-2×10^{-9}, B=1.838×10^{-6} , C=-5.634×10^{-4}, D=5.81×10^{-2}	A=0, B=5×10^{-8} , C=-3.46×10^{-5}, D=6.257×10^{-3}
Surface tension (N/m)	A, B=0, C=-7.3747×10^{-5}, D=4.457×10^{-2}	A, B=0, C=-8.76×10^{-5}, D=4.44×10^{-2}	A, B=0, C=-9.919×10^{-5}, D=4.934×10^{-2}
Thermal conductivity (W/m-K)	A, B=0, C=-2×10^{-4}, D=1.916×10^{-1}	A, B=0, C=-2.25×10^{-4}, D=1.62×10^{-1}	A, B=0, C=-2.941×10^{-4}, D=2.10×10^{-1}
Density (kg/m3)	A, B=0, C=-8.438×10^{-1}, D=1.0486×10^{3}	A, B=0, C=-8.6471×10^{-1}, D=9.4794×10^{2}	A, B=0, C=-8.836×10^{-1}, D=9.4559×10^{2}
Specific heat (J/kg-K)	A, B=0, C=2.0089×10^{1}, D=-3.5831×10^{3}	A=0, B=-2.9183×10^{-2}, C=2.1283×10^{1}, D=-1.6695×10^{3}	A, B=0, C=3.3492, D=1.2284×10^{3}

Appendix B
Supplemental Information for Chapter 4

1. Modified Nusselt number:

Nu^*=2+(Nu_o-2)/F_T

where F_T=F(B_T)=$(1 + B_T)^{0.7}$ ln(1+B_T)/B_T

Nu_o=2+0.552$Re^{1/2}Pr^{1/3}$

2. Modified Sherwood number:

Sh^*=2+(Sh_o-2)/F_M

where F_M=F(B_M)=$(1 + B_M)^{0.7}$ ln(1+B_M)/B_M

Sh_o=2+0.552$Re^{1/2}Sc^{1/3}$

B_T and B_M are Spalding heat and mass transfer number.

3. Film temperature:

$\overline{T_f}$=T_s+1/3(T_∞-T_s)

4. Fuel vapor mass fraction in the film:

$\overline{Y_f}$=$Y_f s$+1/3($Y_{f\infty}$-Y_{fs})

Appendix C
Supplemental Information for High Pressure Droplet Generation Setup

Figure C.1 shows a test setup for 500 psi droplet generation. The tube includes two layers. The outer tube has an inner diameter of 18 mm with maximum hoop stress of 2300 psi. The inner tube has an inner diameter of 1 mm with maximum hoop stress of 835 psi. Heated air flows from the outer tube to the inner tube. Gaskets at two ends of the outer tube provide sealing. The tube is sandwiched between two endplates. This setup can provide good optical access for droplet visualization and can accommodate the variable length of the tubes. Figure C.3 shows the actual assembly of the setup that was verified to operate successfully with 30 bar. The original goal was to integrate this setup with a micro-combustor so that both physical properties and combustion metrics of fuels in $\mathcal{O}(\mu l)$ can be obtained in a streamlined fashion.

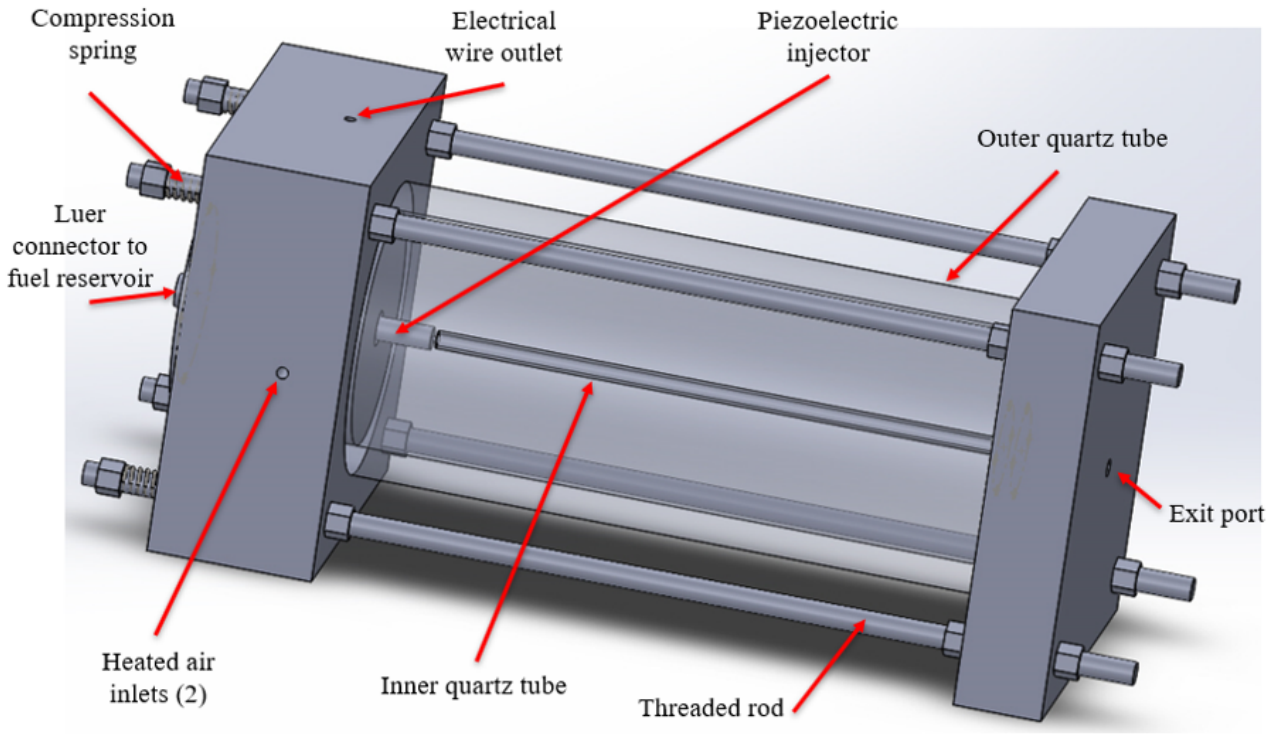

Figure C.1. Setup for 500 psi droplet generation with heated air co-flow.

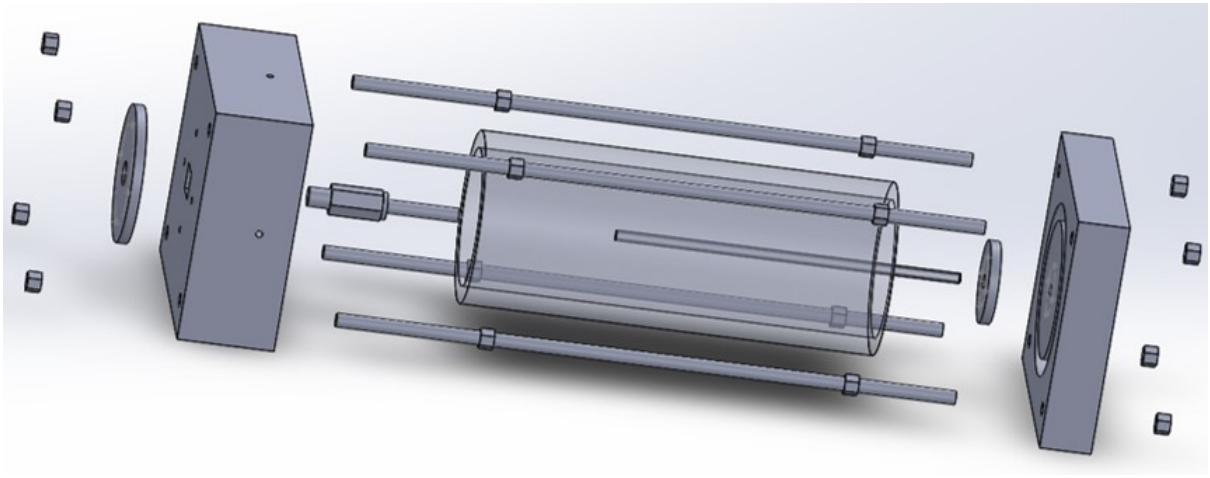

Figure C.2. Exploded view of the setup.

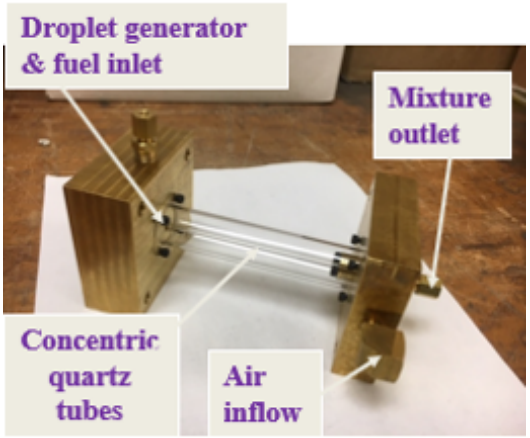

Figure C.3. Actual setup photo.

Appendix D
Permission to Use Copyrighted Materials

D.1 Copyright to Chapter 2

Chapter 2 was previously published as Dang, W., Zhao, W., Schoegl, I., & Menon, S. (2020). A small-volume, high-throughput approach for surface tension and viscosity measurements of liquid fuels. Measurement Science and Technology, 31(9), 095301. Reproduced with permission from © IOP Publishing. All rights reserved.

9/22/21, 9:07 PM https://marketplace.copyright.com/rs-ui-web/mp/license/9e7873ba-411c-40df-97da-82327af56116/9e13b2f5-89c2-42ad-8e55-5fa1...

CCC Marketplace™

This is a License Agreement between Wanjun Dang ("You") and IOP Publishing, Ltd ("Publisher") provided by Copyright Clearance Center ("CCC"). The license consists of your order details, the terms and conditions provided by IOP Publishing, Ltd, and the CCC terms and conditions.

All payments must be made in full to CCC.

Order Date	12-Mar-2021	Type of Use	Republish in a thesis/dissertation
Order License ID	1103763-1		
ISSN	1361-6501	Publisher	IOP Publishing
		Portion	Chapter/article

LICENSED CONTENT

Publication Title	Measurement Science and Technology	Rightsholder	IOP Publishing, Ltd
		Publication Type	e-Journal
Article Title	A small-volume, high-throughput approach for surface tension and viscosity measurements of liquid fuels	Start Page	095301
		Issue	9
		Volume	31
		URL	http://www.iop.org/Journals/mt
Author/Editor	Institute of Physics (Great Britain)		
Date	12/31/1995		
Language	English		
Country	United Kingdom of Great Britain and Northern Ireland		

REQUEST DETAILS

Portion Type	Chapter/article	Rights Requested	Main product
Page range(s)	1-11	Distribution	Worldwide
Total number of pages	11	Translation	Original language of publication
Format (select all that apply)	Electronic	Copies for the disabled?	Yes
Who will republish the content?	Academic institution	Minor editing privileges?	Yes
Duration of Use	Life of current edition	Incidental promotional use?	No
Lifetime Unit Quantity	Up to 499	Currency	USD

NEW WORK DETAILS

Title	Droplet-based fuel property measurements	Institution name	Louisiana State University
		Expected presentation date	2021-05-20
Instructor name	Shyam Menon		

ADDITIONAL DETAILS

https://marketplace.copyright.com/rs-ui-web/mp/license/9e7873ba-411c-40df-97da-82327af56116/9e13b2f5-89c2-42ad-8e55-5fa10e59aaa7 1/5

Order reference number	N/A	The requesting person / organization to appear on the license	Wanjun Dang

REUSE CONTENT DETAILS

Title, description or numeric reference of the portion(s)	Droplet-based surface tension and viscosity measurement at ambient conditions	Title of the article/chapter the portion is from	A small-volume, high-throughput approach for surface tension and viscosity measurements of liquid fuels
Editor of portion(s)	Menon, Shyam; Schoegl, Ingmar; Zhao, Wei; Dang, Wanjun	Author of portion(s)	Menon, Shyam; Schoegl, Ingmar; Zhao, Wei; Dang, Wanjun
Volume of serial or monograph	31	Issue, if republishing an article from a serial	9
Page or page range of portion	095301	Publication date of portion	2020-04-19

D.2 Copyright to Chapter 3

begell
New York • Connecticut

50 North Street
Danbury, CT 06810
203-456-6161
journals@begellhouse.com
www.begellhouse.com

September 15, 2021

Wanjun Dang
PhD Student LSU

Re: Permission to Reprint Material

Dear Wanjun Dang,

Permission is hereby granted to use **part or all material** from the following article published by Begell House: "Temperature Effects On Droplet Oscillation Decay With Application To Fuel Property Measurement" by W. Dang, M. Gurunadhan, I. Schoegl & S. Menon.

Proposed Use: The material will be used online as part of a PhD Thesis entitled "Droplet-Based Fuel Property Measurements"

Publisher: Louisiana State Univeristy

Year of Publication: 2021

As per your email, we hereby grant you permission to reproduce the aforementioned material in print and electronic format at no charge subject to the following conditions:

1 – If any part of the material to be used (for example, figures) has appeared in our publication with credit or acknowledgement to another source, permission must also be sought from that source. If such permission is not obtained then that material may not be included in your publication.

2 – Suitable acknowledgement to the source must be made, either as a footnote or in a reference list at the end of your publication, as follows:

"Reprinted from Publication title, Volume number, Author(s), Title of article, Page Nos., Copyright (Year), with permission from Begell House, Inc.

3 – Reproduction of this material is confined to the purpose for which permission is hereby given.

Yours sincerely

Brandon T. Bisceglia

Brandon T. Bisceglia
Begell House Inc.

References

[1] J. Farrell, J. Holladay, and R. Wagner, "Fuel blendstocks with the potential to optimize future gasoline engine performance: identification of five chemical families for detailed evaluation," US Department of Energy, Washington, DC, Tech. Rep., 2018.

[2] J. T. Farrell, R. Wagner, D. Gaspar, and C. Moen, "Co-optimization of fuels & engines: Fy18 year in review," National Renewable Energy Lab.(NREL), Golden, CO (United States), Tech. Rep., 2019.

[3] D. Gaspar, "Top ten blendstocks for turbocharged gasoline engines: bio-blendstocks with the potential to deliver the highest engine efficiency," *PNNL-28713, Pacific Northwest National Laboratory*, 2019.

[4] R. L. McCormick, G. Fioroni, L. Fouts, E. Christensen, J. Yanowitz, E. Polikarpov, K. Albrecht, D. J. Gaspar, J. Gladden, and A. George, "Selection criteria and screening of potential biomass-derived streams as fuel blendstocks for advanced spark-ignition engines," *SAE International Journal of Fuels and Lubricants*, vol. 10, no. 2, pp. 442–460, 2017.

[5] R. L. McCormick, "Selection criteria for sustainable fuels for high-efficiency spark-ignition engines with examination of their storage stability, impact on engine knock, and fine particle emissions," National Renewable Energy Lab.(NREL), Golden, CO (United States), Tech. Rep., 2018.

[6] M. A. Ratcliff, B. Windom, G. M. Fioroni, P. S. John, S. Burke, J. Burton, E. D. Christensen, P. Sindler, and R. L. McCormick, "Impact of ethanol blending into gasoline on aromatic compound evaporation and particle emissions from a gasoline direct injection engine," *Applied Energy*, vol. 250, pp. 1618–1631, 2019.

[7] K. Luo, C. Shao, M. Chai, and J. Fan, "Level set method for atomization and evaporation simulations," *Progress in Energy and Combustion Science*, vol. 73, pp. 65–94, 2019.

[8] M. Mägi, "Effect of gasoline fuel additives on combustion and engine performance," Ph.D. dissertation, UCL (University College London), 2015.

[9] A. Davanlou, J. D. Lee, S. Basu, and R. Kumar, "Effect of viscosity and surface tension on breakup and coalescence of bicomponent sprays," *Chemical engineering science*, vol. 131, pp. 243–255, 2015.

[10] I. Ruiz-Rodriguez, R. Pos, T. Megaritis, and L. C. Ganippa, "Investigation of spray angle measurement techniques," *IEEE Access*, vol. 7, pp. 22 276–22 289, 2019.

[11] D. C. K. Rao, S. Karmakar, and S. Basu, "Atomization characteristics and instabilities in the combustion of multi-component fuel droplets with high volatility differential," *Scientific reports*, vol. 7, no. 1, pp. 1–15, 2017.

[12] M. Jain, R. S. Prakash, G. Tomar, and R. Ravikrishna, "Secondary breakup of a drop at moderate weber numbers," *Proceedings of the Royal Society A: Mathematical, Physical and Engineering Sciences*, vol. 471, no. 2177, p. 20140930, 2015.

[13] A. H. Lefebvre and D. R. Ballal, *Gas turbine combustion: alternative fuels and emissions*. CRC press, 2010.

[14] Z. Yue and S. Som, "Fuel property effects on spray atomization process in gasoline direct injection," SAE Technical Paper, Tech. Rep., 2020.

[15] W. Zeng, M. Xu, M. Zhang, Y. Zhang, and D. J. Cleary, "Macroscopic characteristics for direct-injection multi-hole sprays using dimensionless analysis," *Experimental thermal and fluid science*, vol. 40, pp. 81–92, 2012.

[16] D. J. Gaspar, S. D. Phillips, E. Polikarpov, K. O. Albrecht, S. B. Jones, A. George, A. Landera, D. M. Santosa, D. T. Howe, A. G. Baldwin *et al.*, "Measuring and predicting the vapor pressure of gasoline containing oxygenates," *Fuel*, vol. 243, pp. 630–644, 2019.

[17] S. V. D. Freitas, M. J. Pratas, R. Ceriani, S. Lima, and J. A. P. Coutinho, "Evaluation of predictive models for the viscosity of biodiesel," *Energy & Fuels*, vol. 25, no. 1, pp. 352–358, 2011.

[18] "Evaluation of the oxidative stability of corn biodiesel," *Fuel*, vol. 90, no. 2, pp. 773–778, 2011.

[19] Y. Kassem and H. Çamur, "A laboratory study of the effects of wide range temperature on the properties of biodiesel produced from various waste vegetable oils," *Waste and biomass valorization*, vol. 8, no. 6, pp. 1995–2007, 2017.

[20] "Models for predicting the surface tension of biodiesel and methyl esters," *Renewable and Sustainable Energy Reviews*, vol. 41, pp. 202–216, 2015.

[21] S. V. D. Freitas, M. B. Oliveira, A. J. Queimada, M. J. Pratas, S. Lima, and J. A. P. Coutinho, "Measurement and prediction of biodiesel surface tensions," *Energy & Fuels*, vol. 25, no. 10, pp. 4811–4817, 2011.

[22] D. Frisch, H. Eyring, and J. F. Kincaid, "Pressure and temperature effects on the viscosity of liquids," *Journal of Applied Physics*, vol. 11, no. 1, pp. 75–80, 1940.

[23] M. Alamgir and J. Lienhard, "The temperature dependence of surface tension of pure fluids," 1978.

[24] M. Mourad and E. H. Noureldenn, "Benefits of exhaust gas energy for preheating biodiesel fuel to enhance engine emissions and performance," *Journal of Mechanical and Energy Engineering*, vol. 3, 2019.

[25] R. Fajgenbaum and R. G. dos Santos, "Influence of fuel temperature on atomization parameters in a pressure-swirl atomizer from a port fuel injector by shadowgraphy technique," *Journal of the Brazilian Society of Mechanical Sciences and Engineering*, vol. 38, no. 7, pp. 1877–1892, 2016.

[26] P. Aleiferis, J. Serras-Pereira, Z. Van Romunde, J. Caine, and M. Wirth, "Mechanisms of spray formation and combustion from a multi-hole injector with e85 and gasoline," *Combustion and Flame*, vol. 157, no. 4, pp. 735–756, 2010.

[27] C. D. Marriott, M. A. Wiles, J. M. Gwidt, and S. E. Parrish, "Development of a naturally aspirated spark ignition direct-injection flex-fuel engine," *SAE International Journal of Engines*, vol. 1, no. 1, pp. 267–295, 2009.

[28] P. L. Du Nouy, "A new apparatus for measuring surface tension," *The Journal of general physiology*, vol. 1, no. 5, pp. 521–524, 1919.

[29] L. Wilhelmy, "About the dependence of the capillarite "a ts constants of alcohol on the substance and shape of the wetted solid body," *annals of physics*, vol. 195, no. 6, pp. 177–217, 1863.

[30] C. E. Stauffer, "The measurement of surface tension by the pendant drop technique," *The journal of physical chemistry*, vol. 69, no. 6, pp. 1933–1938, 1965.

[31] S. Ebnesajjad and A. Landrock, "Chapter 2-surface tension and its measurement," *Adhesives Technology Handbook, 3rd ed.; Ebnesajjad, S., Landrock, AH, Eds*, pp. 19–34, 2015.

[32] J. Padday, "Theory of surface tension," *Surface and colloid science*, vol. 1, no. part I, 1969.

[33] W. D. Harkins and H. F. Jordan, "A method for the determination of surface and interfacial tension from the maximum pull on a ring," *Journal of the American Chemical Society*, vol. 52, no. 5, pp. 1751–1772, 1930.

[34] B. Freud and H. Freud, "A theory of the ring method for the determination of surface tension," *Journal of the American Chemical Society*, vol. 52, no. 5, pp. 1772–1782, 1930.

[35] F. Hansen and G. Rødsrud, "Surface tension by pendant drop: I. a fast standard instrument using computer image analysis," *Journal of colloid and interface science*, vol. 141, no. 1, pp. 1–9, 1991.

[36] H. Girault, D. Schiffrin, and B. Smith, "Drop image processing for surface and interfacial tension measurements," *Journal of Electroanalytical Chemistry and Interfacial Electrochemistry*, vol. 137, no. 2, pp. 207–217, 1982.

[37] M. Mohr, R. K. Wunderlich, K. Zweiacker, S. Prades-Rödel, R. Sauget, A. Blatter, R. Logé, A. Dommann, A. Neels, W. L. Johnson *et al.*, "Surface tension and viscosity of liquid pd 43 cu 27 ni 10 p 20 measured in a levitation device under microgravity," *npj Microgravity*, vol. 5, no. 1, pp. 1–8, 2019.

[38] J. Kremer, A. Kilzer, and M. Petermann, "Simultaneous measurement of surface tension and viscosity using freely decaying oscillations of acoustically levitated droplets," *Review of Scientific Instruments*, vol. 89, no. 1, p. 015109, 2018.

[39] A. Moradian and J. Mostaghimi, "Measurement of surface tension, viscosity, and density at high temperatures by free-fall drop oscillation," *Metallurgical and Materials Transactions B*, vol. 39, no. 2, pp. 280–290, 2008.

[40] B. Stückrad, W. Hiller, and T. Kowalewski, "Measurement of dynamic surface tension by the oscillating droplet method," *Experiments in Fluids*, vol. 15, no. 4, pp. 332–340, 1993.

[41] L. Yang, B. K. Kazmierski, S. D. Hoath, S. Jung, W.-K. Hsiao, Y. Wang, A. Berson, O. Harlen, N. Kapur, and C. D. Bain, "Determination of dynamic surface tension and viscosity of non-newtonian fluids from drop oscillations," *Physics of Fluids*, vol. 26, no. 11, p. 113103, 2014.

[42] S. N. Sahasrabudhe, V. Rodriguez-Martinez, M. O'Meara, and B. E. Farkas, "Density, viscosity, and surface tension of five vegetable oils at elevated temperatures: Measurement and modeling," *International Journal of Food Properties*, vol. 20, no. sup2, pp. 1965–1981, 2017.

[43] E. Ricci, D. Giuranno, and N. Sobczak, "Further development of testing procedures for high temperature surface tension measurements," *Journal of materials engineering and performance*, vol. 22, no. 11, pp. 3381–3388, 2013.

[44] Z. Chen, S. Xia, and P. Ma, "Measuring surface tension of liquids at high temperature and elevated pressure," *Journal of Chemical & Engineering Data*, vol. 53, no. 3, pp. 742–744, 2008.

[45] F. Mashayek, "Dynamics of evaporating drops. part ii: free oscillations," *International journal of heat and mass transfer*, vol. 44, no. 8, pp. 1527–1541, 2001.

[46] P. Miles, *Efficiency Merit Function for Spark-ignition Engines: Revision and Improvements Based on FY16-17 Research.* US Department of Energy, Office of Energy Efficiency & Renewable Energy, 2018.

[47] L. P. Wyszynski, C. R. Stone, and G. T. Kalghatgi, "The volumetric efficiency of direct and port injection gasoline engines with different fuels," SAE Technical Paper, Tech. Rep., 2002.

[48] G. T. Kalghatgi, "Fuel anti-knock quality-part i. engine studies," *SAE Transactions*, pp. 1993–2004, 2001.

[49] M. A. Ratcliff, J. L. Burton, P. Sindler, R. L. McCormick, E. D. Christensen, and L. A. Fouts, "Effects of heat of vaporization and octane sensitivity on knock-limited spark ignition engine performance," National Renewable Energy Lab.(NREL), Golden, CO (United States), Tech. Rep., 2018.

[50] D. A. Splitter and J. P. Szybist, "Experimental investigation of spark-ignited combustion with high-octane biofuels and egr. 2. fuel and egr effects on knock-limited load and speed," *Energy & Fuels*, vol. 28, no. 2, pp. 1432–1445, 2014.

[51] K. Kar, T. Last, C. Haywood, and R. Raine, "Measurement of vapor pressures and enthalpies of vaporization of gasoline and ethanol blends and their effects on mixture preparation in an si engine," *SAE International Journal of Fuels and Lubricants*, vol. 1, no. 1, pp. 132–144, 2009.

[52] G. M. Fioroni, E. D. Christensen, L. A. Fouts, and R. L. McCormick, "Heat of vaporization and species evolution suring gasoline evaporation measured by dsc/tga/ms for blends of c1 to c4 alcohols in commercial gasoline blendstocks," National Renewable Energy Lab.(NREL), Golden, CO (United States), Tech. Rep., 2019.

[53] G. Chupka, R. McCormick, E. Christensen, and L. Fouts, "Heat of vaporization by measurement using dsc/tga versus estimation using detailed hydrocarbon analysis," National Renewable Energy Lab.(NREL), Golden, CO (United States), Tech. Rep., 2015.

[54] J. G. Speight, *Natural water remediation: chemistry and technology*. Butterworth-Heinemann, 2019.

[55] G. Mendes, H. G. Aleme, and P. J. Barbeira, "Reid vapor pressure prediction of automotive gasoline using distillation curves and multivariate calibration," *Fuel*, vol. 187, pp. 167–172, 2017.

[56] V. Andersen, J. Anderson, T. Wallington, S. Mueller, and O. Nielsen, "Vapor pressures of alcohol- gasoline blends," *Energy & Fuels*, vol. 24, no. 6, pp. 3647–3654, 2010.

[57] K. Aikawa, T. Sakurai, and A. Hayashi, "Study of ethanol-blended fuel (e85) effects under cold-start conditions," *SAE International Journal of Fuels and Lubricants*, vol. 2, no. 1, pp. 196–203, 2009.

[58] L. Gibbs, B. Anderson, K. Barnes, G. Engeler, J. Freel, J. Horn, M. Ingham, D. Kohler, D. Lesnini, R. MacArthur *et al.*, "Motor gasolines technical review," *Chevron Products Company, San Ramon, CA*, pp. 53–54, 2009.

[59] H. J. Staat, A. van der Bos, M. van den Berg, H. Reinten, H. Wijshoff, M. Versluis, and D. Lohse, "Ultrafast imaging method to measure surface tension and viscosity of inkjet-printed droplets in flight," *Experiments in fluids*, vol. 58, no. 1, p. 2, 2017.

[60] L. Rayleigh, "On the capillary phenomena of jets," *Proceedings of the Royal Society of London*, vol. 29, pp. 71–97, 1879.

[61] H. Lamb, *Hydrodynamics*. Cambridge University Press, 1993.

[62] N. Ashgriz, *Handbook of atomization and sprays: theory and applications*. Springer Science & Business Media, 2011.

[63] C. L. Yaws, *Thermophysical properties of chemicals and hydrocarbons.* William Andrew, 2008.

[64] A. Pádua, J. Fareleira, J. Calado, and W. Wakeham, "Density and viscosity measurements of 2, 2, 4-trimethylpentane (isooctane) from 198 k to 348 k and up to 100 mpa," *Journal of Chemical & Engineering Data*, vol. 41, no. 6, pp. 1488–1494, 1996.

[65] "Surface tension measurement of fuels and alkanes at high pressure under different atmospheres," *Applied Surface Science*, vol. 229, no. 1, pp. 175–182, 2004.

[66] S. N. R. Isfahani, V. M. Sauer, and I. Schoegl, "Effects of dilution and pressure on combustion characteristics within externally heated micro-tubes," *Proceedings of the Combustion Institute*, vol. 38, no. 4, pp. 6695–6702, 2021.

[67] M. Inc, "Microfab technote 99-03 drive waveform effects on ink-jet device performance," Tech. Rep., 1999. [Online]. Available: http://www.microfab.com/images/pdfs/technote99-03.pdf

[68] P. Perona and J. Malik, "Scale-space and edge detection using anisotropic diffusion," *IEEE Transactions on pattern analysis and machine intelligence*, vol. 12, no. 7, pp. 629–639, 1990.

[69] A. Trujillo-Pino, K. Krissian, M. Alemán-Flores, and D. Santana-Cedrés, "Accurate subpixel edge location based on partial area effect," *Image and Vision Computing*, vol. 31, no. 1, pp. 72–90, 2013.

[70] R. Jain, R. Kasturi, and B. G. Schunck, *Machine vision.* McGraw-Hill New York, 1995, vol. 5.

[71] J. C. Andrae, "Development of a detailed kinetic model for gasoline surrogate fuels," *Fuel*, vol. 87, no. 10-11, pp. 2013–2022, 2008.

[72] E. Becker, W. Hiller, and T. Kowalewski, "Experimental and theoretical investigation of large-amplitude oscillations of liquid droplets," *Journal of Fluid Mechanics*, vol. 231, pp. 189–210, 1991.

[73] S. D. Hoath, W.-K. Hsiao, G. D. Martin, S. Jung, S. A. Butler, N. F. Morrison, O. G. Harlen, L. S. Yang, C. D. Bain, and I. M. Hutchings, "Oscillations of aqueous pedot: Pss fluid droplets and the properties of complex fluids in drop-on-demand inkjet printing," *Journal of Non-Newtonian Fluid Mechanics*, vol. 223, pp. 28–36, 2015.

[74] W. M. Haynes, *CRC handbook of chemistry and physics.* CRC press, 2014.

[75] A. K. Coker, *Ludwig's applied process design for chemical and petrochemical plants.* gulf professional publishing, 2014.

[76] M. G. Bravo-Sanchez, G. A. Iglesias-Silva, A. Estrada-Baltazar, and K. R. Hall, "Densities and viscosities of binary mixtures of 2-butanol+ isobutanol, 2-butanol+ tert-butanol, and isobutanol+ tert-butanol from (308.15 to 343.15) k," *Journal of Chemical & Engineering Data*, vol. 58, no. 9, pp. 2538–2544, 2013.

[77] A. Mejia, H. Segura, and M. Cartes, "Isobaric vapor–liquid equilibrium and isothermal interfacial tensions for the system ethanol+ 2, 5-dimethylfuran," *Journal of Chemical & Engineering Data*, vol. 58, no. 11, pp. 3226–3232, 2013.

[78] J. L. da Silva Jr and M. Aznar, "Thermophysical properties of 2, 5-dimethylfuran and liquid–liquid equilibria of ternary systems water+ 2, 5-dimethylfuran+ alcohols (1-butanol or 2-butanol or 1-hexanol)," *Fuel*, vol. 136, pp. 316–325, 2014.

[79] M. V. Rathnam, M. Kumar, R. T. Sayed, and D. Ambavadekar, "Study on thermophysical properties of binary mixtures of butyl propionate+ ketones at (303.15 and 313.15) kabstract densities, viscosities and speeds of sound for the binary systems of butyl propionate with cyclopentanone, 3-pentanone, cyclohexanone and," *European Chemical Bulletin*, vol. 3, no. 2, pp. 166–172, 2013.

[80] R. Balaji, M. Gowri Sankar, M. Chandra Sekhar, and M. Chandra Shekar, "Thermophysical and spectroscopic properties of binary liquid systems: acetophenone/cyclopentanone/cyclohexanone with n-methylformamide," *Physics and Chemistry of Liquids*, vol. 54, no. 4, pp. 422–439, 2016.

[81] B. R. Bzdek, R. M. Power, S. H. Simpson, J. P. Reid, and C. P. Royall, "Precise, contactless measurements of the surface tension of picolitre aerosol droplets," *Chem. Sci.*, vol. 7, pp. 274–285, 2016.

[82] R. J. Freund, W. J. Wilson, and D. L. Mohr, "Chapter 2 - probability and sampling distributions," in *Statistical Methods (Third Edition)*, third edition ed. Boston: Academic Press, 2010, pp. 67–124.

[83] A. Prosperetti, "Free oscillations of drops and bubbles: the initial-value problem," *Journal of Fluid Mechanics*, vol. 100, no. 2, pp. 333–347, 1980.

[84] R. Codes, "Chemical compatibility guide," *http://www.dstec.com.my/wp-content/uploads/2018/05/Chemical-Resistance-Chart-Detail.pdf*, 2016.

[85] W. Dang, W. Zhao, I. Schoegl, and S. Menon, "A small-volume, high-throughput approach for surface tension and viscosity measurements of liquid fuels," *Measurement Science and Technology*, vol. 31, no. 9, p. 095301, 2020.

[86] J. Anderson, D. DiCicco, J. Ginder, U. Kramer, T. Leone, H. Raney-Pablo, and T. Wallington, "High octane number ethanol–gasoline blends: Quantifying the potential benefits in the united states," *Fuel*, vol. 97, pp. 585–594, 2012.

[87] S. S. Popuri and R. M. Bata, "A performance study of iso-butanol-, methanol-, and ethanol-gasoline blends using a single cylinder engine," *SAE Transactions*, pp. 576–595, 1993.

[88] B. Rajesh Kumar and S. Saravanan, "Effect of iso-butanol addition to diesel fuel on performance and emissions of a di diesel engine with exhaust gas recirculation," *Proceedings of the Institution of Mechanical Engineers, Part A: Journal of Power and Energy*, vol. 230, no. 1, pp. 112–125, 2016.

[89] T. L. Alleman, A. Singh, E. D. Christensen, E. Simmons, and G. Johnston, "Octane Modeling of Isobutanol Blending into Gasoline," *Energy & Fuels*, vol. 34, no. 7, pp. 8424–8431, 2020.

[90] S. M. Sarathy, G. Kukkadapu, M. Mehl, W. Wang, T. Javed, S. Park, M. A. Oehlschlaeger, A. Farooq, W. J. Pitz, and C.-J. Sung, "Ignition of alkane-rich FACE gasoline fuels and their surrogate mixtures," *Proceedings of the Combustion Institute*, vol. 35, no. 1, pp. 249–257, 2015.

[91] H. Selim, S. Y. Mohamed, N. Hansen, and S. M. Sarathy, "Premixed flame chemistry of a gasoline primary reference fuel surrogate," *Combustion and Flame*, vol. 179, pp. 300–311, 2017.

[92] D. Vuilleumier, N. Atef, G. Kukkadapu, B. Wolk, H. Selim, D. Kozarac, S. Saxena, Z. Wang, C.-J. Sung, R. Dibble, and S. M. Sarathy, "The influence of intake pressure and ethanol addition to gasoline on single- and dual-stage autoignition in an hcci engine," *Energy & Fuels*, vol. 32, no. 9, pp. 9822–9837, 2018.

[93] B. Chen, Z. Wang, J.-Y. Wang, H. Wang, C. Togbé, P. E. Álvarez Alonso, M. Almalki, M. Mehl, W. J. Pitz, S. W. Wagnon, K. Zhang, G. Kukkadapu, P. Dagaut, and S. Mani Sarathy, "Exploring gasoline oxidation chemistry in jet stirred reactors," *Fuel*, vol. 236, pp. 1282–1292, 2019.

[94] S. Mirjalili, S. S. Jain, and M. Dodd, "Interface-capturing methods for two-phase flows: An overview and recent developments," *Center for Turbulence Research Annual Research Briefs*, vol. 2017, pp. 117–135, 2017.

[95] C. W. Hirt and B. D. Nichols, "Volume of fluid (VOF) method for the dynamics of free boundaries," *Journal of computational physics*, vol. 39, no. 1, pp. 201–225, 1981.

[96] R. I. Issa, "Solution of the implicitly discretised fluid flow equations by operator-splitting," *Journal of computational physics*, vol. 62, no. 1, pp. 40–65, 1986.

[97] D. L. Youngs, "Time-dependent multi-material flow with large fluid distortion," *Numerical methods for fluid dynamics*, 1982.

[98] J. Schlottke and B. Weigand, "Direct numerical simulation of evaporating droplets," *Journal of Computational Physics*, vol. 227, no. 10, pp. 5215–5237, 2008.

[99] S. Tanguy, T. Ménard, and A. Berlemont, "A level set method for vaporizing two-phase flows," *Journal of Computational Physics*, vol. 221, no. 2, pp. 837–853, 2007.

[100] M. Assael, E. Charitidou, C. N. de Castro, and W. Wakeham, "The thermal conductivity of n-hexane, n-heptane, and n-decane by the transient hot-wire method," *International journal of thermophysics*, vol. 8, no. 6, pp. 663–670, 1987.

[101] X. Wang, J. Wu, S. Qiu, and X. Li, "Measurements of the Thermal Conductivity of n-Octane, Isooctane, 1-Octene, and 1-Octanol in the Temperature Range from 253 to 393 K at Pressures up to 30 MPa," *Journal of Chemical & Engineering Data*, vol. 64, no. 10, pp. 4557–4564, 2019.

[102] R. C. Reid, J. M. Prausnitz, and B. E. Poling, *The properties of gases and liquids*. McGraw Hill Book Co., New York, NY, 1987.

[103] D. G. Goodwin, "Cantera: An open-source, object-oriented software suite for combustion," California institute of technology, Tech. Rep., 2002.

[104] D. R. Lide, *CRC handbook of chemistry and physics*. CRC press, 2004, vol. 85.

[105] C. Miller and L. Scriven, "The oscillations of a fluid droplet immersed in another fluid," *Journal of fluid mechanics*, vol. 32, no. 3, pp. 417–435, 1968.

[106] S. Chandrasekhar, "The oscillations of a viscous liquid globe," *Proceedings of the London Mathematical Society*, vol. 3, no. 1, pp. 141–149, 1959.

[107] A. Prosperetti, "Viscous effects on perturbed spherical flows," *Quarterly of Applied Mathematics*, vol. 34, no. 4, pp. 339–352, 1977.

[108] P. Suryanarayana and Y. Bayazitoglu, "Surface tension and viscosity from damped free oscillations of viscous droplets," *International journal of thermophysics*, vol. 12, no. 1, pp. 137–151, 1991.

[109] D. Plümacher, M. Oberlack, Y. Wang, and M. Smuda, "On a non-linear droplet oscillation theory via the unified method," *Physics of Fluids*, vol. 32, no. 6, p. 067104, 2020.

[110] B. Abramzon and W. Sirignano, "Droplet vaporization model for spray combustion calculations," *International journal of heat and mass transfer*, vol. 32, no. 9, pp. 1605–1618, 1989.

[111] S. Aggarwal and F. Peng, "A review of droplet dynamics and vaporization modeling for engineering calculations," 1995.

[112] S. S. Sazhin, "Advanced models of fuel droplet heating and evaporation," *Progress in energy and combustion science*, vol. 32, no. 2, pp. 162–214, 2006.

[113] A. K. Ray, E. J. Davis, and P. Ravindran, "Determination of ultra-low vapor pressures by submicron droplet evaporation," *The journal of chemical physics*, vol. 71, no. 2, pp. 582–587, 1979.

[114] A. Putnam, "Integratable form of droplet drag coefficient," *Ars Journal*, vol. 31, no. 10, pp. 1467–1468, 1961.

[115] F. Foucher, P. Higelin, C. Mounam-Rousselle, and P. Dagaut, "Influence of ozone on the combustion of n-heptane in a hcci engine," *Proceedings of the Combustion Institute*, vol. 34, no. 2, pp. 3005–3012, 2013.

[116] Y. Qian, X. Wang, L. Zhu, and X. Lu, "Experimental studies on combustion and emissions of rcci (reactivity controlled compression ignition) with gasoline/n-heptane and ethanol/n-heptane as fuels," *Energy*, vol. 88, pp. 584–594, 2015.

[117] J. J. Minty, M. E. Singer, S. A. Scholz, C.-H. Bae, J.-H. Ahn, C. E. Foster, J. C. Liao, and X. N. Lin, "Design and characterization of synthetic fungal-bacterial consortia for direct production of isobutanol from cellulosic biomass," *Proceedings of the National Academy of Sciences*, vol. 110, no. 36, pp. 14 592–14 597, 2013.

[118] M. Obergruber, V. Hönig, P. Procházka, V. Kučerová, M. Kotek, J. Bouček, and J. Mařík, "Physicochemical properties of biobutanol as an advanced biofuel," *Materials*, vol. 14, no. 4, 2021. [Online]. Available: https://www.mdpi.com/1996-1944/14/4/914

[119] W. Dang, M. Gurunadhan, I. Schoegl, and S. Menon, "Temperature effects on droplet oscillation decay with application to fuel property measurement," *Atomization and Sprays*, vol. 31, no. 10, pp. 1–23, 2021.

[120] L. Tao, J. N. Markham, Z. Haq, and M. J. Biddy, "Techno-economic analysis for upgrading the biomass-derived ethanol-to-jet blendstocks," *Green Chemistry*, vol. 19, no. 4, pp. 1082–1101, 2017.

[121] S. M. Sarathy, G. Kukkadapu, M. Mehl, W. Wang, T. Javed, S. Park, M. A. Oehlschlaeger, A. Farooq, W. J. Pitz, and C.-J. Sung, "Ignition of alkane-rich face gasoline fuels and their surrogate mixtures," *Proceedings of the Combustion Institute*, vol. 35, no. 1, pp. 249–257, 2015.

[122] J. Gliński, "Determination of the conditional association constants from the sound velocity data in binary liquid mixtures," *The Journal of chemical physics*, vol. 118, no. 5, pp. 2301–2307, 2003.

[123] M. Roegiers and B. Zhmud, "Property blending relationships for binary mixtures of mineral oil and elektrionised vegetable oil: viscosity, solvent power, and seal compatibility index," *Lubrication Science*, vol. 23, no. 6, pp. 263–278, 2011.

[124] G. M. Chupka, E. Christensen, L. Fouts, T. L. Alleman, M. A. Ratcliff, and R. L. McCormick, "Heat of vaporization measurements for ethanol blends up to 50 volume percent in several hydrocarbon blendstocks and implications for knock in si engines," *SAE International Journal of Fuels and Lubricants*, vol. 8, no. 2, pp. 251–263, 2015.

VITA

Wanjun Dang was born in Wuhan, China. After completing her high school at Wuhan No. 14 High School, she finished her Bachelor of Engineering in Mechanical design, manufacturing, and automation from Wuhan University of Technology Huaxia College in 2008. She started her graduate school in 2009 and completed her Master's degree in Mechanical Engineering from Wuhan University of Technology in Dec 2011. Then, she moved to Nanjing, China, and work at Ford Motor Research & Engineering (Nanjing) Co., Ltd as an engineer in the Department of Product Development Body Interior. After that, she came to the US for the first time to pursue her PhD study in 2015 at Stevens Institute of Technology. Then, she applied for PhD opportunity again in 2017 and restarted her PhD in the US at Louisiana State University, Baton Rouge, LA in the Department of Mechanical and Industrial Engineering in Aug 2017. Her major work was experiment-based and focused on droplet-based approaches for fuel physical property measurements using droplet oscillation and evaporation theories. She passed her PhD final defense on Oct 5, 2021.